pennsylvania
DEPARTMENT OF TRANSPORTATION

Determination of Structural Benefits of PennDOT-Approved Geogrids in Pavement Design

FINAL REPORT

December 31, 2010

By Angelica M. Palomino, Xiaochao Tang and Shelley M. Stoffels

The Thomas D. Larson
Pennsylvania Transportation Institute

COMMONWEALTH OF PENNSYLVANIA
DEPARTMENT OF TRANSPORTATION

PENNSTATE
1855

CONTRACT No. 510602
PROJECT No. PSU 018

DEPARTMENT OF TRANSPORTATION
UNITED STATES OF AMERICA

This work was sponsored by the Pennsylvania Department of Transportation, the Mid-Atlantic Universities Transportation Center, and the U.S. Department of Transportation, Federal Highway Administration. The contents of this report reflect the views of the authors, who are responsible for the facts and the accuracy of the data presented herein. The contents do not necessarily reflect the official views or policies of the Federal Highway Administration, U.S. Department of Transportation, the Mid-Atlantic Universities Transportation Center, or the Commonwealth of Pennsylvania at the time of publication. This report does not constitute a standard, specification, or regulation.

Technical Report Documentation Page

1. Report No.	2. Government Accession No.	3. Recipient's Catalog No.
FHWA-PA-2010-012-PSU 018		

4. Title and Subtitle	5. Report Date
Determination of Structural Benefits of PennDOT Approved Geogrids in Pavement Design	December 31, 2010
	6. Performing Organization Code

7. Author(s)	8. Performing Organization Report No.
Angelica M. Palomino, Xiaochao Tang, and Shelley M. Stoffels	LTI 2011-06

9. Performing Organization Name and Address	10. Work Unit No. (TRAIS)
The Thomas D. Larson Pennsylvania Transportation Institute The Pennsylvania State University 201 Transportation Research Building University Park, PA 16802-4710	11. Contract or Grant No. 510602, PSU 018

12. Sponsoring Agency Name and Address	13. Type of Report and Period Covered
The Pennsylvania Department of Transportation Bureau of Planning and Research Commonwealth Keystone Building 400 North Street, 6th Floor Harrisburg, PA 17120-0064	Final Report 4/01/08 – 12/31/10
	14. Sponsoring Agency Code

15. Supplementary Notes

COTR: Rodney Klopp, 717-787-7287, rklopp@state.pa.us

16. Abstract

This research was undertaken to evaluate and determine structural benefits of three Pennsylvania Department of Transportation approved geogrids for reinforcing weak pavement subgrade. A mechanistic-empirical approach was adopted to develop subgrade permanent deformation models for geogrid-reinforced flexible pavements. Multi-scale tests were conducted for the three geogrids. Mechanical and index properties of the geogrids were tested before the geogrids were subjected to bench-scale testing, namely pullout and direct shear tests. Two sets of accelerated pavement tests were carried out to investigate the effectiveness of geogrids in improving pavement performance. For each APT, four pavement sections were constructed in a pit with concrete walls, among which one was control and the others were reinforced with different geogrids. Two different types of soil were involved for the subgrade construction through the two sets of accelerated testing. Various instruments were installed in the pavement system to measure both static and dynamic response of the pavements. Finite element models were created to simulate the pavement sections in the pit. Subgrade permanent deformation models were developed for pavement sections on the basis of the model adopted by the *Mechanistic-Empirical Pavement Design Guide.* The MEPDG model was modified to accommodate the test conditions in this study. Calibration of the model was conducted using the measurements from the Instrumented APT I while the measurements from the Instrumented APT II were used to verify the model.

17. Key Words	18. Distribution Statement
Geogrid, flexible pavement, subgrade, permanent deformation model, accelerated pavement testing, finite element model, MEPDG	No restrictions. This document is available from the National Technical Information Service, Springfield, VA 22161

19. Security Classif. (of this report)	20. Security Classif. (of this page)	21. No. of Pages	22. Price
Unclassified	Unclassified	164	

TABLE OF CONTENTS

LIST OF TABLES

LIST OF FIGURES

EXECUTIVE SUMMARY

This final report presents results and findings from the research work undertaken to evaluate and determine structural benefits of three Pennsylvania Department of Transportation (PennDOT)-approved geogrids for reinforcing weak pavement subgrade. A mechanistic-empirical (ME) approach was adopted in this study to develop subgrade permanent deformation models for geogrid-reinforced flexible pavements.

Multi-scale tests were conducted for the three geogrids. Mechanical and index properties of the geogrids were tested before the geogrids were subjected to bench-scale testing, namely pullout and direct shear tests. The bench-scale tests were mainly to evaluate the interface properties of the geogrids surrounded by pavement materials that were used in the subsequent accelerated testing.

Two sets of accelerated pavement tests (APT) were carried out to investigate the effectiveness of geogrids in improving pavement performance. For each APT, four pavement sections were constructed in a pit with concrete walls, among which one was control and the others were reinforced with different geogrids. Two different types of soil were involved for the subgrade construction through the two sets of accelerated testing.

Various instruments were installed in the pavement system to measure both static and dynamic response of the pavements. Deformation at the top of subgrade was measured using a linear variable differential transformer (LVDT) in each section while the vertical stress at the top of the subgrade was monitored through earth press cells. Strains in the geogrids were measured using foil strain gages attached on the ribs. A one-third scale model mobile load simulator (MMLS3) was used to apply unidirectional traffic load on the pavement sections. Surface rutting was measured using a profilometer at intervals of the MMLS3 axle repetitions. Lightweight deflectometer (LWD) tests were conducted on the pavement sections to backcalculate the pavement layer properties before the accelerated testing.

Finite element (FE) models were created to simulate the pavement sections in the pit. The FE models were calibrated using the measurements from the LWD tests. The calibration was accomplished through an inverse analysis procedure coupling the FE models with an optimization subroutine. Interface properties obtained from the bench-scale tests were

incorporated into the FE models. The FE models provided pavement responses that were needed for the permanent deformation models.

Subgrade permanent deformation models were developed for pavement sections on the basis of the model adopted by the *Mechanistic-Empirical Pavement Design Guide* (MEPDG). The MEPDG model was modified to accommodate the test conditions in this study. Calibration of the model was conducted using the measurements from the Instrumented APT I while the measurements from the Instrumented APT II were used to verify the model.

1 INTRODUCTION

1.1 Problem Statement

Weak subgrades have been and still are of major concern to pavement design engineers due to their potential contribution to rutting in flexible pavements. Typical approaches adopted to avoid or minimize the problem have focused on: (1) increasing the thicknesses of the pavement layers, both unbound and asphalt concrete; (2) removing a top layer of the subgrade and backfilling it with a soil of higher bearing capacity and better properties to resist frost/heave and other load and environmental factors; and (3) stabilizing the subgrade through a variety of techniques such as adding lime or cement, or incorporating reinforcement media such as geosynthetics. Several factors are considered in selecting an appropriate technique from the aforementioned list, including but not limited to: feasibility, associated cost, time for construction, effort required, and effectiveness. Recently, there has been a growing interest in the use of geosynthetics, particularly geogrids, for subgrade reinforcement, where geogrids are placed at the interface between the subgrade and the aggregate base layer. Factors favoring the use of geogrids include simple and quick installation; increase in types, brands, and quality of geogrids; and the decrease in cost of purchasing the material due to high competitiveness among manufacturers. However, incorporating their benefit in pavement design has not been adequately researched and implemented. Limited design methodologies for reinforced subgrade pavement design have been proposed, most of which are empirical in nature and often presented by the manufacturers in the form of a black-box design without any mechanistic reasoning. Therefore, determining the structural benefits of reinforced subgrade is imperative for any meaningful design that incorporates mechanistic procedures and fundamental material properties.

1.2 Research Objectives

The objective of this project was to determine the structural benefits of PennDOT-approved geogrids when incorporated as subgrade reinforcement in flexible pavements. The objective was met by characterizing the geogrids through multi-scaled testing (i.e., index testing, bench-scale testing, and accelerated pavement testing) and by customizing mechanistic-empirical permanent deformation models for geogrid-reinforced flexible pavements.

1.3 Research Scope

This research was focused on the application of geogrids in flexible pavements. More specifically, this research concentrated on the scenario where geogrids as a reinforcing element are placed at the interface between a weak soil subgrade and an aggregate base course. Four different geogrid products representing a wide range of geogrid categories were involved in this study. Three different types of soil considered as problematic for pavement subgrade were used while the construction of aggregate base course and asphalt layer keep using the same type of material through all the sets of testing.

This study included multi-scaled testing of geogrid properties and reinforcing performance. Index testing was conducted on selected geogrids to obtain consistent physical and mechanical properties. Bench-scale testing, including direct shear and pullout tests, were used to characterized the geogrids within surrounding pavement materials. Using the one-third scale model mobile load simulator (MMLS3), accelerated pavement testing was performed on pavement slabs with scaled structural thicknesses reinforced by different geogrids. Overburden stress, subgrade deformation, and geogrid strains were monitored during accelerated testing. The test results were compared and analyzed to identify critical geogrid characteristics that contribute most to the reinforcing performance in pavements.

In-situ resilient moduli of pavement slabs reinforced by different geogrids were obtained through an inverse analysis procedure based on lightweight deflectometer (LWD) tests. Tested geogrid and pavement material properties were implemented into finite element (FE) models to investigate the contribution of geogrid reinforcement to the pavement system. The FE model was verified by the experimental measurements. Critical responses of pavements were extracted from the FE model. A mechanistic-empirical (ME) permanent deformation model was then developed on the basis of critical responses from the FE model and measurements from the accelerated tests. The ME model takes into account the geogrid reinforcing effects in addition to the pavement materials properties.

2 LITERATURE REVIEW

2.1 Geosynthetics

Due to their favorable characteristics such as non-corrosiveness, long-term durability, lightness, and simplicity of installation, geosynthetics are now a unique type of widely used civil engineering materials, and have become as popular as other construction materials such as concrete, steel, and timber etc. The prefix "geo" implies that the primary applications of geosynthetics are associated with geotechnical engineering-related materials such as soil, rock, and earth, while the suffix "synthetics" refers to the fact that the materials are made from synthetic products.

There are many types of geosynthtic products with various structures, different polymeric materials, and design functions. Table 1 summarizes the common geosynthetic products. This study focuses on the use of geogrids in flexible pavement.

Table 1 Common geosynthetic products (Koerner, 1998; Shukla and Yin, 2006)

Geosynthetics	**Polymeric Materials**	**Structures**	**Application Areas**	**Major Functions**
Geotextiles	polypropylene (PP), polyster(PET), polyethylene (PE), polyamid (PA)	flexible, permeable fabrics	retaining walls, slopes, embankments, pavements, landfills, dams	separation, reinforcement, filtration, drainage, containment
Geogrids	PP, PET, high-density polyethylene (HDPE)	mesh-like planar product formed by intersecting elements	pavements, railway ballasts, retaining walls, slopes, embankments, bridge abutments	reinforcement, separation
Geonets	medium-density polyethylene (MDPE), HDPE	net-like planar product with small apertures	dams, pipeline and drainage facilities	drainage
Geomembranes	PE, polyvinyl chloride (PVC), chlorinated polyethylene (CPE)	impervious thin sheets	containment ponds, reservoirs, and canals	fluid barrier/liner
Geocomposites	depending on geosynthetics included	combination of geotextiles and geogrids/geonets, geomembranes and geogrids	embankments, pavements, slopes, landfills, dams	separation, reinforcement, filtration, drainage

2.2 Geogrids and Their Functions in Flexible Pavements

A geogrid is a net-like geosynthetic with apertures of sufficient size to allow interlocking with surrounding unbound materials such as soil, rock, and aggregate, and functions primarily as reinforcement. Existing, commercially available geogrid products include extruded geogrids, woven geogrids, and welded geogrids. Extruded geogrids are formed using a polymer sheet that is punched and drawn in either one or two directions. Woven geogrids are manufactured by weaving polymer fibers, typically polypropylene (PP) or polyester (PET) that can be coated for increased abrasion resistance (Berg et al., 2000). Welded geogrids are manufactured by welding the junctions of woven segments of extruded polymers. Geogrids can also be divided into two categories based on their stiffness: stiff geogrids, usually made from polypropylene (PP) or polyethylene (PE), have a flexural rigidity greater than 1,000 g-cm (ASTM D 1388), while flexible geogrids, made by a textile weaving process and generally from PET, have a flexural rigidity less than 1,000 g-cm (Koerner, 1998).

During the manufacturing processes, the direction coincident with the direction in which the geogrid is manufactured on the mechanical loom is called machine direction (MD) or roll length direction, while the direction perpendicular to the machine direction in the plane of geogrids is the cross machine direction / transverse direction (TD). Some mechanical properties of geogrids are different when tested in machine direction or cross machine direction. The machine direction is parallel with the traffic direction when installing geogrids in pavements. Figure 1 shows a geogrid sample with terminologies regarding the geogrid structure.

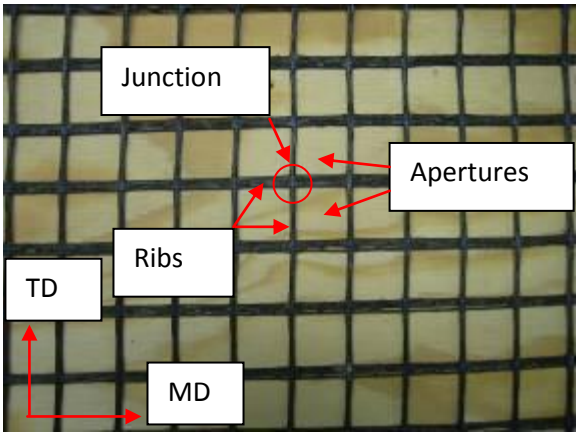

Figure 1. A geogrid sample

When geogrids are used for reinforcing pavements, they can be placed underneath or within the hot-mix asphalt (HMA) layer or within the aggregate layer, or at the subgrade-aggregate interface layer. Geotextiles, geogrids, or combinations of both have been used in the aforementioned applications. This study focuses on using geogrids at the interface between subgrade and aggregate layers to stabilize weak pavement subgrades.

Overlay stress absorption and reinforcement is accomplished by binding the geogrid to the surface of an existing damaged roadway and then covering the geogrid with a new asphalt concrete overlay. This technique delays the appearance of reflective cracks, lengthens the useful life of the overlay (Halim and Razaqpur, 1993; Gilchrist et al., 1996). Also, the inclusion of geogrids within an asphalt layer may lead to an improved performance in terms of rutting resistance (Brown et al., 1984; Haas, 1984).

As a pure reinforcement element for base course, the geogrid is placed within the aggregates base course at different heights, depending on the thickness of base course. Webster (1993) recommended that the geogrid be placed at the bottom of the base for an aggregate layer less than 35.6 cm (14 in) or in the middle of the base layer in excess of 35.6 cm.

For the purpose of stabilizing weak pavement subgrades, geogrids are placed at the interface between a prepared subgrade and aggregate base course (ABC), as Figure 2 shows. The stabilization of weak subgrade results from reinforcing the base course through particle-geogrid interlocking effects and preventing penetration of aggregates into subgrade soils. A ratio of the minimum aperture dimension over average particle size (D_{50}) greater than three is recommended for achieving the best interlocking interaction (Jewell et al., 1984).

Geogrids also provide restraint to the aggregates and minimize lateral spreading of the base course aggregates when subjected to vehicular loads. Lateral spreading of base course aggregate leads to increased vertical strains, and thus a permanent deformation in the wheel path. The modulus of the base is expected to increase along with the developed shear interaction between the aggregates and geogrids, since the granular base course is stress-dependent. The increase in base layer modulus results in an improved vertical stress distribution (more widely distributed) above subgrade, as shown in Figure 2-b, subsequently reducing subgrade deformation (Perkins, 1999).

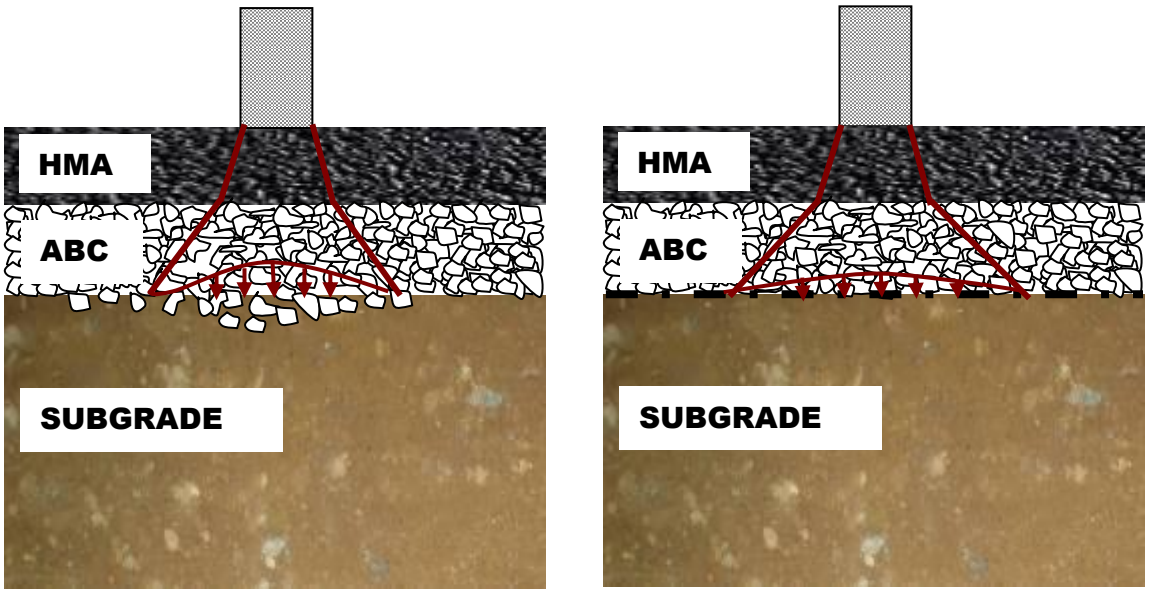

(a) (b)

Figure 2. Geogrid functions in a pavement: (a) without geogrids; (b) with geogrids

A geogrid, by virtue of its design, is unable to provide complete separation of base course and subgrade material. Placement of the geogrid between the base course and subgrade may restrict some coarse aggregate penetration into the subgrade. Contamination of aggregate base course into the subgrade layer in geogrid-stabilized road sections has been documented in field tests (Austin and Coleman, 1993) and large-scale laboratory pavement loading tests (Barksdale, et al., 1989; Al-Qadi et al., 1994).

2.3 Review of Laboratory and Field Studies of Geogrid-Reinforced Flexible Pavements

Through both laboratory and field studies, it has been shown that the inclusion of geogrids at the interface between the base course and subgrade in flexible pavements can improve the performance of flexible pavements by extending the service life or reducing pavement structural thickness with equivalent performance. This section provides a review of existing laboratory and field studies of geogrid-reinforced flexible pavements.

2.3.1 Laboratory Studies

Numerous laboratory investigations have been conducted to study the effectiveness of geogrid additions to the flexible pavement system. Among the laboratory experiments that have been conducted, geogrids were placed at the interface between the aggregates base course and soil subgrade or within the base course at various locations.

Carroll et al. (1987)

Through a number of laboratory tests using circular plates, Abd El Halim (1983) studied the reinforcing performance of geogrids placed at the sugrade-aggregate interface under dry (strong) and saturated (weak) subgrade conditions. It was found that geogrid-reinforced sections withstood more loading cycles before the failure (20-mm rutting depth). The pretension effects for geogrids were also investigated and found not beneficial to the system compared to normal geogrid installation. Based on the work of Abd El Halim (1983), Carroll et al. (1987) developed a design chart that provides a conversion of a conventional unreinforced base course thickness to a geogrid-reinforced section as shown in Figure 3. The inflection point in Figure 3 represents the minimum thickness requirement. It is important to point out that this design chart was derived from experimental results for a single stiff geogrid.

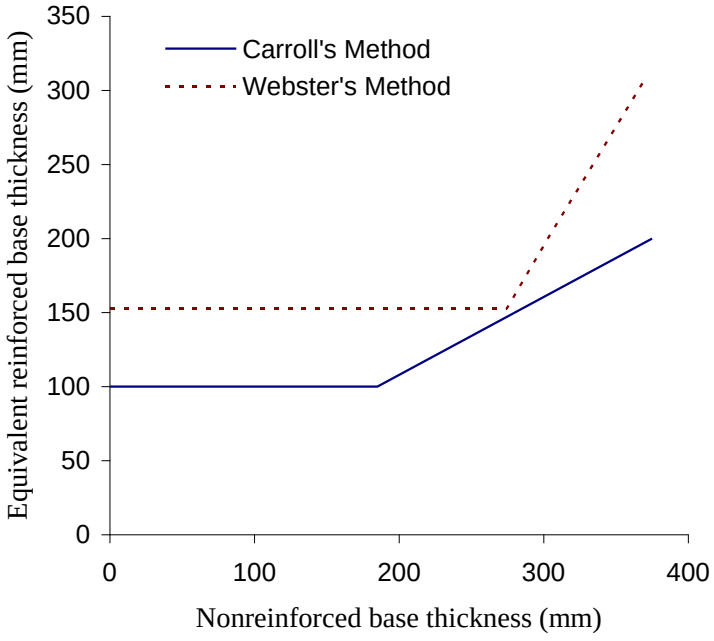

Figure 3. Design criteria for base course thickness proposed by Caroll et al. (1987) and Webster (1993)

Haas et al. (1988)

Aimed to understand the geogrid reinforcement mechanisms, a comprehensive test program was carried out in a 4.5-m × 1.8-m × 0.9-m box. Cyclic loads were applied through a steel plate with diameter of 30.5 cm. The variables of the testing program included the base thickness, subgrade strength, and locations of geogrid reinforcement. The surface deflection, vertical stress atop subgrade, and strains in geogrids were measured at intervals of load repetitions. It was found that the geogrid reinforcement increased the number of load applications by a factor of 3. The base thickness reductions were 25 to 50 percent by inclusion of geogrids. It was suggested that the geogrid should be placed at the interface between the base course and subgrade for thin base sections and near the midpoint of the thicker bases.

Al-Qadi et al. (1994)

Pavement sections were constructed in a 3-m × 2.1-m × 1.8-m box to simulate a typical secondary road in Virginia built on a weak subgrade. Different base course thickness, subgrade California Bearing Ratio (CBR) values and geotextiles and geogrids were involved. Cyclic loads were applied using a steel plate of 300-mm diameter. Surface deflections were measured by an array of LVDTs. It was found that the geotextiles and geogrids offer considerable improvement to the performance of pavement sections built over a low-CBR subgrade. The reinforcing mechanisms of geotextiles and geogrids were found different. Geotextiles provided separation between the aggregates and soil, while this was not the case for geogrids.

Montanelli et al. (1997)

Intended to quantify the structural contribution of geogrids to pavement systems, laboratory tests using a circular loading plate were conducted on pavements built over subgrade with CBR ranging from 1% to 18%. In order to make use of the AASHTO design procedure, Montanelli et al. developed a layer coefficient ratio for the granular base, which is equal to the ratio of the reinforced to unreinforced based layer coefficients. Depending on the subgrade CBR values, the ratio ranged from 1.5 to 2 according to the experimental data. The value of the ratio can be used as a multiplication factor for calculating an important parameter, the structural number (SN) for the AASHTO design procedure:

$$SN = a_1 D_1 + a_2 D_2 G .$$

Where a_1 and a_2 are layer coefficients used to characterize the structural capacity of different layers in the conventional pavement system, D_1 and D_2 are their corresponding thicknesses, and G is the ratio of layer coefficient.

The reinforced base thickness can be determined as follows:

$$D_2 = \frac{SN - a_1 D_1}{D_2 G}$$

As a result, a reduction in base thickness can be achieved depending on the G value.

Perkins (1999)

A reinforced concrete box with the dimensions of 2 m × 2 m × 1.5 m was used for the testing. 40-kN cyclic loads were applied through a 305-mm diameter steel plate. A total of 20 test sections were constructed, including variables of two geogrid products and one woven geotextile, subgrade type and strength, base course thickness, and position of geosynthetics. Pavement surface deformation, strains in geosynthetics, strain and stress in soil, temperature and moisture content were measured using various instruments. Geogrids showed substantial improvement for pavements built over a subgrade with CBR of 1.5, while little improvement was found for pavements built over a stronger subgrade with CBR of 20. Between the two geogrid products used in the test, the stiffer one exhibited better performance. Both geogrids performed better than the geotextile. The position of geogrid placement was considered an important factor affecting the geogrid performance. Significantly better performance was found with the geogrid placed closer to the load in the base, while geogrids showed much less improvements when placed at the bottom of a thicker base.

Leng et al. (2002)

A series of laboratory tests were conducted in a 1.5-m × 1.5-m × 1.35-m box to study the characteristics of geogrid-reinforced aggregates placed over weak soil subgrade. Repetitive loads were applied through a 305-mm circular plate with contact pressure of 500 kPa. The surface deformation and vertical pressure distribution at the interface between aggregate base and soil

subgrade were monitored during tests. The results of the testing suggested that the geogrid reinforcement decreased the surface deformation, improved the stress distribution, and mitigated the degradation of the aggregate base.

2.3.2 Field Investigation

While laboratory-scale tests provide quantitive information on the benefits of geogrid reinforcements, investigations on full-scale geogrid-reinforced flexible pavements yield results more relevant to actual pavement performance. This section presents a review of studies conducted for full-scale geogrid-reinforced flexible pavements.

Webster (1993)

The study was conducted on four lanes of flexible pavement with each lane divided into four separate sections. The aggregate base courses were constructed with four different thicknesses: 152, 254, 305, and 457 mm. A multi-depth deflectometer (MDD) was used to measure deflections and deformations at various depths. Field tests on flexible pavements with subgrade CBR values of 3% and 8% showed the benefits of geogrid reinforcements in terms of rutting resistance. A design chart as shown in Figure 3 was generated by comparing the performance for sections reinforced by geogrids and sections of equivalent base course thickness. Inspection of Figure 3 shows that the design curves developed from the two research programs are significantly different, due to the nature of purely empirical derivation of the two studies.

Perkins (2002)

A total of four full-scale test sections were constructed and subjected to traffic load applied by a Heavy Vehicle Simulator (HVS). Each of the four sections was 9.91 m long and 3.18 m wide. The unidirectional 40-kN wheel load was applied at the center of each section. All four sections consisted of four distinguished layers: 75-mm asphalt concrete, 300-mm aggregate base, 1.37-m A-7-6 soil, and 1.35-m A-2-4 soil. Three geosynthetics (two geogrids and one geotextile) were placed atop the subgrade of three of the four sections. Pavement surface profiles were measured at the intervals of traffic. Vertical stresses in the subgrade soil were measured for

each section and 3-dimentional stresses were measured at one point in the base course. Strain coils were used to measure strains at various depths of the pavement sections.

It was found that all three geosynthetics showed significant improvement in performance in terms of rutting resistance. Considerable differences in stress and strain measurements between reinforced and unreinforced sections were observed. Differences among the reinforced sections were apparent but not significant. Based on the measurements of stresses and strains, it was suggested that the dominant reinforcing mechanisms included a reduction of horizontal strain in the bottom of the base and wider distribution of vertical stress atop the subgrade.

Aran (2006)

Long-term performance of geogrid reinforcement in flexible pavement was investigated in this study. In 1986 and 1990, two sections were constructed to evaluate the geogrid reinforcing performance. In the section constructed in 1986, the geogrid was placed at the bottom of a 25.4-cm base course. An extra 5-cm HMA layer was placed in the control section. For the site constructed in 1990, the geogrid was placed at the bottom or middle of a 10-cm base layer. The control section consisted of 15-cm lime-stabilized subgrade. Performance evaluation was conducted in the years 1991, 2004, and 2005.

Short-term evaluation showed that no significant difference was identified among the test sections. Long-term evaluation indicated that the geogrid performed comparably with the 5-cm HMA layer. The inclusion of geogrids can be considered equivalent to a 15-cm lime-stabilized subgrade. The reinforcing effectiveness of geogrids was more profound when installed in thinner sections.

Al-Qadi et al. (2008)

A total of nine full-scale pavement sections were constructed over a weak subgrade with CBR of 4 to study the effectiveness of geogrids on low-volume flexible pavements. Two geogrids, three base thicknesses, and two HMA thicknesses were involved among the test sections. A total of 173 instruments were installed to measure stress, strain, deflection, moisture, pore-water pressure, and temperature. A unidirectional 44-kN dual-tire load was applied to simulate field loading conditions.

It was found that geogrids are effective in reducing pavement distresses. Based on instrument measurements and visual observation after trenching, a reinforcing mechanism was suggested that the geogrid is effective in reducing horizontal shear deformation of the aggregate layer, particularly in the traffic direction. For a flexible pavement with thin aggregate base, the optimum position of geogrid placement is at the interface between the base course and subgrade. For a thicker base, the optimal location of geogrid is at the upper third of the layer.

Henry et al. (2009)

The purpose of this study was to determine whether geosynthetic reinforcement is beneficial at conditions typically encountered in state highway construction, especially a thicker base layer and HMA layer compared to most previous research. Two HMA layer and base course thicknesses were involved: 102 mm and 152 mm for the HMA layer, 300 mm and 600 mm for the base layer. A total of eight full-scale pavement sections were constructed with the combination of the HMA and base thicknesses including reinforced and unreinforced sections. Falling weight deflectometer (FWD) tests showed the subgrade modulus value varied from 109 MPa to 138 MPa and water was added to the subgrade to reduce the stiffness to the target of 35 MPa. Moisture content sensors were used to monitor the moisture content of soil throughout the project. Custom-manufactured electromagnetic induction coils were used to measure both vertical and horizontal deformations. Both permanent and elastic strains in asphalt and soil were measured. For each section, seven pressure cells were installed in three perpendicular directions. Geogrids were instrumented with foil strain gages to measure longitudinal and transverse strains on the top and bottom of the grids. An HVS was used to apply unidirectional traffic load with tire pressure of 689.5 kPa.

Based on the testing results, it was concluded that the geogrid-reinforced sections generally were able to sustain more traffic load before the pavement failed. One exception was that the geogrid reinforcement did not show benefits for sections with thicker base course (600 mm) and thicker HMA layer (150 mm). It was found that the inclusion of geogrids did not decrease vertical elastic strains of any layers. The permanent strains in geogrids developed with the surface rut depth.

Cox et al. (2010)

This study was aimed to characterize the deformation behavior of geosynthetic-reinforced flexible pavements under dynamic loading. Cyclic plate load (CPL) tests using a Vibroseis (shaker) were conducted on geosynthetic-reinforced pavements test sections constructed for a previous study. An array of LVDTs was used to measure the permanent and elastic surface deflection as a function of load repetitions. The results from the tests on the full-scale pavements showed improved pavement performance with increasing base course thickness. However, no clear difference was found in pavement performance between reinforced and unreinforced sections, possibly because there were not enough strains developed in the pavement to mobilize the geogrid.

2.4 Review of Accelerated Pavement Testing

Accelerated pavement testing (APT) is defined as the simulation of effects of long-term loading conditions on pavement structures by applying wheel loading in a controlled manner and in a compressed time period (Hugo and Martin, 2004). APT is primarily used for the following purposes, among others:

- Pavement performance measurement and prediction
- Evaluation and improvement of pavement structural design
- Vehicle-pavement-environment interaction
- Development and evaluation of rehabilitation and maintenance techniques and strategies
- Evaluation of the usage of existing, new, and modified materials in pavements

Compared to long-term field evaluations, the advantages of APT testing are the ability to conduct performance tests at relatively low costs over a short time period, and the ability to control the loading and environmental conditions (Metcalf, 1996).

According to Hugo and Martin (2004), 28 APT facilities were reportedly operational and active worldwide in the year 2004. Among the existing APT facilities, the loading device varied from live traffic, actual vehicles to load simulators, while the pavement structures being tested ranged from full-scale roads to pavements with reduced structural capacity. The testing conditions could be ambient environments (indoor or outdoor) or controlled environments (modified temperatures and moistures). Although the nature of APT varies, APT facilities can be

divided into two primary categories in terms of the magnitude of wheel load: full-scale APT and small-scale APT. Full-scale APT applies traffic load at or above the appropriate legal load limit (Metcalf, 1996) while the small-scale APT's wheel load is typically below the load limit.

2.4.1 Full-Scale Accelerated Pavement Testing

According to loading conditions, there are two types of full-scale APT facilities: test road/track and full-scale mobile load devices. Test roads or test tracks are typically subjected to loading from actual traffic or actual vehicles. Representative test roads/tracks are MnROAD, WesTrack, NCAT Test Track, Virginia Smart Road, and Ohio SHRP Test Road, among others. The test roads/tracks provide more realistic testing conditions, while the cost of test roads/tracks is typically high. The other major category of APT uses mobile load devices such as Heavy Vehicle Simulator, Texas Mobile Load Simulator (TxMLS), FHWA Accelerated Loading Facility (ALF), Advanced Transportation Loading System (ATLaS), and Danish Road Testing Machine (RTM). A mobile load device tests a small sample area of either in-service pavement sections or laboratory pavement sections. Described below are representations of the two categories of full-scale APT facilities.

MnROAD

Aimed to investigate road designs and procedures, materials used, and the effects of traffic loads and weather on the pavement, the Minnesota Department of Transportation (MnDOT) started the Minnesota Road Research Project (MnROAD) in 1989. The roadway test facility consists of two test roads: a 5.6-km-long interstate roadway constructed next to I-94 and loaded by deviated freeway traffic; and a 4-km-long low-volume loop subjected to controlled load conditions (Newcomb, 1990).

More than 4,500 various electronic sensors were embedded in MnROAD to measure the load responses of the pavement and to monitor the environmental factors, which provided a unique opportunity to gain insight into the performance and durability of various sensors in pavements (Baker et al., 1994). The sensors were categorized into load response sensors and environmental sensors. According to the needs of measurements, different kinds of load response sensors were installed: strain gauges, LVDT, clip gauge, piezo-accelerometer, soil pressure cell, tiltmeter, etc. Various environment sensors such as pore water pressure cell, resistivity probe, thermocouple, and time domain reflectometer (TDR) were installed on the site to continuously

monitor the environmental effects (Baker et al., 1994). Probably the most prominent accelerated pavement test program after the AASHO Road Test in the late 1950s, MnROAD has been involved in numerous aspects of pavement research and practice: pavement design calibration and verification, low-volume road design, thin and ultra-thin whitetopping, continuous compaction control (intelligent compaction), new techniques in pavement assessments (dynamic cone penetrometer and ground penetrating radar), etc. (Tompkins et al., 2008).

NCAT Test Track

The original National Center of Asphalt Technology (NCAT) test track was constructed in 2000 in Opelika, Alabama. It is a closed-loop accelerated testing facility consisting of 46 test sections with a total length of 2.7 km. The test sections were loaded by conventional truck tractor-trailer vehicle trains. No environment control was carried out, but the pavement temperature, rainfall, and relative humidity were monitored continuously (Willis et al., 2009).

A variety of experiments have been conducted using the test track facility. The first phase of testing was focused on a study of surface mixture performance on perpetual pavements. Structural study on pavements with various thicknesses and material compositions was carried out during the second phase of testing to investigate the interaction between pavement response and performance. Instruments such as asphalt strain gages, earth pressure cells, and thermistor bundles were used to collect pavement critical responses (Timm et al., 2006). The third phase of testing continued to focus on structural study and on the calibration and verification of mechanistic-empirical (M-E) design concepts (Willis et al., 2009).

HVS at UCB Pavement Research Center (PRC)

In 1994, the California Department of Transportation (Caltrans), together with the Pavement Research Center (PRC) at University of California at Berkley, acquired two Heavy Vehicle Simulators, developed by the Council of Scientific and Industrial Research (CSIR) of South Africa. One is used to test full-scale pavements in a controlled laboratory environment. The other is used to test in-service pavements. Applied through a half axle using dual standard-size truck tires, the wheel load of the HVS is up to 200 kN (45 kip). The wheels can move in a unidirection or bi-direction (back and forth) manner and the maximum speed is 10 km/h or 1000 axles/hr. The HVS wheel path is 8.0-m (26.2-ft) long (Harvey et al., 2000). A number of

instruments are used to measure and monitor the pavement responses and conditions, including laser profilometer, road surface deflectometer (RSD), multi-depth deflectometer (MDD), thermocouples, and photographic surface crack monitoring equipment (Harvey et al., 2000).

Research on both asphalt and concrete pavement design and rehabilitation has been conducted using the HVS facilities. Some of the research projects include evaluation of overlay design using dense-graded asphalt concrete (DGAC) or asphalt rubber hot mix gap-graded for Caltrans, study of asphalt-treated permeable base (ATPB), comparison of AASHTO and Caltrans pavement design methods, study of fast-setting hydraulic cement concrete, and evaluation of the efficiency of dowel bar retrofitting of joints, etc. (Monismith et al., 2004).

Texas Mobile Load Simulator

The Texas Mobile Load Simulator program started in 1995. The TxMLS has six full-scale standard tandem axles traveling in one direction. It applies axle load of 150 kN and the tire pressure is 690 kPa (100 psi). The TxMLS can apply 6,000 axle loads per hour with nominal speed of 18 km/h (Chen and Hugo, 1998).

The TxMLS has been used to investigate load damage equivalency, determine remaining pavement life and its impact on rehabilitation guidelines, investigate new pavement materials, and study truck component-pavement interaction. Instruments and equipment such as multi-depth deflectometer, falling weight deflectometer, portable seismic pavement analyzer (PSPA), and Spectral analysis of surface waves (SASW) have been used in the TxMLS testing program to monitor pavement conditions (Fugo et al., 1999).

2.4.2 Small-Scale Accelerated Pavement Testing

Providing satisfactory scaling parameters, small-scale APT is expected to correlate with full-scale APT tests in predicting pavement performance in terms of permanent deformation (Kim et al., 1997). Small-scale APT is operated at a significantly lower cost compared to full-scale APT. The mobility of small-scale APT is also preferable when small-scale APT is used to test laboratory-constructed pavement structures.

The one-third scale Model Mobile Load Simulator (MMLS3), designed and manufactured by MLS Inc. in South Africa, has been used to assess field rutting and moisture damage and investigate structural distress of model pavements in the laboratory. It was found the MMLS3 test results were comparable to field performance under full-scale APT tests in terms of

ranking and extent (Martin et al., 2003). It is recognized that there is a trade-off between cost and capability. The MMLS3 is limited to testing scaled pavement structures in order to achieve similar stress distribution with full-scale APT in a pavement system.

2.5 Analysis and Modeling of Flexible Pavements

A flexible pavement is typically viewed as a structure with a relatively thin asphalt concrete layer lying above granular base and subbase to protect the soil subgrade from being overstressed. The flexible pavement's critical responses such as vertical compressive stresses/strains on top of the subgrade, vertical stresses/strains in granular base layers and asphalt concrete layer, and horizontal tensile strains at the bottom of the asphalt concrete layer are of great interest for pavement performance prediction. The critical responses of a flexible pavement are traditionally obtained through either layered elastic analysis or the relatively new numerical modeling approach.

2.5.1 Analysis of Flexible Pavements

Boussinesq's half-space theory assumes a homogenous media with an infinitely large area and an infinite depth. The half-space theory can be applied to flexible pavement analysis when the pavement is unsurfaced or the modulus ratio between the pavement and subgrade is close to unity. The Burmister's layered theory (1943, 1945) made it possible to conduct more realistic structural analysis on an actual flexible pavement, as a pavement is typically layered with better materials on top and not homogeneous from layer to layer.

Half-Space Theory

The original Boussinesq's theory was developed for a point load on an elastic half-space (i.e., force at a point of an indefinitely extended solid). The closed-form solution to the half-space problem indicates that the stress in the half-space is a function of vertical and radial distance to the loading point (or the origin in an axisymmetric coordinate) and independent of the stiffness of the media (Timoshenko and Goodier, 1951).

Foster and Ahlvin (1954) developed closed-form solutions to determine the vertical stress, horizontal stress, and vertical deflection due to the uniformly distributed circular load by integrating the stress components in Boussinesq's theory over the circular area. An assumption

of Foster and Ahlvin's work (1954) is that the Poisson's ratio of the half-space is 0.5 (i.e., the half-space is incompressible). Ahlvin and Ulery (1962) later improved the solution by taking into account effects of Poisson's ratio.

Layered Elastic Theory

Burmister (1943) presented an analytical approach to solve a two-layer system with a stiffer layer placed on top of another layer of infinite thickness. The elastic layered approach yields a more realistic solution than Boussinesq's half-space assumption, whereas vertical stresses, particularly at the interface, are overpredicted (Yoder and Witczak, 1975).

In 1945, Burmister extended the solution for a three-layer problem (Figure 4). The solution was derived on the basis of the following assumptions:

- Each layer is homogenous, isotropic, and linear elastic with a modulus of E and Poisson's ratio of μ.
- The media is weightless and infinite in the horizontal direction.
- Each layer has a finite thickness except that the bottom layer is infinite in depth.
- The layered system is uniformly loaded over a circular area with radius of *r* on the surface.
- Interfaces between two adjacent layers are assumed to be continuous: if the interface is fully bounded, the two layers at the interface have the same vertical stress, shear stress, vertical and horizontal displacements; if the interface is frictionless, the shear stress is zero at each side of the interface.

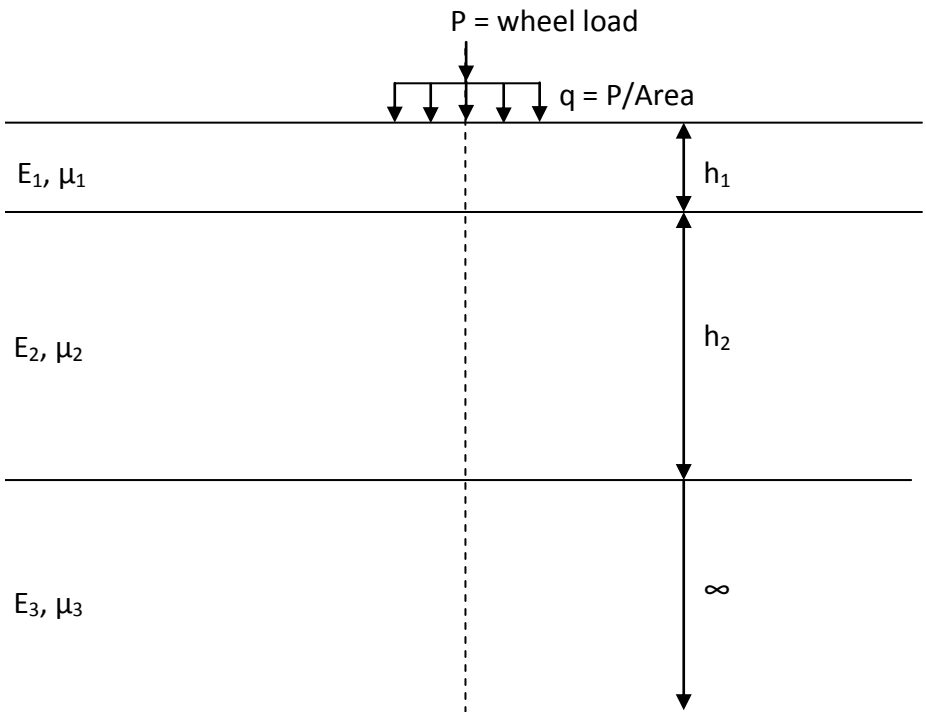

Figure 4. A general multilayered elastic system

On the basis of Burmister's elastic layered theory, a large number of computer programs were developed to solve for the stresses and strains of interest in a multi-layered pavement system. Some of the programs incorporated non-linear elastic behaviors of granular materials and viscoelastic material models for asphalt concrete. Multiple wheel loads were also considered in some of the programs. Among others, some of these elastic layered programs are listed below:

- CHEVRON (Warren and Dieckman, 1963)
- BISAR (De Jong et al., 1973)
- JULEA (Uzan, 1976)
- ELSYM5 (Kopperman et al., 1986)
- DAMA (AI, 1991)
- KENLAYER (Huang, 1993)

It is worthy of pointing out that pavement analysis based on layered elastic theory has several limitations due to the nature of the theory's assumptions. The actual pavement materials exhibit highly non-linear, stress-dependent or time-dependent behaviors instead of linear elastic behaviors. Self weight of pavement layers should be considered because of its effects on the stress-dependent granular materials and pavement dynamic responses. There also should be

boundaries in the horizontal direction. The asphalt concrete layer and granular layer may be partially bounded.

2.5.2 Finite Element Modeling for Flexible Pavements

Finite element (FE) modeling is a commonly used numerical approach to solve for a layered flexible pavement system. A variety of specialized FE codes were developed for analyzing flexible pavements. Following are some examples:

- ILLIPAVE (Raad and Figueroa, 1980)
- SENOL (Brown and Pappin, 1981)
- MICH - PAVE (Harichandran et al., 1990)
- GTPAVE (Tutumluer, 1995)

The emergence of general-purpose FE commercial packages promotes the usage of FE modeling in pavement analysis. The limitations of conventional pavement analysis based on the layered elastic theory as previously discussed can be overcome by incorporating more sophisticated material models and more realistic simulation into FE models for flexible pavements. ABAQUS, ANSYS, and ADINA are the commercially available FE packages that are being widely used in structural analysis of flexible pavements. Chen et al. (1995) conducted a comparison study between programs based on layer elastic theory (DAMA), specialized finite element programs (ILLIPAVE and MICH-PAVE), and a generalized program (ABAQUS). A close agreement in surface deflection profiles between MICH-PAVE and ABAQUS was found. Results between the layered elastic program and finite element programs generally showed discrepancies, while the results from ABAQUS were comparable to those from specialized FE programs.

In choosing appropriate FE models for pavements, several important aspects need to be taken into account, including pavement material behaviors, dimensionality of the FE model, and static or dynamic analysis. The following reviews of FE modeling for flexible pavements are focused on these aspects.

Pavement Material Models in FE

It is generally accepted that the pavement experiences not only elastic deformation but also plastic, viscous and viscoelastic deformation under cyclic traffic loading. The granular

pavement materials treated as continuum solids possess a stress-dependent nature, i.e. the strain is a nonlinear function of the stress state. The granular materials, moreover, exhibit direction-dependent (i.e., anisotropic) characteristics. Many specialized FE programs for pavement analysis have incorporated viscoelastic models for asphalt concrete and stress-dependent elastic models for granular materials. On the other hand, general-purpose FE programs consider a wide range of constitutive models for pavement materials: linear and nonlinear elastic, viscoelastic, and elastoplastic. While there are numerous successful examples of simulating nonlinear behaviors of pavement materials (Zaghloul and White, 1993; Taciroglu, 1998; Uddin and Ricalde, 2000; Schwartz, 2002; Mun, 2003; Kim, 2007; Liao, 2007), described below are some of the recent and representative work that took use of the up-to-date testing and modeling tools.

Using ABAQUS, Liao (2007) employed a linear viscoelastic model-generalized Maxwell model for simulating the hot-mix asphalt in the pavement. Accurately simulating a pavement requires both appropriate material characterization and an accurate mechanistic model. The HMA viscoelastic material properties were characterized through frequency-sweep dynamic modulus testing at different temperatures by following the NCHRP (2002) procedures. The tests yielded values of dynamic modulus ($|E^*|$) and phase angle (φ) at different loading frequencies and testing temperatures. A master curve of relaxation modulus, E(t) in the time domain was obtained through a conversion procedure from the dynamic modulus in the frequency domain (Schapery and Park, 1999). Shear modulus can be calculated from the relaxation modulus with a Poisson's ratio. The time-dependency, in ABAQUS, is expressed through Prony series in terms of shear moduli. A five-term Prony series was developed to define the stress-strain relationship and incorporate it into the ABAQUS FE model. The model was calibrated (fine tuned) to field pavement responses measured from instruments. The calibrated FE model was then used to conduct parametric studies to study effects of layer thickness, layer modulus, pavement temperature, etc.

Besides the asphalt concrete behaviors, the characteristics of unbound granular materials are another important factor in mechanistic analysis of pavement structures. It is widely recognized that unbound granular materials exhibit resilient behavior after the initial stage of cyclic loading. Many nonlinear elastic models have been developed to take into account the effects of stress dependency in the form of resilient modulus for granular pavement materials (Seed, 1967; Hicks and Monismith, 1971; Uzan, 1985; Witczak and Uzan, 1988; NCHRP, 2004).

ABAQUS provides the interface for users to implement specialized material constitutive laws. A user material subroutine (UMAT) can be written in FORTRAN to define the stress-strain relationship of the material. The subroutine is called by ABAQUS at all calculation points to update the stresses and solution-dependent state variables at each increment. Kim (2007) developed a user material subroutine for the nonlinear Uzan (1985) model and incorporate it into ABAQUS FE models. The subroutine calculated the resilient modulus and updated the stiffness matrix at each iteration for each integration point based on the stress state. The new resilient modulus was then used to calculate the stress and strain for the next iteration until the convergence. Thus, the ABAQUS FE model was able to address the variation of resilient modulus in both vertical and horizontal directions within the base layer. It was found that there were significant effects of nonlinear elastic models on pavement critical responses, by contrast to solutions from linear elastic analysis.

Dimensionality of the FE Model

Depending on the boundary conditions (loading configurations and pavement geometries), a pavement can be simulated in two-dimensional or three-dimensional FE models. Two-dimensional axisymmetric FE models are commonly used when a half single-axle load (i.e., one wheel load) is applied to the pavement and the load is assumed to be circularly distributed. Although the superposition of 2-D axisymmetric FE solutions, especially from nonlinear models, generally introduces some errors, the 2-D model is routinely used for practical design calculations due to its simplicity (Schwartz, 2002; NCHRP, 2004).

More sophisticated three-dimensional FE models have been increasingly used to simulate flexible pavements. The nonlinear 3-D FE modeling was even recommended as a practical engineering tool for pavement design when computational power allows (GAO, 1997). While 3-D FE modeling requires more computation time and memory, it has the flexibility to take into account versatile loading configurations (both multiple wheel loads and nonsymmetrical loading areas), tire-pavement interaction, and pavement discontinuity (cracking).

Static vs. Dynamic Analysis

Pavements under vehicle loading have been traditionally modeled as static systems for response analysis. The effects of load-time history are neglected in a static analysis, which is not

in accordance to the realistic responses of time-dependent asphalt concrete. Furthermore, the mass inertial and damping forces may significantly influence the pavement responses, considering the fact that natural frequency of flexible pavement (6 to 12 Hz) can be close to the vehicle loading frequency depending on the vehicle speed (Gillespi et al., 1993; Uddin, 2003). A study by Yoo and Al-Qadi (2007) revealed that the critical pavement responses such as tensile strains at the bottom of asphalt concrete and compressive strains at the top of subgrade are underestimated compared to those from a dynamic analysis. Uddin and Garza (2002) conducted dynamic analysis on airfield pavements subjected to FWD loading. With the FWD load history in dynamic analysis, results of dynamic analysis showed a closer match with the measured surface deflection profile than the results from static analysis. Thus, the backcalculation procedures with the aid of dynamic modeling could more accurately estimate pavement layer properties.

2.5.3 Finite Element Modeling for Geogrid-Reinforced Flexible Pavements

As a powerful tool to study the mechanistic behaviors of a pavement system, finite element modeling has been used to investigate geogrid-reinforced flexible pavements. Although geogrids are actually a mesh-like structure with openings, they are typically treated as continuous membranes within the FE models. The interlocking mechanisms through which the geogrid provides lateral confinements to granular aggregates cannot be directly simulated under the assumptions of continuum mechanics for FE modeling.

Wathugala et al. (1996)

Using ABAQUS, axisymmetric FE models were created to simulate reinforced flexible pavements by geogrids placed at the base-subgrade interface. The elasto-plastic Drucker-Prager model was used for asphalt concrete and base aggregates while the subgrade soil was simulated by the Hierarchical Single Surface (HiSS) model developed by Wathugala and Desai (1993). Better pavement performance in terms of rutting resistance was predicted with stiffer geogrids. Results from the FE models using elasto-plastic models were compared with the results from linear elastic models and more significant improvements in pavement performance was found.

Perkins et al. (2004)

The purpose of this study was to develop a design method for geosynthetic-reinforced flexible pavements within the context of the *Mechanistic-Empirical Pavement Design Guide* . As one of the ME design components, 2-D axisymmetric FE models for unreinforced pavements were created in ABAQUS by following the guidelines used by the design guide for nonlinear response models (NCHRP, 2004). Recognizing that a simple response model for reinforced pavements did not adequately address the benefits of geogrid reinforcements, the researchers developed a multi-step simulation procedure to account for the effects of compaction and traffic loading on the development of confinement of the base aggregates from geogrids.

Geogrids were simulated as linear elastic membranes in this study. Contacts based on the Coulomb friction model were assigned to the upper and lower surfaces of the geogrid and the adjacent pavement layers. Through the multi-step FE modeling, the interface shear stresses increase with the compaction and the traffic load repetitions. The development of the interface shear stresses contributes to the lateral confinement of base aggregates. Reasonable agreement in surface permanent deformation was obtained between the measurements from testing sections and the results from predictive models based on critical pavement responses extracted from the FE models.

Leng and Gabr (2005)

Aimed at investigating geogrid-reinforcing effectiveness within unpaved roads built over soft subgrade, FE models were created using the FE package ABAQUS. The built-in Drucker-Prager model with hyperbolic yield criterion was used for pavement base materials to minimize the unrealistic tensile stresses in the base. The geogrid was modeled as membranes that take tension only. A Coulomb friction model was adopted to simulate the shear resistance behavior of the interface between the base layer and geogrids. A friction coefficient value and allowed elastic slip/relative displacement were assigned to the interface model.

The FE models showed the benefits of geogrids by decreased surface deflection and improved vertical stress distribution over the top of subgrade. Higher geogrid modulus and interface friction led to lower vertical stress at the top of subgrade. A parametric study conducted using the FE models showed that the geogrid-reinforcing effectiveness was mostly affected by the aggregates base thickness and the base/subgrade modulus ratio.

Saad et al. (2006)

Saad et al. conducted a dynamic 3-D FE modeling on geosynthetic-reinforced flexible pavements using the commercial FE program ADINA. The aggregate base was treated using the elastoplastic Drucker-Prager model and the subgrade soil was model by the modified CamClay model. Both the asphalt concrete and geosynthetic were treated as linear elastic. Dynamic load with a triangular wave having duration of 0.1 second was applied to the pavement model. The pavement layers-geosynthetic interface was assumed to be fully bounded. A parametric study was carried out to investigate the factors such as base quality and thickness and subgrade quality that influence the reinforcing effectiveness of geosynthetics.

Kwon (2007)

An axisymmetric FE model was developed to investigate the benefits of geogrid reinforcement for base layer in terms of pavement mechanistic responses. The asphalt concrete was modeled as isotropic linear elastic. A nonlinear, stress-dependent material model was adopted for the base aggregates and subgrade soil. Anisotropy of the base aggregates was also considered in the FE model. The geogrid was simulated using membrane elements with finite thickness. A prominent character of the model is the inclusion of "locked-in" horizontal residual stresses in the vicinity of geogrids, which simulates the stiffening effects of geogrid reinforcements induced by construction and trafficking. The residual stress was applied to a layer of base course above the geogrids as an initial condition. The FE models were calibrated and validated by field measurements of pavement responses from a full-scale accelerated pavement testing.

2.6 Permanent Deformation Models for Unbound Pavement Layers

Many factors affect the permanent deformation behaviors of unbound pavement layers such as number of load repetitions, the stress state due to the loading magnitude, loading rate and history, temperature and moisture conditions. Furthermore, some properties of the unbound material play an important role in permanent deformation behaviors of the unbound layer: grain size distribution, content of fines, the degree of compaction, grain shape and surface roughness, etc. (Lekarp et al., 2000). While it is almost impossible for a permanent deformation model to

take into account all the factors above, most of the existing permanent deformation models account for one or more than one critical factor.

Barksdale (1972)

As one of the earliest permanent deformation models developed for unbound pavement materials, Barksdale's model (1972) suggests that the accumulation of permanent deformation is linearly increased with the logarithm of the number of load repetitions:

$$\varepsilon_p = a + b \log(N) \quad (1)$$

where:

ε_p = permanent axial strain

a = calibration parameter

b = calibration parameter

N = number of load repetitions

Monismith et al. (1975)

A log-log relation between the permanent strain and number of load repetitions was suggested by Monismith (1975) as follows:

$$\varepsilon_p = aN^b \quad (2)$$

where:

ε_p = permanent axial strain

a = calibration parameter

b = calibration parameter

N = number of load repetitions

It is noted that both models developed by Barksdale and Monismith describe the relationships between the accumulation of permanent deformation and number of load repetitions. Other factors that may affect the development of the permanent deformation are not explicitly included in the models.

Tseng and Lytton (1989)

Tseng and Lytton (1989) developed a permanent deformation model based on the statistical analysis of a database of cyclic triaxial tests results:

$$\varepsilon_a = \left(\frac{\varepsilon_0}{\varepsilon_r}\right) e^{-\left(\frac{\rho}{N}\right)^{\beta}} \varepsilon_v h \quad (3)$$

where: ε_a = permanent strain

ε_r = resilient strain imposed in laboratory test

ε_v = average vertical resilient strain in the layer

ε_0, β, ρ = material parameters

N = number of load applications

h = layer thickness

The three material parameters (ε_0, β, ρ) are related to the material properties such as water content, resilient modulus, and stress states of the laboratory testing. The three material parameters are differently associated with the material properties and stress states for granular materials and subgrade soil. The parameters are expressed as below for granular materials:

$$\log\left(\frac{\varepsilon_0}{\varepsilon_r}\right) = 0.80978 - 0.06626 W_c - 0.003077 \sigma_\theta + 0.000003 E_r \quad (4)$$

$$\log\beta = -0.9190 + 0.03105 W_c + 0.001806 \sigma_\theta - 0.0000015 E_r \quad (5)$$

$$\log\rho = -1.78667 + 1.45062 W_c + 0.0003784 \sigma_\theta - 0.002074 W_c^2 \sigma_\theta - 0.0000105 E_r \quad (6)$$

For subgrade soil, the three parameters are expressed as follows:

$$\log\left(\frac{\varepsilon_0}{\varepsilon_r}\right) = -1.69867 - 0.09121 W_c - 0.11921 \sigma_d + 0.91219 E_r \quad (7)$$

$$\log\beta = -0.9730 + 0.00000278 W_c^2 \sigma_d + 0.017165 \sigma_d + 0.000033 W_c^2 \sigma_\theta \quad (8)$$

$$\log \rho = 11.009 + 0.000681 W_c^2 + \sigma_d - 0.40260 \sigma_d + 0.000054 W_c^2 \sigma_\theta \quad (9)$$

where:

W_c = moisture content

σ_d = deviatoric stress

σ_θ = bulk stress

E_r = resilient modulus

It is worth pointing out that the model developed by Tseng and Lytton considers both the materials properties and stress states in addition to the number of load applications.

Theyse (1997)

Based on the results of accelerated testing using a heavy vehicle simulator, Theyse (1997) developed a permanent deformation model for pavement subgrade:

$$PD = e^{c} N^{s} \left(e^{B\sigma_c} - 1 \right) \quad (10)$$

where:

PD = permanent deformation

N = number of load repetitions

σ_c = vertical compressive stress on top of the subgrade

c, s, B = regression parameters

As typically vertical compressive strains are adopted in the permanent deformation models, a better correlation was found between the vertical stress and the resulting permanent deformation. Thus, the vertical stress was considered a critical parameter in the model.

Lekarp and Dawson (1998)

The shakedown concept suggests that a pavement is subjected to an incremental accumulation of plastic strains when the magnitude of the load is greater than a certain value, so-called shakedown limit. If the load is lower than the shakedown limit, the plastic strain tends to

level off and the pavement is considered to be in the state of shakedown. Lekarp and Dawson adopted the shakedown principles in modeling the permanent deformation behaviors of unbound pavement layers. A model describing the relationships between the permanent strain accumulation, the stress path length, and the maximum shear-normal stress ratio was proposed by Lekarp and Dawson:

$$\frac{\varepsilon_p(N_{ref})}{L/p_0} = a\left(\frac{q}{p}\right)_{mzx}^{b} \quad (11)$$

where:

$\varepsilon_p(N_{ref})$ = permanent axial strain at a given reference number of load applications N_{ref}, N_{ref} >100

L = length of stress path

p_0 = reference stress

q = deviator stress, $(\sigma_1 - \sigma_3)$

p = mean normal stress, $\frac{\sigma_1 + 2\sigma_3}{3}$

$(\frac{q}{p})_{max}$ = maximum stress ratio

a, b = calibration parameters

NCHRP 1-37A (2004)

The research team for NCHRP 1-37A adopted the framework of the model in Equation 3 developed by Tseng and Lytton (1989) for permanent deformation models in the MEPDG. Modifications were made to Tseng and Lytton's original model to accommodate the calibration and field measurements. The major changes were the unification of the separate models for granular base materials and subgrade materials and the elimination of the stress terms in the original models. The three material parameters (ε_0, β, ρ) for both granular base and subgrade materials were determined as follows:

$$\log \beta = -0.61119 - 0.017638\, W_c \quad (12)$$

$$\log\left(\frac{\varepsilon_0}{\varepsilon_r}\right)=\frac{(e^{(\rho)^{\beta}}*a_1E_r^{b_1})+(e^{(\rho/10^9)^{\beta}}*a_9E_r^{b_9})}{2} \quad (13)$$

$$C_0=\ln\left[\frac{(a_1E_r^{b_1})}{(a_9E_r^{b_9})}\right] \quad (14)$$

$$\rho=10^9\left[\frac{C_0}{(-(10^9)^{\beta})}\right]^{\frac{1}{\beta}} \quad (15)$$

$$W_c=51.712\left[\left(\frac{E_r}{2555}\right)^{\frac{1}{0.64}}\right]^{-0.3586*GWT^{0.1192}} \quad (16)$$

where: W_c = water content, %

E_r = resilient modulus of the layer, psi

GWT = ground water table depth, ft

a_1 = 0.15

b_1 = 0.0

a_9 = 20.0

b_9 = 0.0

By adding a calibration factor to the original Tseng and Lytton's model (1989), the permanent deformation model for MEPDG is:

$$\delta_a=\beta_{cal}\left(\frac{\varepsilon_0}{\varepsilon_r}\right)e^{-\left(\frac{\rho}{N}\right)^{\beta}}\varepsilon_v h \quad (17)$$

within which β_{cal} = 1.673 for unbound granular base materials and 1.35 for subgrade soils. The two calibration constants were obtained on the basis of observations and measurements of pavement sections from the Long-term Pavement Performance (LTPP) program. The two calibration constants are considered national factors by NCHRP 1-37A.

It should be noted that the permanent deformation model for unbound pavement layers developed by the NCHRP 1-37A project is one of the most recent models of this type and widely recognized. The model has been calibrated for local pavements by many state agencies. However, the permanent deformation model for unbound pavement layers could be improved by incorporating a shear strength term (Witczak, 2005).

3 RESEARCH APPROACH AND EXPERIMENT DESIGN

This chapter describes the research approach and experiment design adopted in this study. Some important aspects and considerations of the experimental methodologies are addressed in this chapter.

3.1 Research Approach

The flowchart presented in Figure 5 shows the framework of the research approach and experiment design of this study. One of the unique aspects of the approach for this research is the multi-scaled tests on geogrids, including index tests for physical and mechanical properties of geogrids, bench-scale tests on characterizing the interface between geogrid and surrounding pavement materials, and performance-based accelerated pavement tests. The critical geogrid characteristics are expected to be identified by an analysis of correlation among the tests conducted at different scales, which will be incorporated into the permanent deformation models for geogrid-reinforced flexible pavements.

Finite element models are created to simulate the pavement responses under the conditions of the accelerated testing. The inputs of geogrid properties and interface characterizations for the FE models are based on the results of index and bench-scale tests on geogrids. The properties of pavement layers are obtained through an inverse analysis procedure in conjunction with lightweight deflectometer (LWD) tests. The primary function of the FE model in this study is to provide critical pavement responses (i.e., vertical strains) for developing the mechanistic-empirical permanent deformation models.

With existing permanent deformation models for unreinforced flexible pavements as the starting point, the permanent deformation models were assessed and customized for geogrid-reinforced flexible pavements. The pertinent variables in the permanent deformation models for geogrid-reinforced flexible pavements are identified according to the accelerated testing conditions. In addition, the permanent deformation models will be able to reflect the inclusion of geogrid reinforcement and the effects of geogrid characteristics on geogrids' performance.

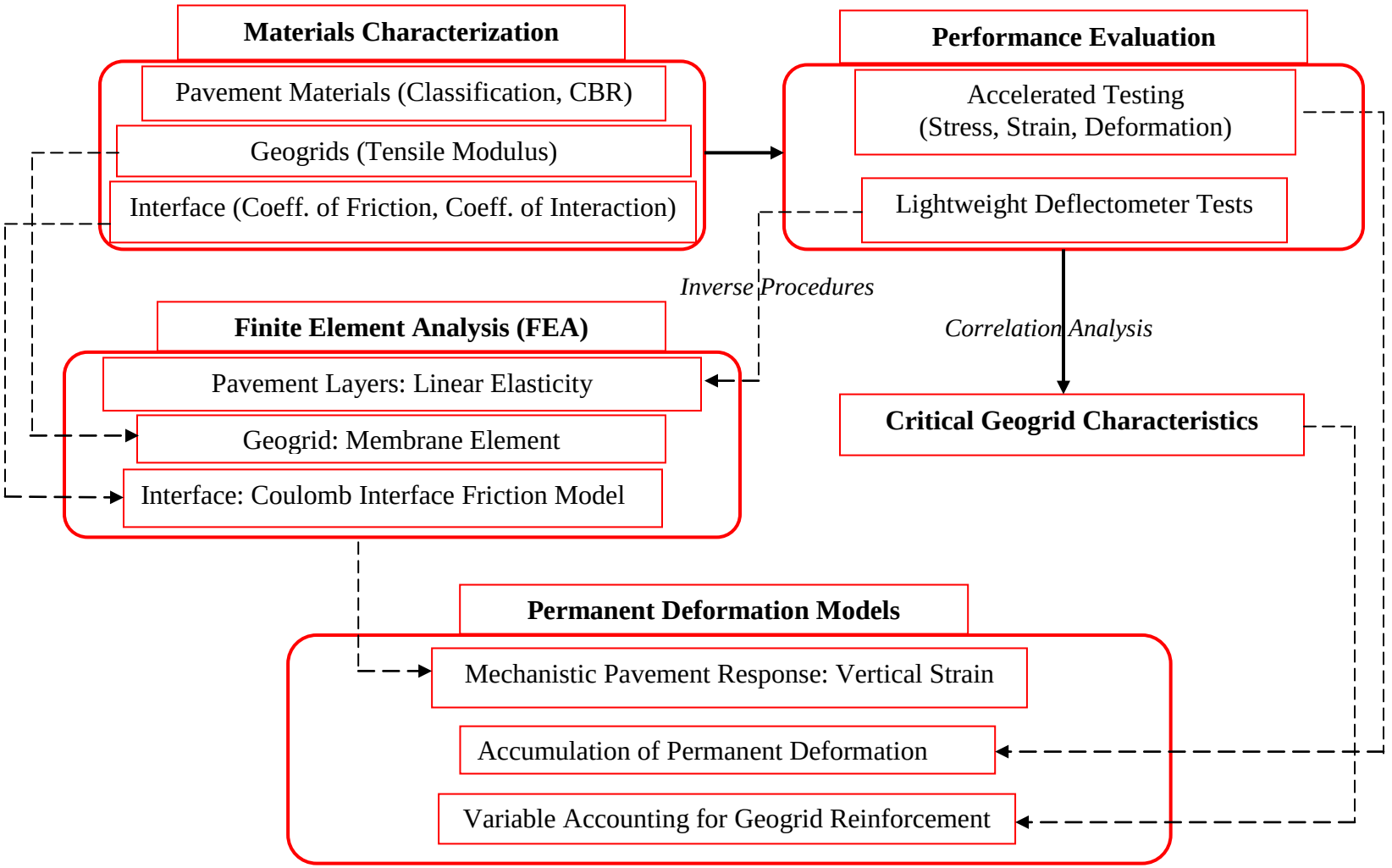

Figure 5. Framework of the experiment design and research approach of this study

3.2 Geogrids Materials and Interface Characterization

3.2.1 In-Air Tests for Index Properties of Geogrids

In-air index tests were conducted for geogrids in accordance to either ASTM standards or Geosynthetic Research Institute (GRI) standards, as listed in Table 2. The physical and mechanical properties of geogrids were tested in both machine direction (MD) and transverse/cross-machine direction (XMD). The in-air index tests were conducted for three different geogrid products (designated as Grid A, Grid B, and Grid C) that were subsequently used in bench-scale tests and the accelerated pavement testing.

Table 2. Tested index properties of the geogrids*

Index Property	Test Method
Aperture size (mm)	Calipers
Rib thickness (mm)	Calipers
Junction thickness (mm)	ASTM D 5199
Mass per unit area (g/m^2)	ASTM D 5261
Tensile strength at 2% strain (kN/m)	ASTM D 6637
Tensile strength at 5% strain (kN/m)	ASTM D 6637
Ultimate tensile strength (kN/m)	ASTM D 6637
Elongation at break (%)	ASTM D 6637
Junction strength (kN/m)	GRI GG2
Flexural rigidity (mg-cm)	ASTM D 1388, mod.
Torsional stiffness (cm-kg/degree)	GRI GG9

*Note: Tests listed in the table were performed by TRI/Environmental, Inc.

In addition to the standard index tests listed above, the mechanical tensile properties of geogrids were tested at the maximum load that the geogrid is expected to be experienced in the performance-based accelerated testing. The static tensile tests will be conducted for each geogrid product in both machine and cross-machine directions.

3.2.2 Bench-Scale Tests for Geogrid-Pavement Materials Interfaces

While the index properties of geogrids tested in air indicate the physical and mechanical characterizations of geogrids to some extent, the index properties alone may not be sufficient to predict how well a geogrid will perform within the medium of pavement materials. The interaction between geogrids and the surrounding medium is one of the primary reinforcing mechanisms through which the geogrid provides lateral

restraints to the surrounding medium and consequently mitigates the permanent deformation. Therefore, it is important to characterize the interface between geogrids and surrounding pavement materials for the application of geogrid in reinforcing flexible pavements.

There are two ASTM standard testing methods available to investigate the interactive behaviors between geogrids and external mediums: pullout tests (ASTM D 6706) and direct shear tests (ASTM D 5321). Pullout tests are carried out to characterize the geogrid-aggregate interface, while direct shear tests are performed for the aggregate-geogrid-soil interface. The two tests will be conducted for the geogrids, aggregate and soil that will be used in the accelerated testing. One aggregate material, two types of soil (designated as Soil CL and Soil ML), and three types of geogrid products are involved in the accelerated pavement testing. The interface between the pavement materials and three of the geogrid products were tested through pullout and direct tests, as listed in Table 3.

Table 3. Tested interfaces through pullout and direct shear tests

Pullout Tests	**Direct Shear Tests**	
Agg.-Grid A	Soil CL-Grid A-Agg.	Soil ML-Grid A-Agg.
Agg.-Grid B	Soil CL-Grid B-Agg.	Soil ML-Grid B-Agg.
Agg.-Grid C	Soil CL-Grid C-Agg.	Soil ML-Grid C-Agg.
	Soil CL - Agg.	Soil ML – Agg.

3.3 Accelerated Testing

Following the index and bench-scale tests on geogrids, it is natural to perform further tests on geogrids under the conditions that are the same or similar with what experienced by geogrids within a flexible pavement system. Such tests on geogrids installed in a pavement system will comprehend characterizing geogrids. Accelerated testing will be carried out to test layered model pavements by using the one-third scale model mobile load simulator (MMLS3). The model pavements will be constructed in a pit with reinforced concrete walls.

3.3.1 Scaling Factors of Accelerated Testing using MMLS3

The MMLS3 is an accelerated pavement testing device that applies unidirectional trafficking to the pavement in a controlled laboratory environment. Accelerated pavement testing offers excellent means to conduct pavement performance tests and has been used to evaluate pavement performance and products since 1909 in the United States (Metcalf, 1996). The advantages of APT over full-scale testing are the ability to conduct performance tests at much lower costs over a shorter time period, and the ability to control the loading environmental conditions.

The MMLS3 applies a wheel load of 2.7 kN with a contact pressure of 690 kPa (100 psi) roughly representing $1/9^{th}$ of the loading conditions applied by a standard full-scale single tire ($1/4^{th}$ dual-tire equivalent single axle load, ESAL). In an effort to attain similitude between the scaled slabs and actual field slabs in terms of the stress state, the thickness of each layer should be scaled approximately to $1/3^{rd}$ of that in the field (Martin et al., 2003). It should be noted that the gradation of the pavement materials and geometry of the geogrid are not scaled, while the structural thickness of the pavement is accordingly reduced. Therefore, compared to a full-scale pavement system, it suspects that the reinforcing effects due to the interaction between the geogrid and pavement materials are enhanced within the scaled-down pavement system.

3.3.2 Accelerated Pavement Testing Matrix

A total of four sets of accelerated tests were carried out. The first two sets were conducted as exploratory tests to obtain an insight into the performance of geogrid in reinforcing weak pavement subgrade. The subsequent two sets of accelerated tests were conducted to investigate the permanent deformation behaviors of geogrid-reinforced flexible pavements. The pavements and geogrids were instrumented by various sensors to monitor the responses of the pavement system to the MMLS3 cyclic load. Table 4 lists the information on all the sections that were subjected to the accelerated testing. For each set of APT testing, four pavement sections were constructed and tested. Among the four sets of accelerated tests, sections of the exploratory APT I were all reinforced with different geogrid products while there was a control section of the other sets, as listed in Table 4.

Table 4. Pavement sections subjected to accelerated testing

APT	AC Thickness (cm / in)	Base Course Thickness (cm / in)	Subgrade Thickness (cm / in)	Subgrade Soil	Subgrade CBR (%)	Sections
Instrumented APT I	3.8 / 1.5	10.2 / 4.0	113.0 / 44.5	Soil 2 Clay of Low Plasticity (CL) /A-4(5)	3	Grid A Grid B Grid C Control
Instrumented APT II	3.8 / 1.5	10.2 / 4.0	113.0 / 44.5	Soil 3 Silt (ML) /A-4(4)	1.5	Grid A Grid B Grid C Control

3.4 Development and Calibration of a Pavement Response Model using the Finite Element Method

In order to develop mechanistic-empirical permanent deformation models for the reinforced and unreinforced flexible pavement sections, mechanistic responses (typically, resilient strains at the mid-depth of the pavement layer or sub-layer) are required. They can be calculated from the response model. Finite element models were created to simulate the accelerated pavement sections with and without geogrid reinforcements at the base-subgrade interface. The pavement sections were assumed to be axisymmetric in the FE models for the purpose of saving computational efforts. Pavement materials were considered as linear elastic and the geogrids were modeled as continuous membranes.

An inverse analysis procedure was adopted to calibrate the pavement layer elastic moduli values. Measurements during the lightweight deflectometer testing were used to compare against the corresponding calculated values from the FE model. In this study, the surface deflection at the center of the LWD load, the deflection on top of the subgrade, and the vertical stress on top of the subgrade were measured when the pavement was subjected to the LWD load. The pavement layer elastic moduli were tuned until by minimizing the difference between the measured and the calculated values.

3.5 Identification of Calibration Factors for Selected Permanent Deformation Models

The permanent deformation models in MEPDG (NCHRP, 2002) were adopted and customized to accommodate the testing conditions in this study. Considering that the geogrids are used primarily for stabilizing weak subgrade in this study, it would be logical to address the effects of geogrid reinforcements on the pavement subgrade permanent deformation. However, due to the lack of measurements on deformation of the base course layer, permanent deformation models were not developed for the base layer and subsequently the asphalt concrete layer.

Although a national calibration factor (β_{cal}) was given in MEPDG for soil subgrade permanent deformation model (refer to Equations 12 through 17), it was imperative to recalibrate the model with regard to the special testing conditions in this study. In addition, the subgrade permanent deformation model was simplified by eliminating a term ($\frac{\varepsilon_0}{\varepsilon_r}$) that is associated with laboratory tests and not applicable to this study. The zero values of parameters b_1 and b_9 result in the independency of the constant C_0 on the elastic modulus included (see Equation 14). It was decided to set the two parameters b_1 and b_9 as calibration factors in this study to account for the stiffness of the subgrade in the model, although the vertical resilient strain from the response model as one of the inputs already took into account effects of the subgrade modulus. Therefore, there were three calibration factors for each section: β_{cal}, b_1, and b_9.

4 MATERIALS CHARACTERIZATION

The materials used for the bench-scale and accelerated pavement testing in this study include soils commonly found in Pennsylvania, crushed stone aggregate, and hot-mix asphalt. Three different soils (designated as Soil 1, Soil 2, and Soil 3), one aggregate, one HMA and four different PennDOT-approved geogrid products (designated as Grid A, Grid B, Grid C, and Grid D) were used throughout the study.

4.1 Pavement Materials Characterization

The same type of HMA and aggregates were used for all the accelerated testing sections throughout this study. Subgrade soil was considered a variable of pavement material in this study. Therefore, laboratory characterization tests were performed only for the three different types of subgrade soil.

4.1.1 Subgrade soil

Three different types of soil as pavement subgrade were used in order to examine the soil effects on the reinforcing effectiveness. The soil was obtained from local construction sites representing common soil types in central Pennsylvania. The soils are designated as Soil CL and Soil ML. The local sources of the three soils are: Science Park Road and University Drive, respectively. Sieve analysis and Atterberg limits tests were conducted to classify the three soil types. The particle size distribution for the soil is presented in Figure 6. According to the Unified Soil Classification System (USCS), they are classified as lean clay with sand (CL) and silt with sand (ML) per ASTM D 2487, A-2-3, A-4(5), and A-4(4) according to ASSHTO M 145 for Soil CL and Soil ML, respectively. Table 2 lists the properties of the three subgrade soils.

Standard Procter tests (ASTM D 698) for the three types of soil yielded similar laboratory compaction characteristics between Soil CL and Soil ML, as Figure 7 shows. The optimal moisture content and maximum dry density obtained from the tests are listed in Table 5.

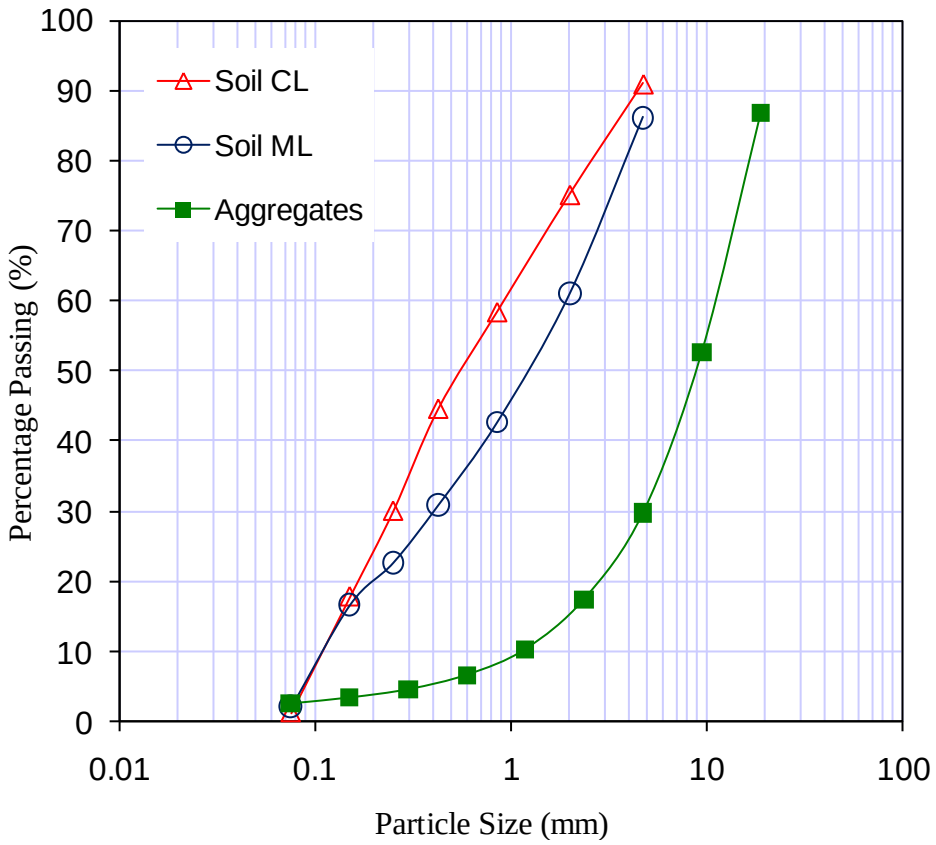

Figure 6. Particle size distribution for soil and aggregates used in this study

Table 5. Soil properties

Soil	**Classification USCS/AASHTO**	**Percentage of Passing No. 200 Sieve (0.075mm) (%)**	**Plasticity Index (%)**	**Optimal Moisture Content (%)**	**Maximum Dry Density (kg/m^3)**
Soil CL	Clay of Low Plasticity (CL) / A-4(5)	77.6	22.7	18	1700
Soil ML	Silt (ML)/ A-4(4)	83.2	4.4	19	1690

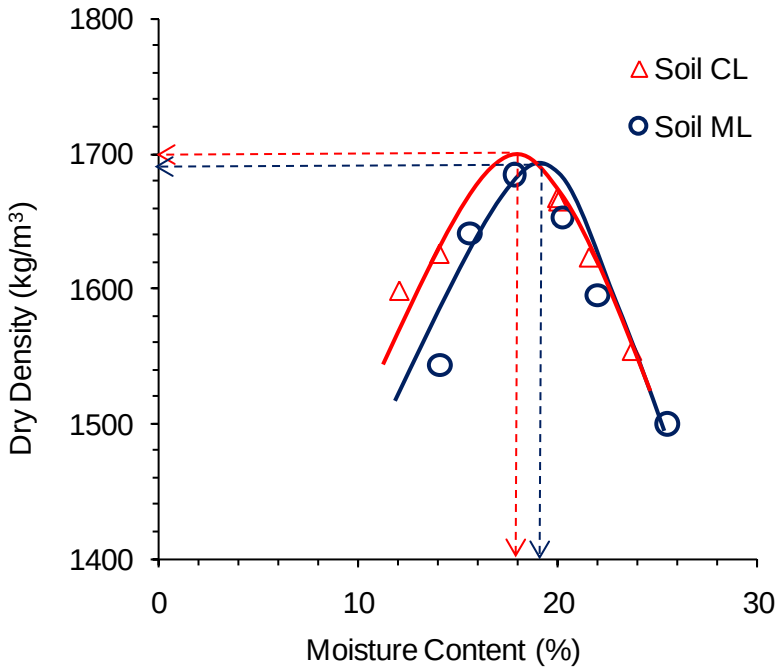

Figure 7. Proctor test results for subgrade soils

A set of laboratory unsoaked CBR tests (ASTM D 1188) were performed for the soil at different water contents, as shown in Figure 8. The trend shows that CBR decreases significantly with increase in water content beyond the optimum water content, indicating the soil is water sensitive. Hence, the soil is compacted at a water content greater than optimum to induce weak soil subgrade conditions.

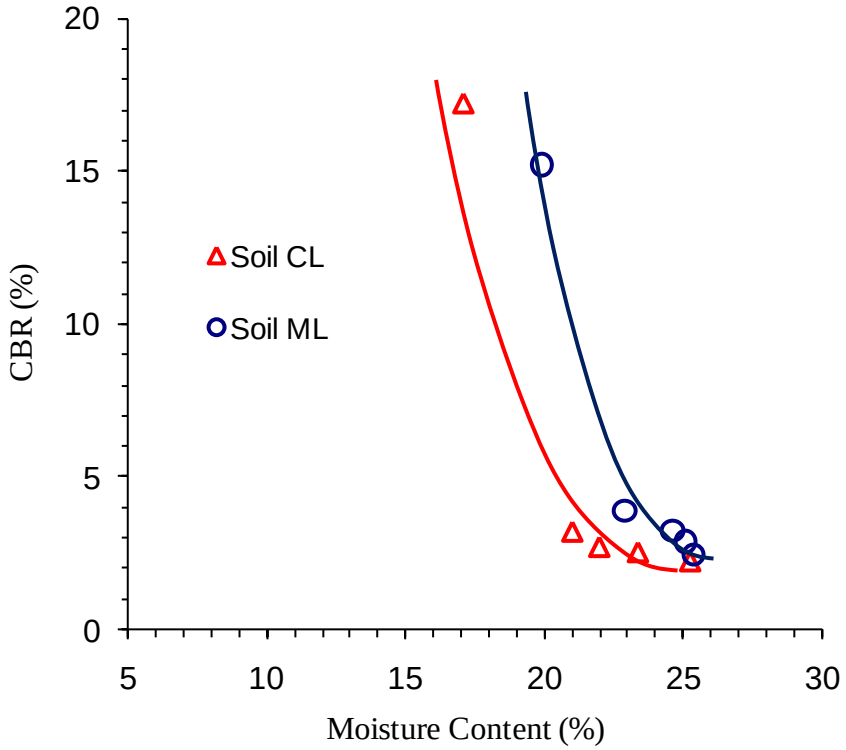

Figure 8. Variation of soil CBR with moisture content

4.1.2 Base Course Aggregates

Dense-graded crushed stone was used as the pavement aggregate base layer. The grain size analysis (Figure 6) shows that the base course aggregate meets the Pennsylvania Department of Transportation (PennDOT) 2A grading requirement. A standard Proctor test for the aggregates yielded optimum moisture content of 3.9% and maximum dry density of 2329.1 kg/m^3.

4.1.3 Asphalt Mixture

The 9.5 mm HMA was provided by the local mixture plant, HRI Inc. The asphalt mixture had a theoretical maximum specific gravity of 2.532, which was used to check the air void percentage for the subsequent compactions of asphalt concrete.

4.2 Geogrids Index and Mechanical Properties

In-air index properties of geogrids were tested according to ASTM standards or standards set forth by the Geosynthetic Research Institute (GRI). Furthermore, the

geogrids were subjected to wide-width tensile tests at small displacement that is more pertinent to the application in pavements.

Four commonly used biaxial geogrid products were selected for this study and are herein designated as Grid A, Grid B, and Grid C. Grid A was composed of high-tenacity polyester (PET) multifilament yarns with junction knitted together and coated with a polyvinyl chloride (PVC) coating. Grid B was made by punching patterned holes into polypropylene (PP) sheets and biaxially drawing the sheets under controlled temperatures and strain rates. Grid C was made of PET multifilament yarns that are woven into a network. Grid C was coated with a polymer coating. Based on the measured flexural rigidity per ASTM D 1388, Grid A and Grid C were classified as flexible geogrids, while Grid B was classified as a stiff geogrid (Koerner 1998).

4.2.1 Index Tests

Index tests were performed on the three biaxial geogrid products to determine their physical and mechanical properties. Testing was conducted by TRI/Environmental Inc. following ASTM standards as well as standards set forth by the Geosynthetic Research Institute. Properties measured from index tests are the most commonly used criteria in specifications for use of geogrid products by state highway agencies.

Table 6 lists the index tests conducted on the three geogrid products, standard test protocols followed, along with the measured values of physical and mechanical properties. Properties were tested in both machine direction and cross-machine direction if applicable. As can be seen in Table 6, the aperture size of all of the geogrids was greater than 25.4 mm (1 inch). However, most of the base aggregates prepared in accordance with PennDOT 2A passed the 19.05-mm (0.75-inch) sieve. Recall that interlocking effects are influenced by the size ratio of geogrid aperture to PennDOT 2A base aggregate particle diameter.

Table 6. Geogrid index properties

Index Property	Test Method	Grid A		Grid B		Grid C	
		MD*	TD**	MD	TD	MD	TD
Aperture size (mm)	Calipers	25.65	26.42	25.65	36.58	27.18	28.96
Rib thickness (mm)	Calipers	1.42	2.03	1.60	1.07	0.76	1.12
Junction thickness (mm)	ASTM D 5199	1.55		3.94		1.17	
Mass per unit area (g/m^2)	ASTM D 5261	350.93		319.06		298.37	
Tensile strength at 2% strain (kN/m)	ASTM D 6637	10.3	11.2	9.8	15.6	7.5	10.1
Tensile strength at 5% strain (kN/m)	ASTM D 6637	18.1	17.4	16.8	29.2	13.1	14.1
Ultimate tensile strength (kN/m)	ASTM D 6637	39.5	52.8	23.9	32.9	33.3	57.8
Elongation at break (%)	ASTM D 6637	10.5	12.0	20.6	10.9	10.5	14.0
Junction strength (kN/m)	GRI GG2	7.4	7.1	17.7	28.1	6.1	7.6
Flexural rigidity (mg-cm)	ASTM D 1388, mod.	452671		1429355		146119	
Torsional stiffness (cm-kg/degree)	COE / GRI GG9	3.43		7.50		3.47	

MD*: machine direction; TD**: cross-machine direction / transverse direction.

Knowing that the test parameters and procedures such as grip type and clamping techniques can significantly affect the stress-strain characteristics, every effort was made

to maintain consistency in testing procedures and conditions (Müller-Rochholz and Recker, 2000; Thornton et al., 2000). Moreover, the biaxial stiffness of geogrids cannot be determined by simply combining the machine direction and cross machine direction stiffness (McGown et al., 2005).

4.2.2 Geogrid Tensile Properties at Small Displacements

While the tensile strength of geogrids listed in Table 6 provides an indication of geogrid tensile characteristics, geogrids used in pavements typically are not expected to experience that much strain, not to mention stretching until failure. In order to characterize the tensile properties of geogrids pertinent to the applications in pavements, it was necessary to conduct wide-width tensile tests for geogrids at small displacements on the basis of ASTM D 6637. The tests were performed in both machine direction (MD) and cross-machine direction (TD).

Grips were made to clamp the two ends of geogrids (Figure 9). Care was exercised to ensure that there was no slipping between the grids and geogrids during the testing. The dimensions of the geogrid specimen were 20 cm × 30 cm to have representative amounts of apertures and grids (Figure 9). The testing was carried out on an Instron machine. A static load at the displacement rate of 0.0208 mm/sec (0.05 in/min) was applied until it reached 500 N, which is close to the load that the geogrids would experience in pavements in the subsequent accelerated testing. The tensile deformation of the geogrid was measured by a laser extensometer with a resolution of 0.001 mm.

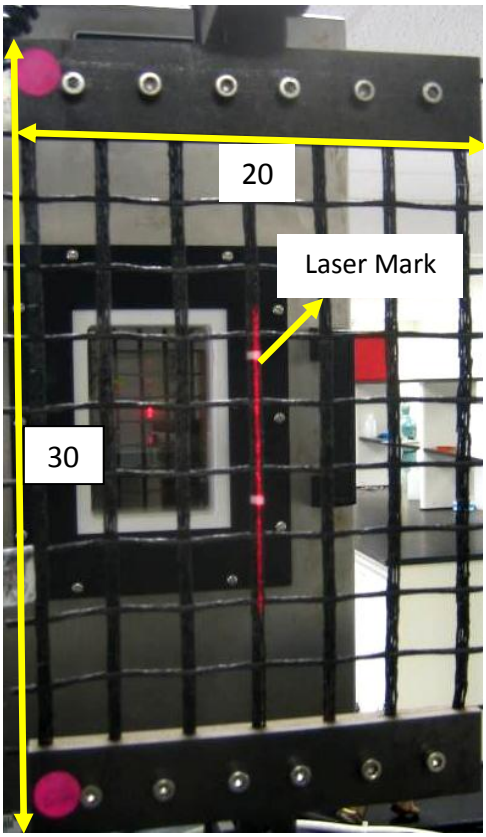

Figure 9. Wide-width tensile tests on geogrids (units in cm)

In accordance with ASTM D 6637, the tensile stress is calculated as follows:

$$\sigma_f = [(F - T)/N_r] \times N_t \quad (18)$$

where:

σ_f = equivalent force per unit width, N/m

F = measured force, N

T = slack tensile load, N

N_r = number of tensile elements (ribs) being tested

N_t = number of tensile elements per unit width, equal to N_c/b

The number of tensile elements per unit width (N_t) of the geogrid is determined by taking the average of three measurements from samples that are 95% of the roll width. The number of tensile elements (ribs), N_c, is counted within the measured distance, b.

The results of the tensile testing for Grids A, B, and C in both the machine direction and cross-machine direction are presented in Figure 10, Figure 11, and Figure 12, respectively. As can be seen, for Grids A and C, the tensile characteristics were considerably different between the machine direction and cross machine direction, while Grid B exhibited similar tensile behaviors in both directions. Table 7 lists the tangent tensile modulus of each geogrid in both machine direction and cross-machine direction. As can be seen, Grid B generally showed higher tensile modulus than Grid A and Grid C. It is worth mentioning that the tensile moduli were tested under the conditions of small strains (less than 1%), which would be the strain level experienced by geogrids installed in the pavement sections during subsequent accelerated testing.

Table 7. Geogrids tensile modulus

Geogrids	**Tensile Modulus (N/m)**	
	Machine Direction	Cross-Machine Direction
Grid A	3052	5231
Grid B	6249	5962
Grid C	4813	3261

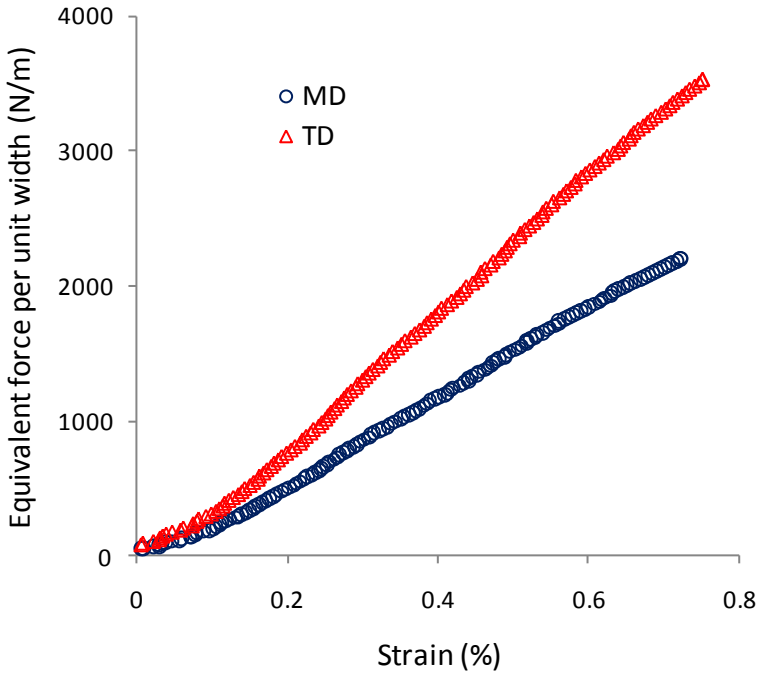

Figure 10. Tensile tests results for Grid A in machine direction (MD) and cross-machine direction (TD)

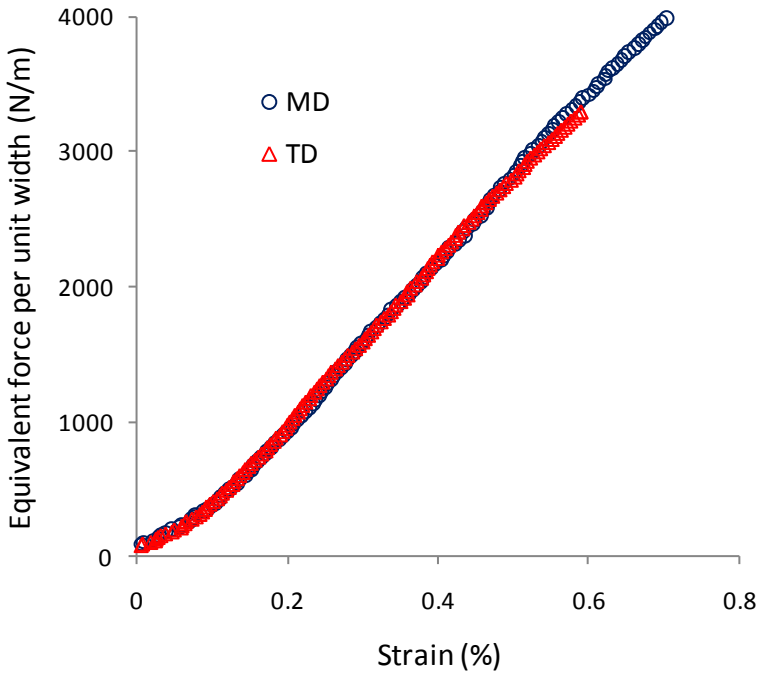

Figure 11. Tensile tests results for Grid B in machine direction (MD) and cross-machine direction (TD)

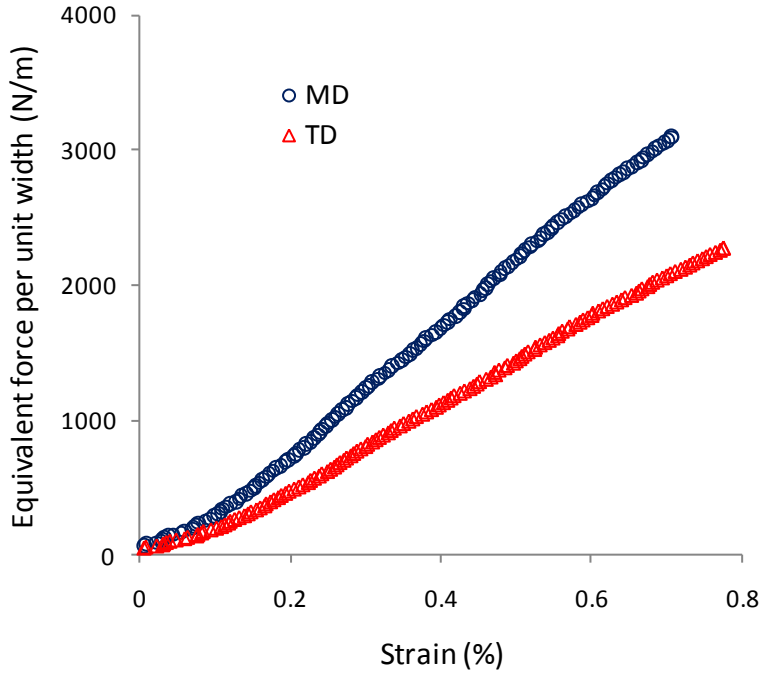

Figure 12. Tensile tests results for Grid C in machine direction (MD) and cross-machine direction (TD)

4.3 Aggregate-Geogrid-Aggregate Interface Characterization

The soil-geogrid-aggregate and aggregate-geogrid-aggregate interfaces were characterized through bench-scale tests including pullout tests (ASTM D6706) and direct shear (ASTM D 3080). The objective of the bench scale tests is to evaluate the performance of the geogrid under the conditions and in the medium in which it will be installed, as opposed to index tests, where the geogrid is tested in isolation. Pullout tests were conducted in this study to characterize the interaction properties of the various types of geogrids installed within aggregates. TRI/Environmental Inc. performed the pullout testing.

It should be pointed out that the interfaces between geogrids and pavement materials were loaded until failure in both the pullout and direct shear tests. While this is not the typical service condition for the application of geogrids in pavements, the results of the pullout and direct tests can be indicative and should be interpreted within the context of pavement applications.

4.3.1 Pullout Test Procedures

Pullout tests were conducted on three geogrids in a medium consisting of the base course aggregates used in the pavement section per ASTM D6706 in the machine direction of the geogrid. The pullout test setup is shown in Figure 13. The geogrid samples were cut into 1.2-m by 0.6-m sections and inserted into a 0.4-m-thick compacted aggregate layer with the machine direction ribs oriented parallel to the pullout direction. All pullout tests were carried out under normal pressure of 6.9 kN/m^2 (144 psf) and at a displacement rate of 1.0 mm/min. The geogrid displacements were measured at the front of the pullout box and at 31 cm, 61 cm, 89 cm, and 116 cm away from the front through a tell-tale system having steel wires connecting geogrids to LVDTs.

The geogrid's resistance to pullout is a function of frictional characteristics between the geogrids and surrounding unbound materials, strength of the geogrid junctions, flexural stiffness of the transverse ribs, and geogrid percent open area. A strong bond between the soil and the geogrid can be achieved with the satisfactory factors above.

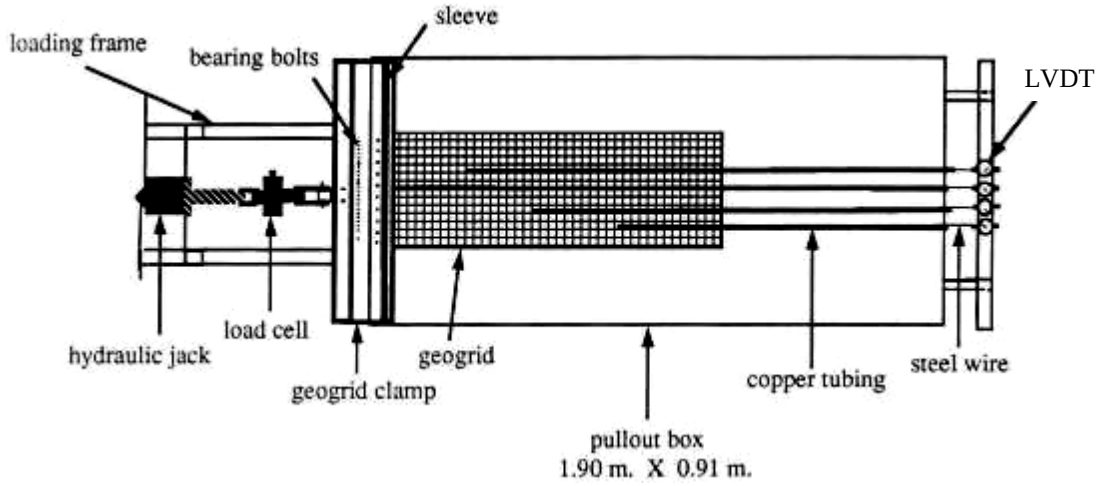

(a)

(b)

(c)

Figure 13. Pullout test setup: (a) plan view schematic of the pullout box (Koerner, 1998); (b) top-view of pullout box showing the geogrids on the soil and tubes housing steel wires (Courtesy of TRI/Environmental Inc.); and (c) connection of steel wire to a geogrid rib (Courtesy of TRI/Environmental Inc.)

4.3.2 Pullout Tests Results

Figure 14 shows the pullout force-displacement relationships for Grids A, B, and C at the front face of the pullout box. Although Grid C's interaction coefficient, derived from the maximum pullout load, is the highest among the three geogrids, Grid B had the best pullout resistance at small displacements (up to 11 mm in this case). Similar trends were observed at the other locations: 61 cm, 89 cm, and 116 cm from the front face. Note that the attributes of geogrids at small strain are important when geogrids are used as pavement reinforcement, since traffic-induced deformation of geogrids in pavements is minimal. From that standpoint, the coefficient of interaction results should be used

cautiously. The magnitude of the necessary pullout force to induce small displacements is more indicative of performance in pavements.

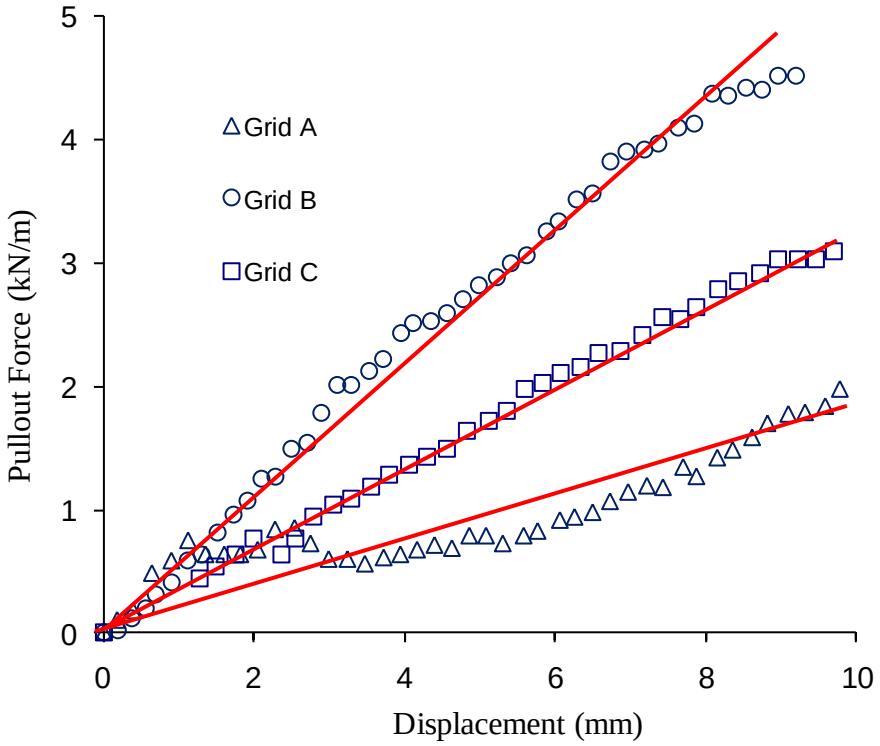

Figure 14. Pullout load-displacement for Geogrids A, B, and C at the front of the pullout box

Figure 15 demonstrates the relationship between pullout force and displacement at different distances from the front of the pullout box for Grid A and Grid B, which represent flexible and stiff geogrids behaviors, respectively. Along the pullout direction, the portion of Grid B furthest from the pulled end (back end of the pullout box) does not show significant movement until the occurrence of pullout failure. In contrast, significant displacement at all the tell-tale locations indicates possible slippage of Grid A at the interface. This again indicates that Grid B has better pullout resistance.

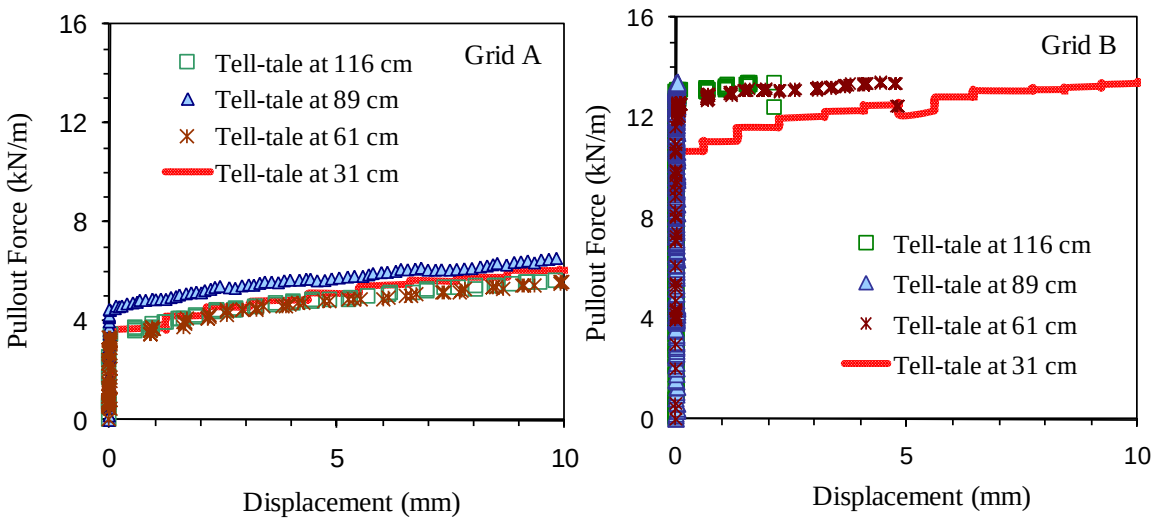

(a) (b)

Figure 15. Relationship between pullout force and displacement: (a) Flexible geogrid Grid A; (b) Stiff geogrid Grid B

4.4 Aggregate-Geogrid-Soil Interface Characterization

Direct shear tests were conducted for characterizing the interfaces among the three geogrids, two soils, and one aggregate. A total of 12 interfaces were tested through direct shear tests, including reinforced and unreinforced interfaces (Table 3).

4.4.1 Direct Shear Test Procedures

The direct shear test was conducted in conformance with ASTM D 3080 to measure the friction angle and adhesion at the interface between the subgrade and aggregate base layer, with and without a geogrid in place. The geogrids were placed between the upper aggregates box and the lower soil box (Figure 16). Dimensions of both boxes were 30.5 cm × 30.5 cm × 10.2 cm (12 in × 12 in × 4 in). The base aggregate was remolded and compacted to 100% of maximum dry density at optimum moisture content (3.9%). In direct shear tests with Soil 1, the subgrade soil was compacted to 92.5% of maximum dry density and at optimum moisture content (10%). In direct shear tests with Soil 2, the soil was compacted at dry unit weight of 1442 kg/m^3 (90 pcf) and at water content of 25%, which were similar conditions to those under which the subgrade was constructed in accelerated testing. Direct shear tests were performed under three different normal pressures: 12 kPa (2 psi), 27 kPa (4 psi), and 36 kPa (6psi). The selected pressure

of 27 kPa was an approximate estimate of the pressure imparted on the pavement subgrade during the accelerated test based on the applied traffic loading. Shear forces were applied at a constant displacement rate of 1.02 mm/min (0.04 in/min), slow enough to dissipate soil pore pressure. TRI/Environmental Inc. performed the direct shear tests with Soil 1 and SGI Testing Services LLC performed all the direct shear tests with Soil 2 and Soil 3.

(a)

(b)

Figure 16. Direct shear tests: (a) a geogrid sample placed on compacted subgrade soil in the lower shear box; (b) subgrade soil in the lower box upon the completion of tests and removal of aggregates (courtesy of SGI Testing Services, LLC)

Shear stress applied to the specimen for each recorded shear force was calculated based on corrected specimen contact area. Correction of specimen contact area was necessary because the actual contact area decreased as a function of horizontal displacement of the traveling container. The corrected area was calculated for each displacement reading by using the following equation:

$$A_c = A_i - d \times W \quad (19)$$

where:

A_c is corrected area, m^2

A_i is initial specimen contact area, m^2

d is horizontal displacement of the traveling container, m

W is specimen contact width in the direction perpendicular to that of shear force application, m

4.4.2 Direct Shear Tests Results

Figure 17 illustrates interface resistance behavior from unreinforced and reinforced soil samples under displacement-controlled direct shear tests. As expected, for each type of interface shear stress, the value for failure generally increases with increasing normal stresses.

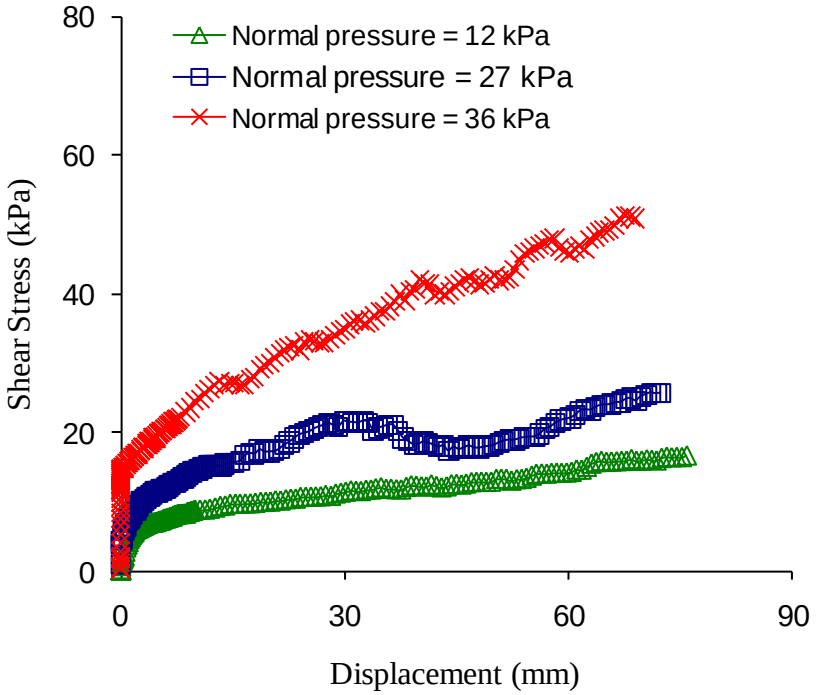

(a)

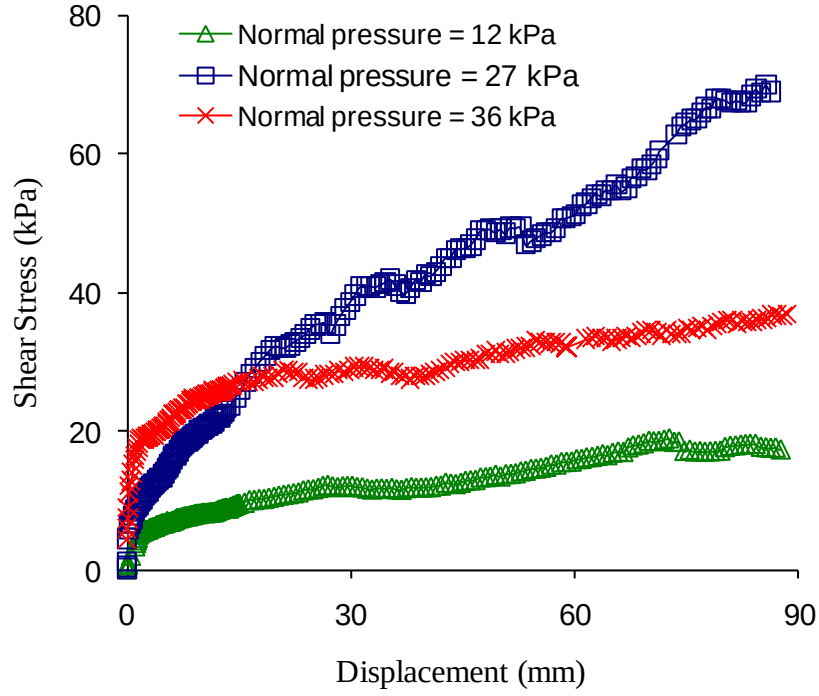

(b)

Figure 17. Direct shear tests under normal pressure of 12 kPa (2 psi), 27 kPa (4 psi), and 36 kPa (6psi): (a) unreinforced Soil 1-aggregate interface; (b) reinforced Soil 1-Grid A-aggregate interface

Area-corrected peak values of shear stress and corresponding normal stress were used to derive angle of friction and effective adhesion. Figure 18 shows the failure envelopes for the unreinforced and reinforced interface.

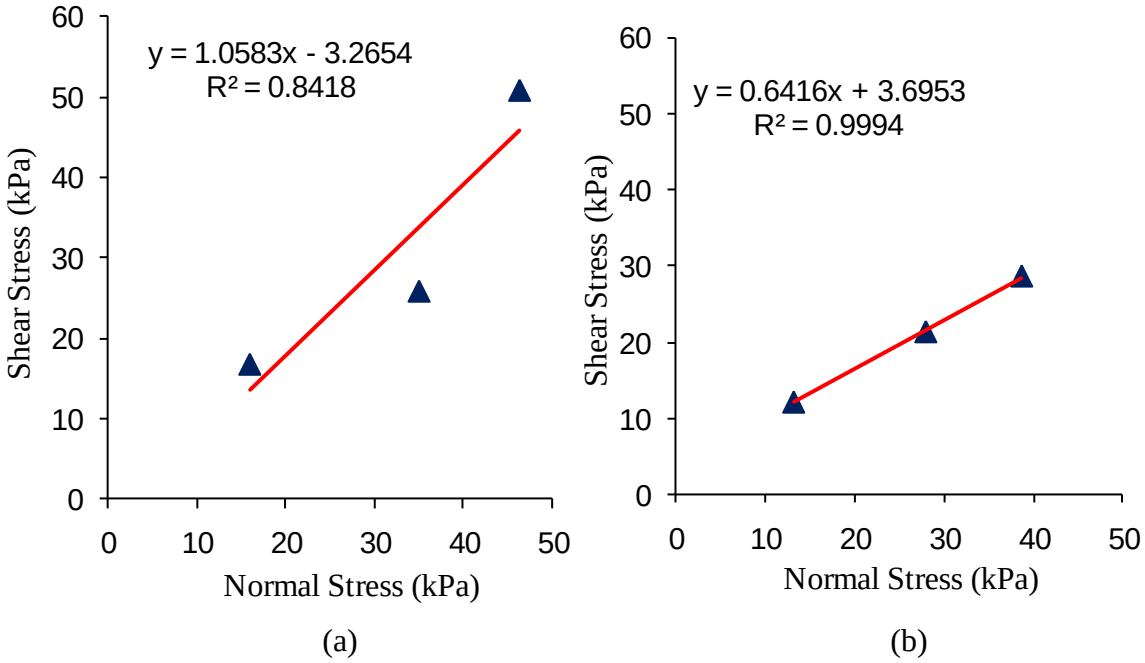

(a) (b)

Figure 18. Failure envelope at peak loading: (a) unreinforced Soil 1-aggregate interface; (b) reinforced Soil 1-Grid A-aggregate interface

Given the shear strength parameters of the control interface, the interface efficiency factor, E_ϕ, can be calculated as (Koerner, 1998):

$$E_\phi = \frac{\tan\delta}{\tan\phi} \qquad (20)$$

where δ is the friction angle of the geogrids reinforcement interface, and ϕ is the friction angle of the control interface. The efficiency factor for geotextiles varies from 0.6 to 1.0, but can be greater than 1.0 for geogrids (Juran et al., 1988).

Table 8 summarizes the strength index interpreted from direct shear tests results. Although the interface characteristics during direct shear tests can be influenced by many factors, such as applied normal pressure, geogrid material characteristics, and drainage conditions. For this study, the geogrid material properties were expected to be the only

factor affecting the interface, since all other factors were held constant among the tests for the four geogrids.

Table 8. Summary of direct shear tests results

Interface	Angle of Friction (deg.)	Adhesion (kPa)
Soil CL-Aggregates	26.0	12.4
Soil CL-Grid A- Aggregates	25.0	11.3
Soil CL-Grid B- Aggregates	25.0	12.0
Soil CL-Grid C- Aggregates	25.0	11.7
Soil ML-Aggregates	26.0	12.0
Soil ML-Grid A- Aggregates	25.0	11.0
Soil ML-Grid B- Aggregates	25.0	10.8
Soil ML-Grid C- Aggregates	26.0	11.3

5 INSTRUMENTED ACCELERATED PAVEMENT TESTING

In order to investigate the pavement critical responses and obtain more sophisticated measurements, two sets of accelerated pavements testing using various instruments were carried out for pavement slabs constructed in a concrete pit measuring 2.1 m × 3.7 m. The pavement section layouts and thicknesses were the same for these two sets of instrumented accelerated testing, except the subgrade soil types were different. In each of the two instrumented accelerated tests, there were four pavement sections among which one was a control and others were reinforced by Grid A, Grid B, and Grid C, respectively. The two instrumented accelerated tests were designated as Instrumented APT I and Instrumented APT II, respectively.

Accelerated testing on instrumented pavement sections served two purposes: providing measurements of critical pavement responses for the calibration and verification of FE models; and investigating the performance of different geogrids and providing measurements for the development of permanent deformation models. Testing results from Instrumented APT II were used to verify the permanent deformation models developed on the basis of results from Instrumented APT I. Lightweight deflectometer (LWD) testing was conducted on pavement sections to backcalculate the pavement layer properties. Both static and dynamic measurements from the instruments were taken at the intervals of the MMLS3 load applications in addition to the surface profile measurements.

5.1 Pavement Dimensions and Boundary Effects

The available pit space was 366 cm (144 in) long, 206 cm (81 in) wide, and 127 cm (50 in) deep to the backfill surface. The structural thickness of pavement layers had to be scaled down according to the scale of MMLS3 load and existing PennDOT design specifications for low-volume roads. Furthermore, numerical studies were carried out to investigate the potential boundary effects on the pavement with the four-section layout in the existing concrete pit.

5.1.1 Determination of Scaled Pavement Layer Thickness

The current PennDOT pavement design methodology is based on the AASHTO *Guide for Design of Pavement Structures* (AASHTO, 1993), which is accompanied by the AASHTOWare Darwin (PennDOT, 1995). Table 9.4 (Min. and Max. Thickness of Surface, Base, and Subbase Materials for Superpave Mixes) in Publication 242 was used to determine the structural thicknesses. The minimum value for collector highways specified in Publication 242 was adopted for each pavement layer to represent a low-volume road structure with weak bed soil support, which generates a full-scale pavement structure consisting of 9 cm (3.5 inches) AC layer, 13 cm (5 inches) aggregate base course, and 15 cm (6 inches) subbase. By combining the base and subbase layers, a one-third scale model pavement has 4 cm (1.5 inches) AC layer and 10 cm (4 inches) base layer, as Figure 19-a shows. Note that 4 cm (1.5 inches) of AC layer is also the recommended minimum lift thickness for the 9.5-mm asphalt mixtures that were used for constructing the AC layer (PennDOT, 1995).

5.1.2 Boundary Effects

Studies were carried out to investigate possible boundary effects due to both the backfill aggregates foundation and concrete walls. The investigation was focused on the impact of various boundaries on a critical pavement response, vertical stresses at the top of subgrade. Results of a previous study on the boundary effects due to subgrade thickness for an unpaved aggregate-subgrade structure showed that the 113-cm-thick subgrade (Figure 19-a) was adequate for achieving minimal impact from the backfill foundation underneath the subgrade. Linear static two-dimensional axisymmetric FE models with different radial distances between the load center and boundary were created to study the effects of concrete walls on the pavement responses. It was shown that the 46 cm (18 in) boundary distance (Figure 19-b) with the four-section layout had insignificant effects on the change of vertical stresses at the top of the subgrade.

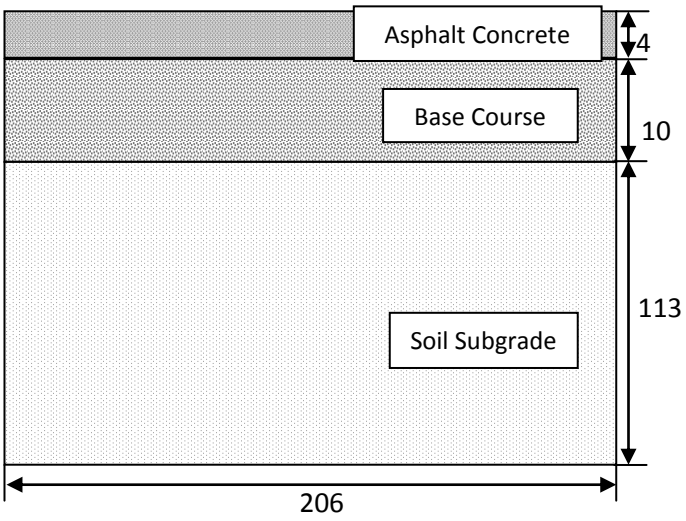

(a)

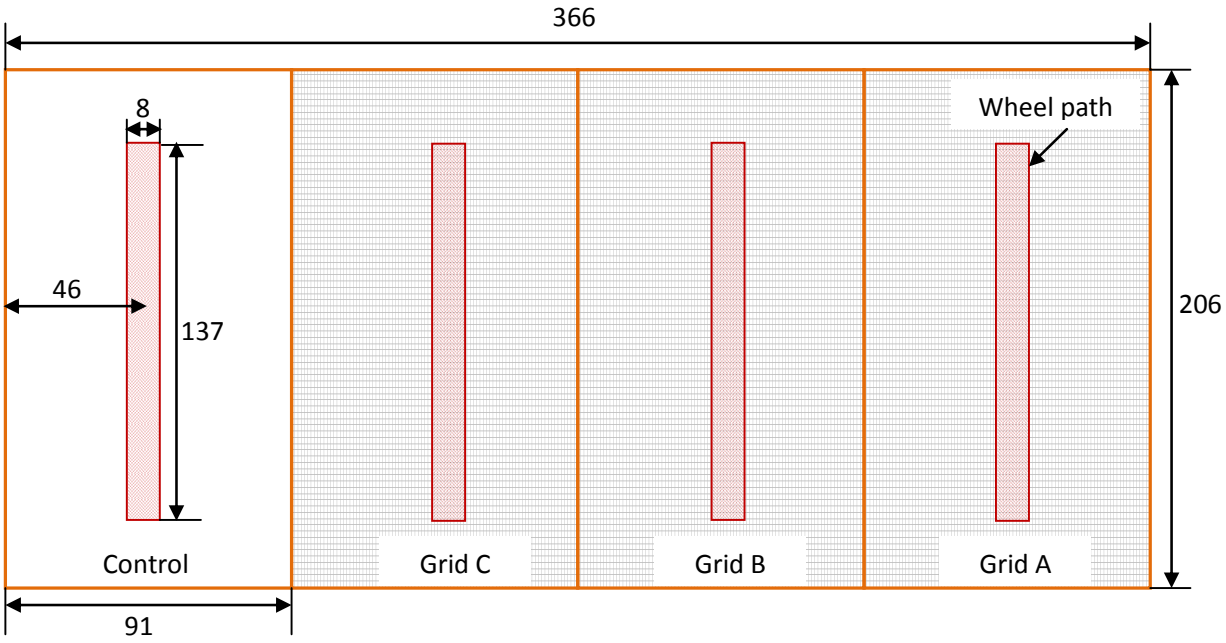

(b)

Figure 19. Dimensions of the model pavement sections: (a) cross section of the pavement sections; (b) layout of the pavement sections (units in cm)

Boundary Effects due to Backfill Foundation

The soil subgrade had a thickness of 113 cm (44.5 in), as shown in Figure 19-a. A previous study was conducted on an unpaved aggregate-subgrade structure to investigate the effects of subgrade thickness on the pavement critical responses. A three-layer system was considered: 13-cm (5-in) aggregates base with modulus of 290 MPa (42,061 psi),

soil subgrade with modulus of 30 MPa (4,351 psi), and an assumed infinite layer as for the backfill foundation with modulus of 150 MPa (21,756 psi). Only the MMLS3 load was examined. The LWD loading was not examined because it showed less effect on vertical stress atop subgrade. The MMLS3 load was assumed to be a circular, uniformly distributed load with pressure of 689 kPa (100 psi) and contact radius of 3.5 cm (1.39 in). Calculation using the linear elastic program KENLAYER was conducted for a series of soil subgrade thickness.

Figure 20 shows that the change in vertical stress atop the subgrade becomes minimal when the subgrade thickness is about 100 cm (40 inches). One could assume that the 113 cm (44.5 inches) thick subgrade for the proposed pavement cross section with the addition of an asphalt layer has negligible boundary effects due to the backfill underlying the subgrade.

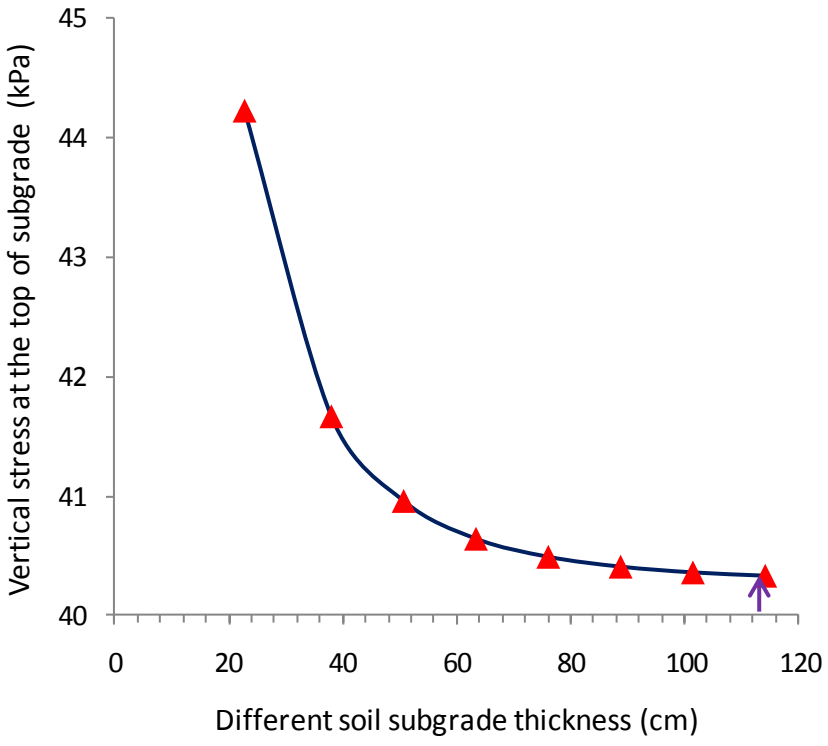

Figure 20. Change of vertical stress on top of subgrade with subgrade thickness

Boundary Effects due to Concrete Side Walls

A series of FE modeling was performed in order to find out the distance from the load center to nearest boundary, such that the boundary effect is negligible. The FE models simulated the MMLS3 loading and the proposed structural layer thickness, as Figure 19 shows. Modulus values for base course and the backfill layer (AASHTO #57 aggregates) were obtained through the inverse analysis procedure from previous tests.

Table 9. Inputs for FE models

Layer	**Thickness (cm/in)**	**Modulus (MPa/psi)**	**Poisson's Ratio**	**Load**
AC	4/1.5	2758/400000	0.2	Pressure: 689 kPa (100 psi) Contact radius: 3.5 cm (1.39 in)
Base Course	10/4	290/42061	0.3	
Subgrade	113/44.5	30/4351	0.4	
AASHTO #57	127/50	150/21756	0.3	

In the FE models, the distance from the loading center to the nearest boundary varied from 25 cm (10 inches) to 102 cm (40 inches) to observe the boundary effects on vertical stress on top of the subgrade. As can be seen in Figure 21, the change of vertical stress on top of the subgrade becomes minimal when the distance from the load center to the boundary reaches 51 cm (20 inches). It is noticed that the boundary distance is 46 cm (18 inches) for the four-section layout as shown in Figure 19-b, which is 5 cm less than the ideal boundary distance. However, the vertical stresses on top of subgrade for sections with boundary distance of 51 cm (20 inch) and 46 cm (18 inches) are 15.7 kPa (2.27 psi) and 15.4 kPa (2.24 psi), respectively. The percentage difference in vertical stress atop subgrade between the two cases is about 1.9%. It is, therefore, expected that the boundary effects due to the side walls with distance of 46 cm to the load center is negligible.

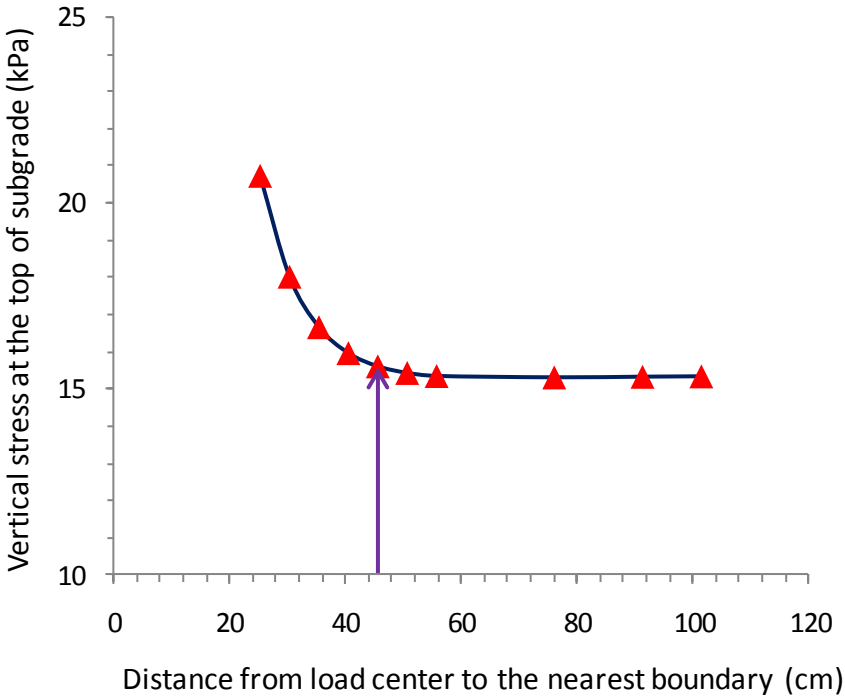

Figure 21. Vertical stress atop subgrade with different boundary distance

5.2 Instruments Selection and Calibration

In order to accurately quantify the reinforcement effectiveness for different geogrids and identify the optimal properties for given subgrade conditions, it is necessary to measure the stresses and strains prevalent at the aggregate-geogrid-soil interface in addition to the nature and value of the strain felt by the geogrid ribs. Using instrumentation for making such measurements also allows for understanding and characterization of the mechanisms taking place at the base-geogrid-subgrade interface. Furthermore, for the purposes of calibrating the response model (FE model) and permanent deformation models, it was set to measure these pavement critical responses: elastic and permanent deformation at the top of the subgrade, vertical stresses at the top of the subgrade and strains in the geogrids.

5.2.1 Instruments for Subgrade Deformation Measurement

Both elastic deflection and permanent deformation at the subgrade needed to be measured in order to verify the FE models and calibrate the permanent deformation models. An in-depth search was conducted to identify a reliable approach to measure the

deformation in pavement layers. More details on selecting an instrument to measure subgrade deformation can be found in Appendix A. It was decided that LVDTs (Macro Sensors GHSE-750-1000) would be used to measure the deflection of subgrade surface. The end of the LVDT was fixed with respect to the bottom of the subgrade. Thus, the LVDT measured the total deformation of the subgrade.

Considering the fact that the measurements of subgrade deformation are important for the calibration of the FE models and deformation prediction models, in order to ensure subgrade deformation measurements, a backup instrumentation plan was made for the subgrade deformation measurements. The relatively inexpensive potentiometers were customized and installed at the top of the subgrade to measure the elastic and permanent strains within the gauge length. Specifications for LVDTs and potentiometers can be found in Appendix A.

Using a micrometer, calibration was carried out for each LVDT and potentiometer before the LVDTs and potentiometers were installed in the pavement. The LVDTs and potentiometers were recalibrated after their use in the Instrumented APT I and before their use in Instrumented APT II. The calibration procedures and results are provided in Appendix A.

5.2.2 Instruments for Subgrade Vertical Stresses Measurement

The selection of sensors for measuring subgrade vertical stresses in pavements was based on the known loading configuration and pavement structures to ensure sufficient resolution and accuracy. A desirable pressure sensor should be able to measure stresses in the soil without significant disturbance to the existing state of stress. There are two basic types of earth pressure cells for measuring the total vertical stress in the subgrade soil: diaphragm cells and hydraulic pressure cells.

The primary component of a diaphragm cell is a stiff circular membrane supported by a stiff edge ring. The membrane is deflected by the external soil pressure. The deflection of the membrane is measured by an electrical resistance strain gage transducer attached on the inner face of the cell. The membrane deflection is related to the magnitude of external soil pressure. On the other hand, the hydraulic cell consists of two circular steel plates. The two circular steel plates were welded together around their

periphery to form a cavity filled with de-aired liquid. The cavity is connected by a steel tube to a pressure transducer that converts the fluid pressure to an electrical signal. Vibrating wire transducers and semiconductor-type transducers are typically used for hydraulic pressure cells. While vibrating wire transducers generally measure long-term static pressure, the semiconductor transducer was chosen to measure the dynamic pressures from the traffic loads.

Hydraulic-type earth pressure cells (Geokon 3500) with semiconductor transducer were chosen to measure the vertical stress as one of the critical responses of pavement. In order to diminish the disturbance to the pavement system, the earth pressure cells were customized into smaller dimensions to accommodate the application in the scaled accelerated testing.

It is ideal to conduct the calibration for pressure cells in a hydrostatic stress state. In this study, the pressure cells were subjected to known increasing dead weights to check the linearity of the pressure cell measurements. More information on the specifications of the pressure cell and their calibration are included in Appendix A.

5.2.3 Geogrid Strain Gages

Measuring strains developed in geogrids during the MMLS3 wheel load applications can quantify the degree to which the geogrids are mobilized and engaged. In this study, the strain gage selection was mainly based on the available application areas for the gage and the expectation of possible strains in the geogrids during the testing, although other factors should be considered such as the test duration, accuracy required, and cyclic endurance (Vishay, 2007).

After an in-depth literature search and consulting application engineers from strain gage distributors, it was decided to use a foil type strain gage (KFG-5-120-C1-11L3M3R) from Omega Engineering, Inc. to measure strains in geogrids. The strain gage has a backing material constructed from polyimide, and the measurement grid is made of a constantan alloy that can sustain strains up to 5%. The strain gage has a resistance of 120.0±0.8 Ω, gage factor of 2.09±1.0%. The overall length and width of the strain gage is 9.4 mm and 2.8 mm, respectively. Strain gages were connected into a three-wire quarter bridge circuit with the completion module of the data acquisition system. Shunt

calibration was conducted for the strain gage circuits through a precise 100-kΩ resistor built into the module for the purpose of verification and scaling. Strain gages were installed on both the top and bottom surface of the geogrid rib in order to account for the bending effects.

Strain gages are conventionally calibrated by the manufacturer on a steel specimen to obtain a gage factor. Strain gages do not affect the behavior of the calibration steel specimen because of the comparable modulus ratio between the strain gage and steel. However, it is recognized that the gage-adhesive system adds reinforcement effects to geogrids due to the significantly lower modulus of geogrids compared to that of the gage-adhesive system. Furthermore, the strain gages had to be coated for protection from mechanical damage and waterproofing. The external coat-gage-adhesive system could introduce considerable reinforcements to the locus where the strain gage is installed. A calibration was conducted to correlate the local strain measurements from strain gages to the global strains measured by a laser extensometer. The calibration procedures and results are attached in Appendix A.

5.3 Pavement Slabs Construction and Instrument Installation

The pavement slabs were constructed in the pit according to the configuration and dimensions discussed in Section 6.1. Similar construction procedures as in the previous exploratory accelerated testing were adopted. Throughout the construction, care was exercised to ensure the uniformity of compaction efforts among the four sections. Various instruments were installed in the pavement slabs using different techniques and following different procedures. The successful installation of the instruments ensured the subsequent reliable measurements.

5.3.1 Construction of Pavement Slabs

The pavement slabs construction started with preparing the subgrade soil at the target moisture content in order to have a desired CBR value for the subgrade. Soil 1 (CL / A-4(5)) was used for constructing the subgrade in Instrumented APT I. The subgrade was constructed by several 6-in lifts in order to achieve adequate compaction. A vibratory plate compactor was used to compact the soil. Sand cone tests were performed for each lift after compaction to check the degree of compaction and moisture content. Presented

in Table 10 are the results of sand cone testing for the last three lifts, representing the as-constructed subgrade conditions.

Table 10. As-constructed lift properties of subgrade soil in Instrumented APT I

Lift (from bottom to top)	**Density (kg/m^3 / pcf)**	**Moisture Content (%)**	**Degree of Compaction (%)**
Lift One	1858.0 / 116.0	23.6	89.8
Lift Two	1720.8 / 107.4	26.4	81.3
Lift Three	1799.1 / 112.3	25.4	85.7

Following the completion of subgrade construction, geogrids were placed on top of the subgrade with care to avoid any wrinkles. Aggregate was then placed into the pit at the optimum water content and compacted by two lifts. Due to the limited capacity of the heating oven for asphalt mixtures, the asphalt layer had to be constructed by dividing the entire pit into two halves in the direction of length (366 cm). Air voids of the asphalt concrete for each section were measured after completion of the construction.

5.3.2 Installation of Instruments

A total of five different types of instruments were installed in the pavement system: LVDTs, earth pressure cells, potentiometers, strain gages, and thermocouples. All the load-associated instruments were installed at the base-subgrade interface and underneath the wheel path, as Figure 22 shows. For each of the four sections, one LVDT was installed at the top of the subgrade and in the middle of the section. As can be seen in Figure 22-a, the LVDT was housed in a steel tube fixed to the bottom of the subgrade. The pressure cell and potentiometer were installed at the subgrade top with 25 cm offset from the middle of the section in the direction of the MMLS3 wheel path. For each of the three reinforced sections, a total of eight strain gages were installed on the geogrid. Strain gages were installed at the locations with 10 cm offset from the middle of the section. At each location, two pairs of strain gages were attached onto two adjacent geogrid ribs in the direction of machine direction (MD) and cross-machine direction (TD), respectively. The challenge of instrumenting the geogrids has been documented by many (Brandon et al., 1996; Maxwell et al., 2005; Warren et al., 2005).

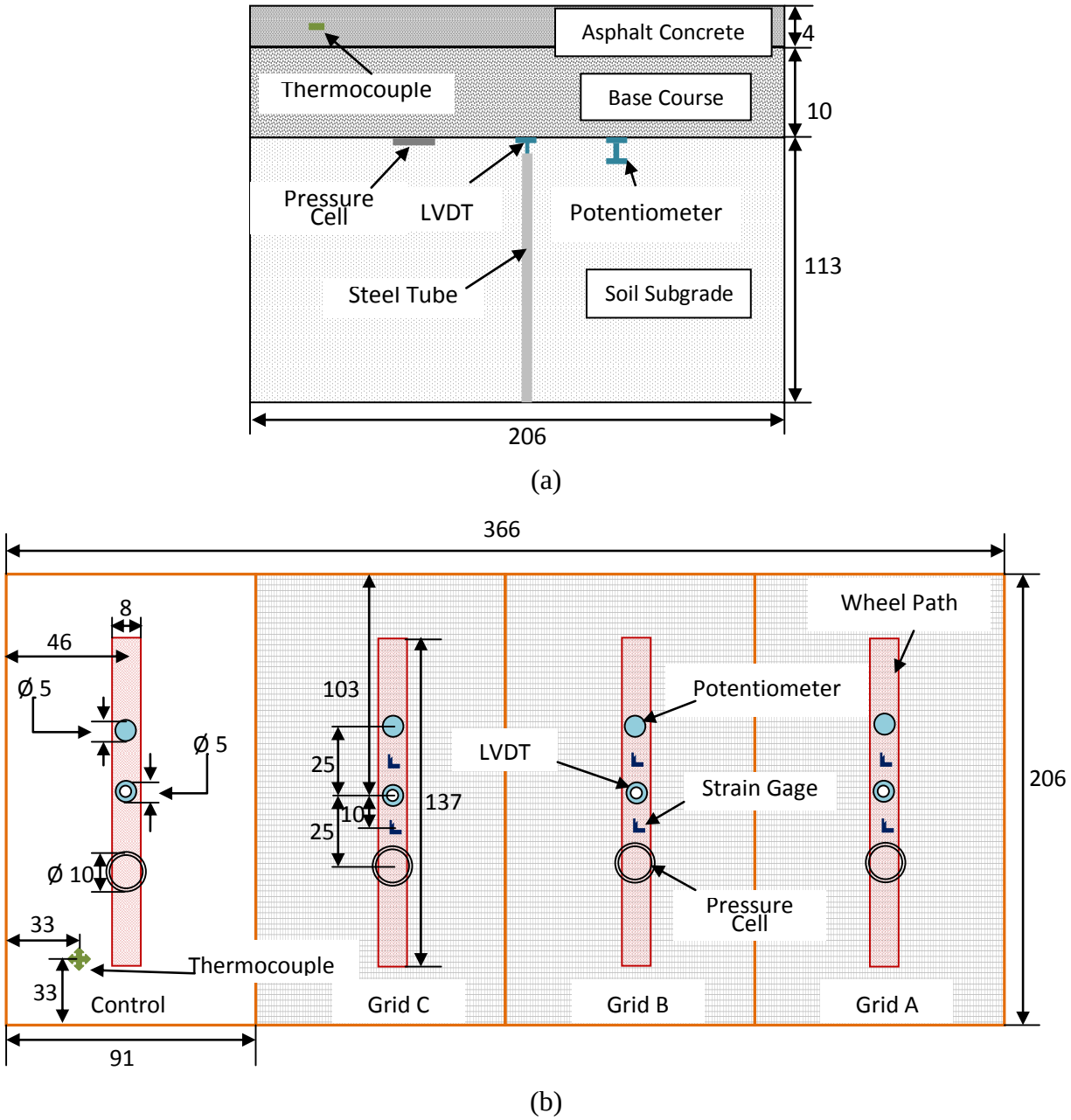

Figure 22. Positions of instruments in the pavement system: (a) cross section view of the instrument locations; (b) plan view of the instrument locations (units in cm)

Installation of each of the five types of instruments followed different procedures. Modifications to the instrument were made to accommodate the applications of the instruments in this study. Techniques were developed to protect the instruments from mechanical damage and water infiltration. More details about instrumentation installation can be found in Appendix A.

5.4 Testing and Data Collection

Using a non-destructive device, lightweight deflectometer tests on the pavement layers' structural capacities were conducted on aggregate surfaces and asphalt surfaces for each of the four sections. During the LWD tests, surface deflections under a known impulse load were recorded along with the instrument responses.

After the LWD tests on the asphalt surface, the pavement was subjected to the MMLS3 trafficking. Both static and dynamic measurements from the instruments were collected at intervals of MMLS3 axles while the pavement surface profiles were also measured.

It should be pointed out that data collection from the instruments was carried out at various stages of the construction and testing. In-air readings from the instruments were taken just before the instruments were placed into the pavement. During the construction, particularly the compaction process, instruments data were collected to monitor the impact of construction onto the sensors. Upon the completion of construction and before any testing, a baseline reading was taken for all of the instruments.

5.4.1 Lightweight Deflectometer Testing

A portable lightweight deflectometer (Carl Bro^{TM} PRIMA 100) was used for assessment of in-situ pavement layer modulus. A description of the device can be found in Appendix B.

The main purpose of the LWD tests was to measure the pavement responses to a known load and use the measurements to calculate the pavement layer properties through an inverse analysis procedure. The LWD was not able to yield meaningful measurements on testing the soil subgrade because the subgrade was too weak to experience an elastic deflection under the LWD load. LWD tests were conducted on aggregates base for each of the four sections. For the three reinforced sections, five locations were tested along the line where the MMLS3's wheel load was to be applied. Only three locations were tested for the control section. Tests were repeated at least three times for each testing point to ensure the consistency of the measurements. The instruments responses to each LWD loading were recorded. Following the same procedure, LWD tests were also conducted on the asphalt concrete layer.

5.4.2 MMLS3 Testing

The MMLS3 testing commenced 24 hours after the completion of the asphalt layer. A total of 100,000 MMLS3 axles were applied to each of the four sections. The pavement responses to the dynamic loading of MMLS3 were recorded through the instruments. Furthermore, in order to monitor the accumulation of the permanent deformation of the subgrade, measurements from the instruments were taken without the MMLS3 surcharge load at various stages of MMLS3 trafficking. In addition to the instruments data, the pavement surface profiles were measured at the intervals of the MMLS3 traffic. For each of the four sections, profile measurements were taken at six different locations along the wheel path.

5.5 Results and Discussion

This section presents the results of LWD testing and the MMLS3 accelerated testing on the four pavement sections from both Instrumented APT I and Instrumented APT II. The measurements from the LWD tests, mainly central surface deflections, can be used as an indicator of the pavement structural capacity, although the LWD test measurements will be used to backcalculate the pavement layer moduli in Chapter 7. Instrumentation measurements as the responses of the pavement system to the MMLS3 load are presented, including subgrade deformation, vertical stresses on top of the subgrade, and strains in the geogrids. In addition, the surface profiles (permanent deformation at intervals of MMLS3 axles) are presented. Factors affecting pavement performance such as variation in compaction efforts, temperature, and moisture content change are discussed.

5.5.1 Surface Central Deflections under LWD Load

LWD testing was conducted on both the aggregate base and asphalt concrete surfaces for each of the four sections. LWD testing was not carried out on the subgrade because the subgrade was too soft to sustain the LWD without permanent deformation. The primary purpose of LWD tests was to provide measurements under a known impulse load for backcalculating the pavement layer properties. However, the peak surface deflection can be used as an indicator of pavement structural capacity. All the central

peak deflection values were normalized to the same loading level of 4.8 kN for the purpose of comparison.

LWD on Base Course Layer

Table **11** presents the peak value of deflection measurements on the base course layer for sections in Instrumented APT I. As can be seen in

Table **11**, the control section generally exhibits higher deflection compared to other reinforced sections in Instrumented APT I. The rank among the sections based on the average peak deflection of all the locations is: Grid A (1641.3 μm), Grid B (1771.2 μm), Grid C (2151.0 μm), and Control (2190.0 μm).

Table 11. Peak deflection (μm) at the center of LWD load on base layer for Instrumented ***APT I*** (normalized to 4.8 kN; 3 days after subgrade construction)

Locations	Press. Cell	Gage_NC	LVDT	Gage_FC	Poten. Meter	*Average*
Grid A	1649.4	1445.1	1398.9	1829.3	1884.0	*1641.3*
Grid B	1968.9	1601.3	1460.9	1774.3	2050.9	*1771.2*
Grid C	1960.4	1800.3	2017.1	2138.0	2839.1	*2151.0*
Control	2015.5	N/A	2075.1	N/A	2479.2	*2190.0*

Table 12 through Table 14 present the central peak deflection measured from LWD tests on the base layer in Instrumented APT II. As previously described, a weaker soil subgrade was constructed in Instrumented APT II. Pavement sections in Instrumented APT II generally showed higher deflection than that in Instrument APT I, as expected (see Table 11 and Table 12).

Table 12. Peak deflection (μm) at the center of LWD load on base layer for Instrumented ***APT II*** (normalized to 4.8 kN; 4 days after subgrade construction)

Locations	Press. Cell	Gage_NC	LVDT	Gage_FC	Poten. Meter	*Average*
Grid A	2682.9	2533.8	2342.9	2368.9	3145.3	*2614.8*
Grid B	3896.1	2870.2	3199.5	3289.0	4271.2	*3505.2*
Grid C	3377.3	2513.6	1810.1	2205.9	2969.6	*2575.3*
Control	4488.8	3704.9	2925.8	2870.2	3415.8	*3481.1*

Due to the delay of asphalt mixture acquisition, the asphalt concrete layer was not constructed until about 1 month after the subgrade construction. It was anticipated that the subgrade might lose moisture and gain stiffness during the time period between the

completion of base construction and the commencement of asphalt layer construction. LWD tests were conducted at the 14th day and 27th day of the completion of subgrade construction. As can be seen from Table 13 and Table 14, the central peak deflection decreases with time, which indicates an increase of pavement layer stiffness caused by the moisture loss.

Table 13. Peak deflection (μm) at the center of LWD load on base layer for Instrumented ***APT II*** (normalized to 4.8 kN; 14 days after subgrade construction)

Locations	Press. Cell	Gage_NC	LVDT	Gage_FC	Poten. Meter	*Average*
Grid A	1657.7	1715.4	1585.8	1732.4	2025.5	*1743.3*
Grid B	2735.4	2005.7	1287.0	1615.4	2799.3	*2088.6*
Grid C	2560.9	1992.1	1499.7	1706.4	2292.5	*2010.3*
Control	2984.5	2287.6	1758.7	1794.0	2376.9	*2240.4*

Table 14. Peak deflection (μm) at the center of LWD load on base layer for Instrumented ***APT II*** (normalized to 4.8 kN; 27 days after subgrade construction)

Locations	Press. Cell	Gage_NC	LVDT	Gage_FC	Poten. Meter	*Average*
Grid A	1305.9	1360.1	1263.2	1309.4	1606.3	*1369.0*
Grid B	1904.3	1484.0	1287.0	1615.4	2303.6	*1718.9*
Grid C	2107.4	1557.9	1281.0	1370.3	2066.9	*1676.6*
Control	2203.7	1544.3	1259.4	1221.6	1540.2	*1553.8*

LWD on Asphalt Concrete Layer

Table 15 and Table 16 present the peak value of deflection measurements on the asphalt layer for sections in Instrumented APT I and APT II, respectively. The deflection measurements were normalized to the same LWD loading level with the measurements on the base course layer. It can be seen the peak central deflection decreased significantly compared to those on the base course due to the addition of the asphalt layer and the resulted increase in structural capacity of the pavement.

Table 15. Peak deflection (μm) at the center of LWD load on asphalt layer for Instrumented ***APT I*** (normalized to 4.8 kN)

Locations	Press. Cell	Gage_NC	LVDT	Gage_FC	Poten. Meter	*Average*
Grid A	434.0	512.3	537.0	402.4	414.2	*460.0*
Grid B	364.4	332.8	358.0	459.5	388.6	*380.7*
Grid C	424.0	456.8	530.8	478.7	497.5	*477.5*

Control	378.7	N/A	425.2	N/A	405.9	*403.3*

Table 16. Peak deflection (μm) at the center of LWD load on asphalt layer for Instrumented ***APT II*** (normalized to 4.8 kN)

Locations	Press. Cell	Gage_NC	LVDT	Gage_FC	Poten. Meter	*Average*
Grid A	562.3	564.6	563.4	525.4	615.2	*566.2*
Grid B	332.8	364.4	358.0	460.0	704.1	*443.8*
Grid C	653.3	650.7	568.0	628.9	688.1	*637.8*
Control	494.4	487.6	534.7	498.5	599.3	*522.9*

5.5.2 Surface Rutting under MMLS3 Trafficking

Figure 23 displays the typical profiles recorded at various numbers of the MMLS3 load repetitions. It can be seen that the change of profiles is more aggressive at the initial stage of the MMLS3 loading due to the densification of the pavement materials under the MMLS3 load.

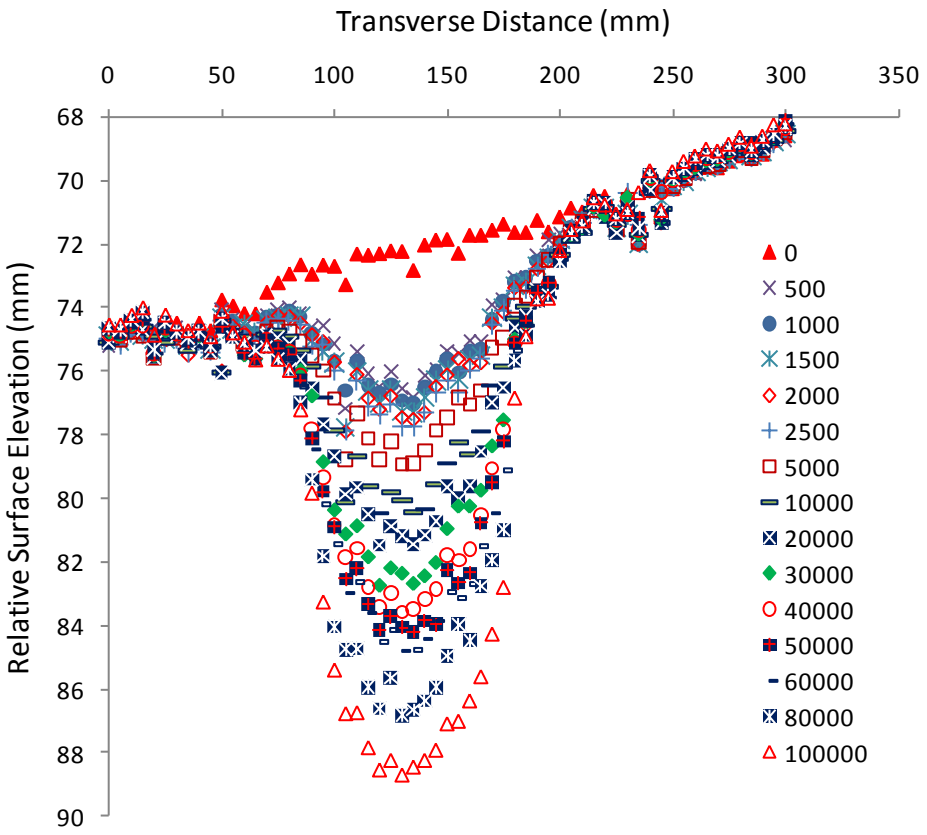

Figure 23. Transverse profile of the wheel path along at different number of MMLS3 load repetition

The accumulation of surface rutting was calculated by subtracting the baseline measurement from the subsequent maximum values of profile measurements. Figure 24 shows the accumulation of surface rutting along with the MMLS3 load applications for the four sections. The surface rutting for each section shown in Figure 24 is the average of the measurements taken at the six different locations within each section.

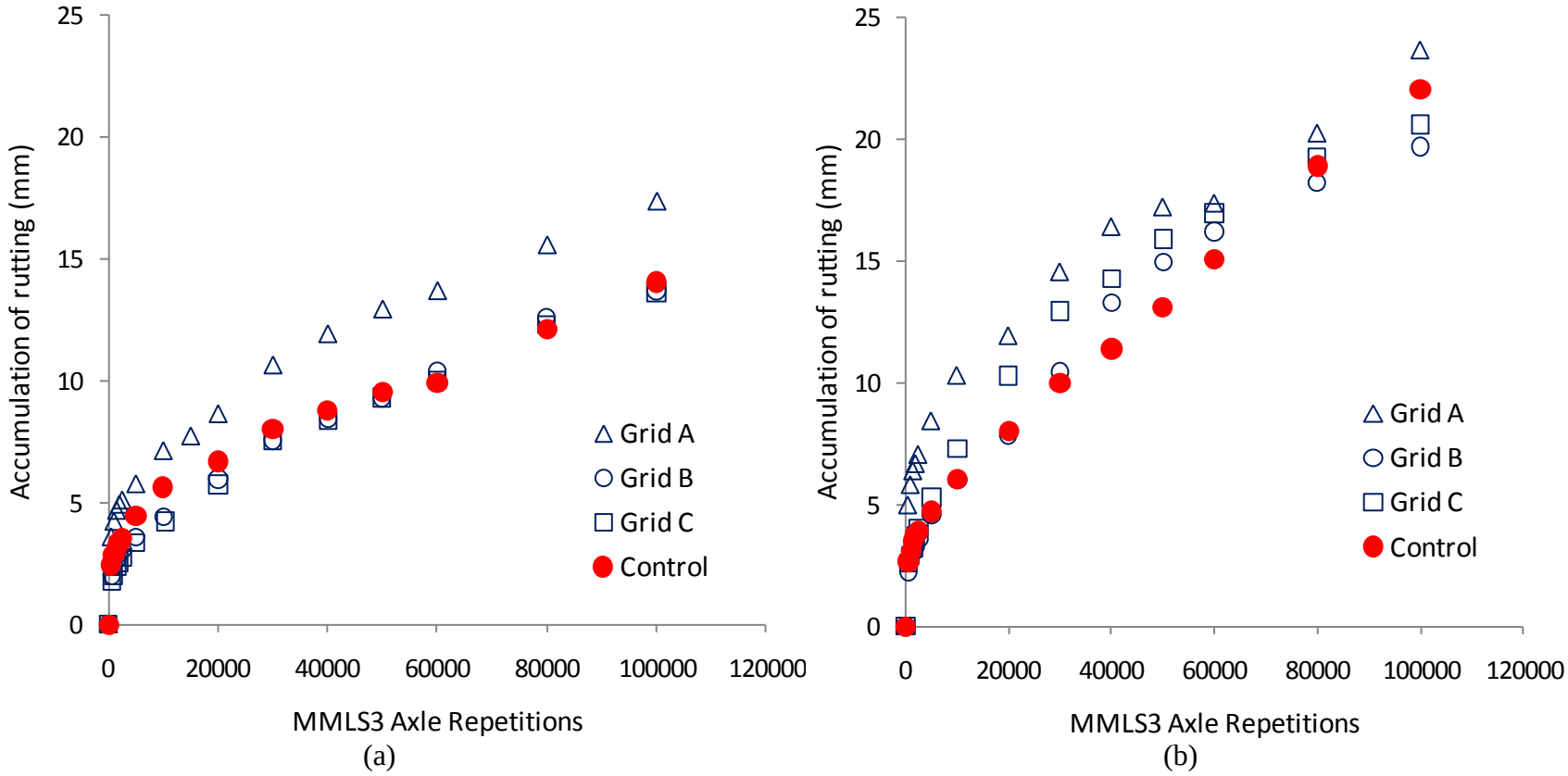

Figure 24. Average accumulation of surface rutting along with the MMLS3 load applications: (a) Instrumented APT I; (b) Instrumented APT II

It is noted that the section reinforced by Grid A showed the most significant rutting among the four sections in both Instrumented APT I and APT II. Sections reinforced with Grid B and Grid C exhibited similar performance through both sets of APT tests. The control section did not necessarily experience the most rutting in both APT tests.

It should be pointed out that there are various factors causing the difference in the performance of resisting surface rutting among the four sections. The pavement structural layers thicknesses and materials used for the four sections were the same. Except for the geogrid reinforcements included at the base-subgrade interface, the most possible factors that may contribute to the difference in the performance of resisting rutting are:

- Change of the moisture content of the subgrade soil
- Asphalt concrete temperatures throughout the testing
- Air voids of asphalt concrete due to the variability in compaction

The factors should be taken into account when comparing the performance among the four sections.

Change of the Subgrade Soil Moisture Content

The stiffness of the soil subgrade is a function of moisture content, as illustrated in Figure 8. Moisture content of the subgrade soil and its distribution changes through the means of both upwards evaporation and downwards seepage. The moisture content of the subgrade soil was 25.4% upon the construction of the subgrade (April 20, 2010). Tests on the moisture content of subgrade soil were carried out after 62 days of the subgrade construction (June 20, 2010). Table 17 lists the moisture content test results after the Instrumented APT I test.

Table 17. The distribution of moisture content in the subgrade after the accelerated testing in Instrumented APT I

Sampling depth from the Subgrade Surface (cm / in)	**Moisture Content (%)**
0.0 - 7.6 / 0.0-3.0	21.2
7.6 - 15.2 / 3.0-6.0	22.0
15.2 - 22.9 / 6.0-9.0	22.9
Average	22.0

It was found that there was about 3.1% and 4.1% decrease in moisture content in the subgrade soil for Instrumented APT I and APT II as listed in Table 18. The decrease in moisture content of the subgrade soil may result in an increase of subgrade stiffness and subsequent decrease in the pavement permanent deformation.

Table 18. Moisture content of subgrade soil in Instrumented APT I and APT II

	APT I Moisture Content (%)	**APT I Moisture Content (%)**
As-constructed	25.1	28.8
After Accelerated Testing	22.0	24.7
Change	3.1	4.1

Although it is difficult to quantify the moisture losses as a function of elapsing time for the subgrade soil, Table 19 and Table 20 present the time period of accelerated testing on each of the four sections during the accelerated testing APT I and APT II. The subgrade of the section reinforced by Grid A is expected to have the highest moisture content and lowest stiffness when the section with Grid A was subjected to the accelerated testing.

Table 19. Time period of accelerated testing on the four sections in Instrumented APT I*

Sections	**Time Period**	**Days After Subgrade Construction**
Grid A	May 12 – May 24, 2010	23 – 35
Control	May 25 – May 29, 2010	36 – 40
Grid B	May 31 – June 3, 2010	42 – 45
Grid C	June 3 – June 7, 2010	45 – 49

*Subgrade was constructed on April 20, 2010

Table 20. Time period of accelerated testing on the four sections in Instrumented APT II*

Sections	**Time Period**	**Days After Subgrade Construction**
Grid A	Aug. 20 – Aug. 23, 2010	30 – 34
Control	Aug. 24 – Aug. 26, 2010	34 – 37
Grid B	Aug. 26 – Aug. 29, 2010	37 – 40
Grid C	Aug. 30 – Sept. 1, 2010	41 – 43

*Subgrade was constructed on July 21, 2010

Variation in Asphalt Concrete Temperatures

The asphalt concrete temperatures were recorded throughout the accelerated testing for each of the four sections. As can be seen in Figure 25, the difference in temperatures between the control section and sections reinforced by Grid B and Grid C is negligible while temperatures of the section with Grid A were relatively lower during the testing in Instrumented APT I. The average values of the recorded temperatures for sections with Grid A, Grid B, Grid C and control section are: 23.4 °C, 25.7 °C, 26.2 °C, and 25.6 °C. The average temperature during the testing of the section with Grid A was about 2 °C less than the average temperatures of the other three sections. Temperatures in Instrumented APT II tests showed less variation than that in Instrument APT I tests. Based on these temperature measurements, the variation in asphalt temperatures does not play a role in the inconsistency of asphalt rutting.

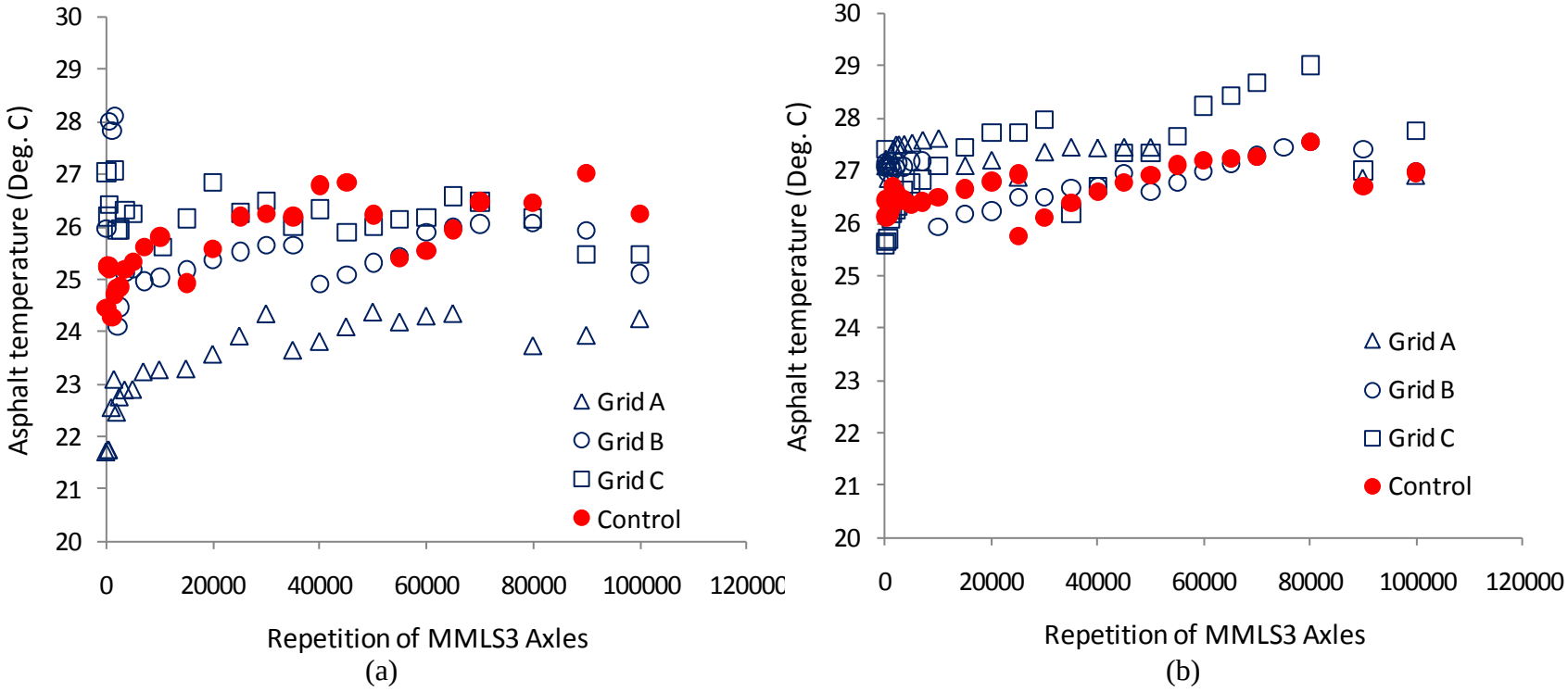

Figure 25. Recorded asphalt temperatures during the MMLS3 testing: (a) Instrumented APT I; (b) Instrumented APT II

Variation in Asphalt Concrete Air Voids

Asphalt rutting is due to two primary mechanisms: material densification or vertical compression, and lateral flow or plastic movement. The densification of materials is mostly associated with inadequate compaction (high air voids) of the asphalt layer, while the lateral flow is mostly due to the inadequate shear strength of the asphalt mixtures. Thus, the construction variability, particularly the compaction effort, may contribute to the difference in pavement performance.

The surface rutting, measured using the profilometer at intervals of MMLS3 load applications, is essentially the total permanent deformation of the entire pavement structure, including permanent deformation in the asphalt layer, permanent deformation in the base layer, and the subgrade permanent deformation. Recalling that the geogrids were primarily used to reinforce the weak subgrade (i.e., reduce subgrade permanent deformation), it would be ideal for all the different sections to have the same or similar permanent deformation in the asphalt layer and base layer such that the effectiveness of geogrid reinforcement in reducing pavement permanent deformation could be directly compared. Thus, it is necessary to minimize the effects of air voids variability on the asphalt concrete rutting.

Given the same loading conditions, the degree of densification of the asphalt layer for different sections is mostly affected by the initial air voids, although the conditions of being reinforced by geogrids or not and by different geogrid products may also affect the degree of densification to a certain extent. The densification of the asphalt mixture is the reduction of its volume and is assumed to be linearly proportional to the reduction in the air void content. Assuming the volume change or densification of the asphalt layer occurs in the vertical direction only, a given change in air voids causes the same percent of change in the thickness of the asphalt layer, although the asphalt mixtures are actually compressed in all three directions.

The surface rutting for each section in Instrumented APT I and Instrumented APT II was normalized to the change of air voids in the section, as summarized in Table 21 and Table 22. Surface rutting is the average of measurements taken at six locations along the wheel path. The measured air void values are averages taken across the tested section. By normalizing the surface rutting (total permanent deformation) of the pavement to the asphalt air voids, it was assumed that the deformation in the base and subgrade was similar between sections in each APT. The normalized rutting value, RD_{norm}, was calculated for each section as:

$$RD_{norm} = RD \times \frac{V_{Acontr.}}{V_{Ai}} \quad (1)$$

where RD is the measured surface rutting

$V_{Acontr.}$ is the average value of the air voids for the control (unreinforced) section, %

V_{Ai} is the average value of air voids for the reinforced section of interest, %

Table 21. Measured air voids of asphalt concrete before and after the accelerated testing in ***Instrumented APT I***

Sections	**Air Voids Before Testing (%)**	**Air Voids After Testing (%)**	**Air Void Change (%)**
Grid A	9.2	6.1	3.1
Grid B	9.1	5.1	4.0
Grid C	7.6	4.6	3.0
Control	7.3	5.6	1.7

Table 22. Air voids of asphalt concrete before and after the accelerated testing for a sample within wheel path in ***Instrumented APT II***

Sections	**Air Voids Before Testing (%)***	**Air Voids After Testing (%)****	**Air Void Change (%)**
Grid A	12.8	11.2	1.6
Grid B	14.5	11.2	3.3
Grid C	13.5	10.2	3.3
Control	11.6	10.1	1.5

* Measured using a pavement quality indicator (PQI)

** Measured from core samples

Figure 26 shows the measured rutting accumulation along with the number of MMLS3 load applications for sections in both APTs. The rutting accumulation appears to be either the same as the control or greater than the control when a geogrid is present. Figure 27 shows the rutting accumulation for each section after being normalized to the change of the asphalt air voids of the section. The normalized rutting indicates that Grid B and Grid C provided considerable benefits in reducing the total permanent deformation compared to the control case through both sets of accelerated tests. Grid A showed inconsistent reinforcing effectiveness between the two APTs. While it appears that Grid A does not improve the performance of pavements built on soft subgrade, the limited number of testing replicates in this study do not

support a definitive conclusion. Until more testing can be completed, caution should be exercised when using Grid A under conditions similar to those in this study.

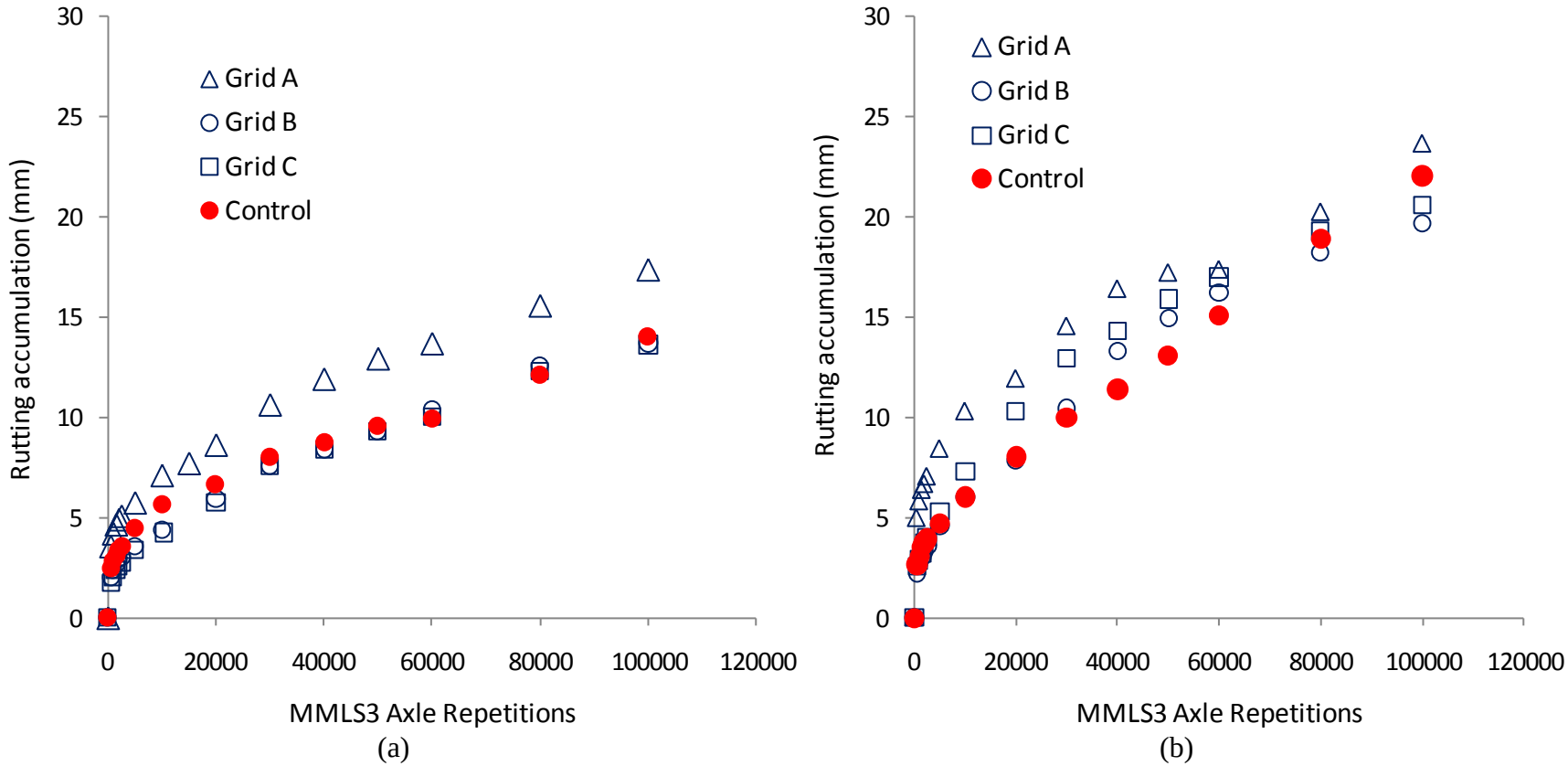

Figure 26. Average accumulation of surface rutting with MMLS3 load applications: (a) Instrumented APT I, (b) Instrumented APT II

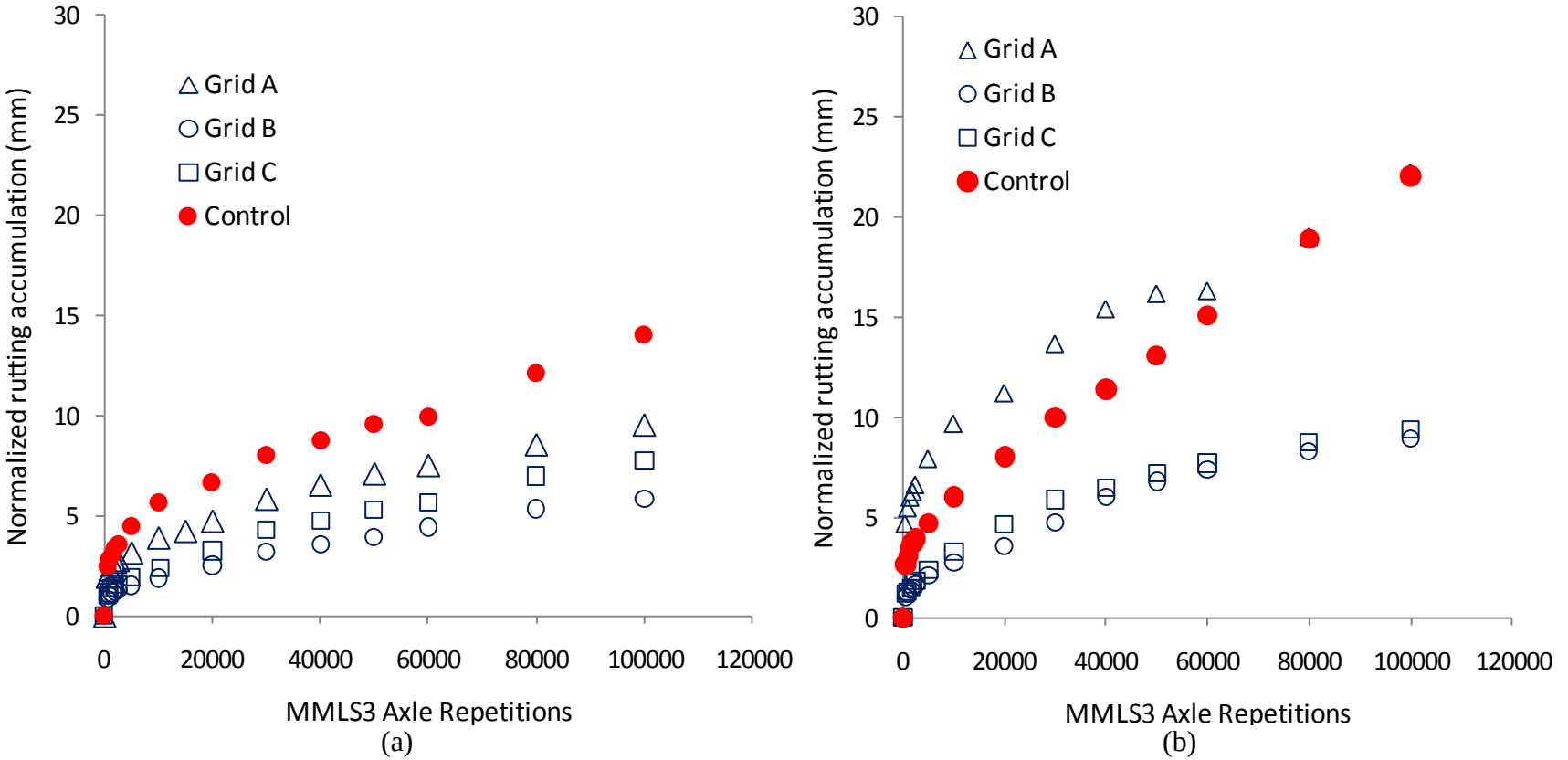

Figure 27. Accumulation of surface rutting ***normalized to the change of asphalt air voids*** for pavement sections in: (a) Instrumented APT I, (b) Instrumented APT II

5.5.3 Subgrade Deformation

Both permanent and elastic deformations of subgrade were measured at intervals of MMLS3 traffic. The circular plate affixed to the contact tip of the LVDT travelled simultaneously with the deflection and recovery of the subgrade. Thus, the elastic deflection of the subgrade was able to be measured by the LVDT. Figure 28-a shows a typical measurement from the LVDT over the time period of four MMLS3 wheel passes. The raw measurements were filtered to eliminate measuring noises. The baseline reading was subtracted from the LVDT measurements to obtain the elastic deformation corresponding to the load of MMLS3 (Figure 28-b). It can be seen that the peak value of subgrade deflection due to the MMLS3 wheel load is around 0.24 mm.

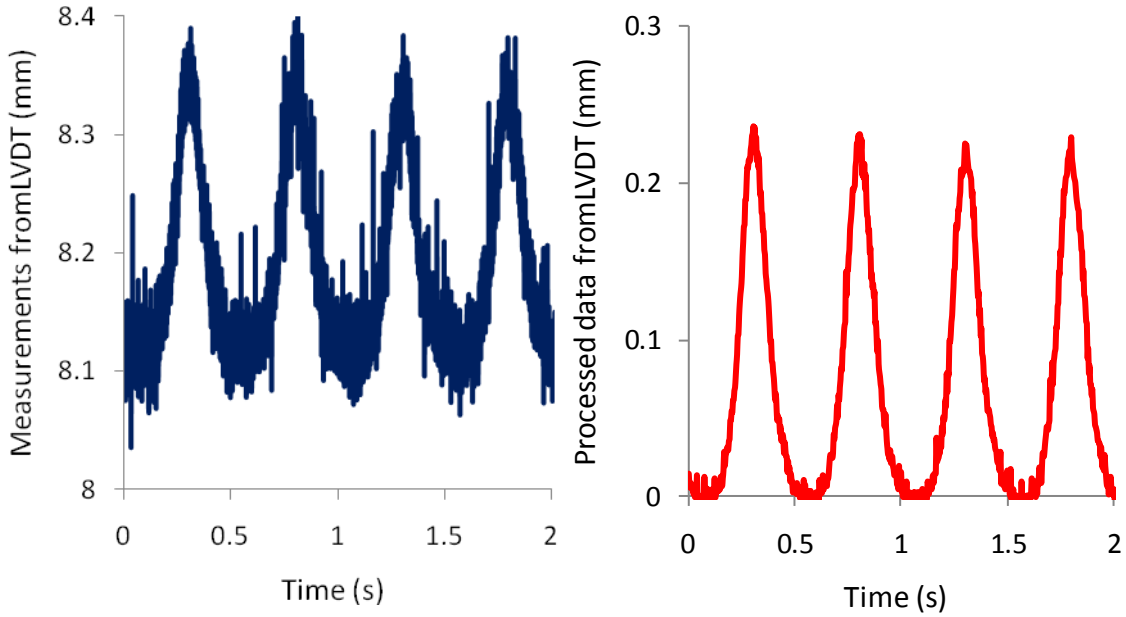

(a) (b)

Figure 28. Dynamic responses of LVDTs to the MMLS3 load: (a) LVDT measurements; (b) processed LVDT data

As previously mentioned, the LVDTs were mounted into a steel tube whose end was fixed at the bottom of the subgrade. Therefore, the permanent deformation measured by LVDTs represented the overall deformation of the entire subgrade layer. Figure 29-a shows the accumulation of permanent deformation along with the amount of MMLS3

load applications for sections in Instrumented APT I. As can be seen in Figure 29-a, the control section has a slightly larger deformation than the section reinforced by Grid A at the end of 100,000 MMLS3 load applications, while the pavement sections reinforced by Grids B and C show significantly less permanent deformation, which is consistent with the rank of surface rutting resistance (**Figure 26**).

In Instrumented APT II (Figure 29-b), Grid B and Grid C again showed improvements in resisting subgrade permanent deformation. Similarly with the surface rutting behavior (**Figure 26**-b), Grid A showed more deformation than the control section, especially at low numbers of axle load repetitions.

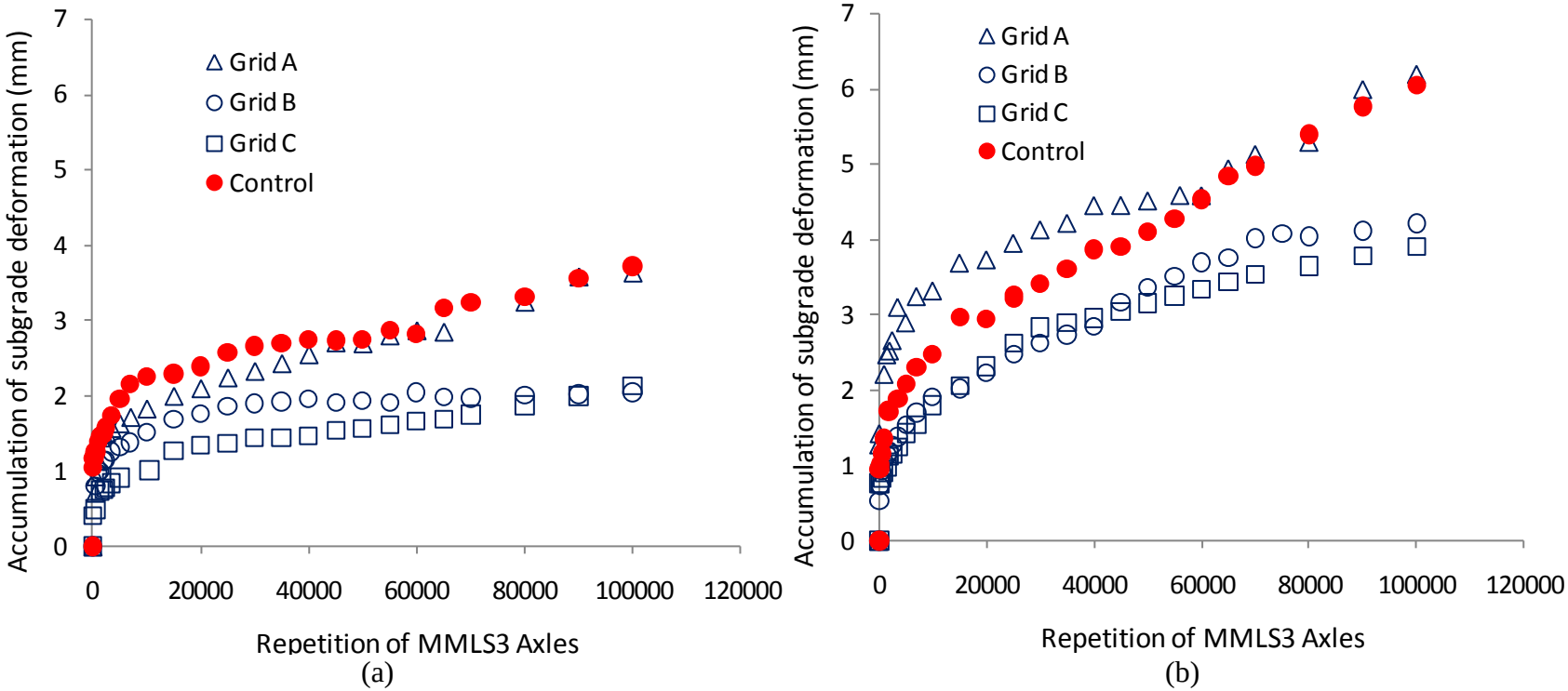

Figure 29. Accumulation of subgrade permanent deformation for sections in: (a) Instrumented APT I; (b) Instrumented APT II

5.5.4 Vertical Stress atop Subgrade

The dynamic responses of pressure cells to the MMLS3 load were recorded and processced by following the similar procedures with the LVDTs dynamic measurements. Figure 30-a displays the raw data of pressure cell measuremens and processed data. Figure 30-b shows the processed data after the removal of spikes in the raw data. As can be seen in Figure 30-b, the maximum vertical stress at the top of subgrade applied by the MMLS3 is about 27 kPa (3.9 psi). The peak value of the vertical stress measurements will be used in an inverse analysis procedure to backcalculate pavement layer properties.

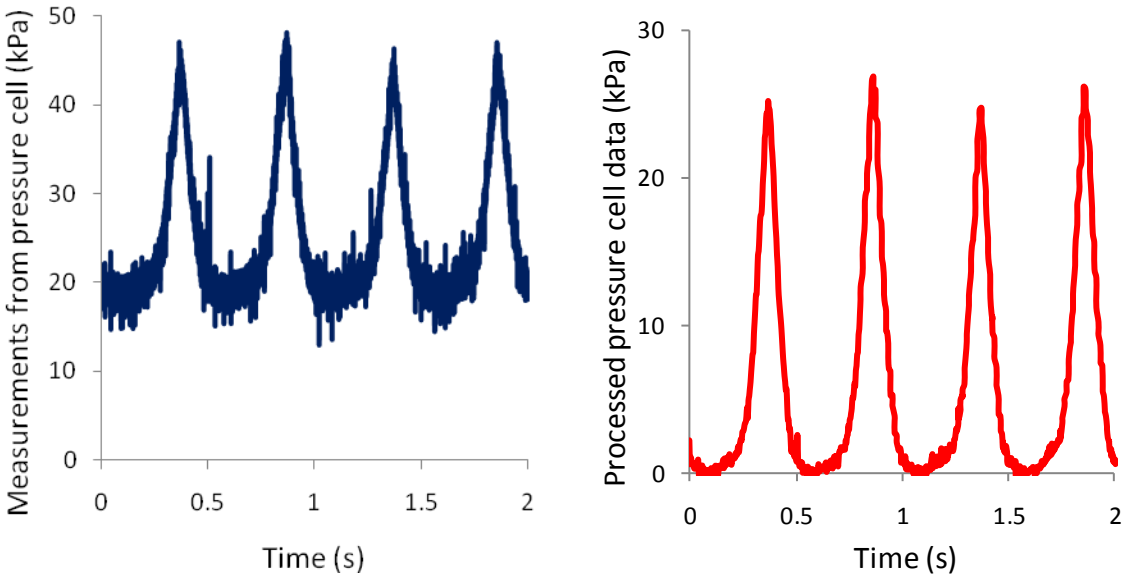

(a) (b)

Figure 30. Dynamic responses of pressure cells to the MMLS3 load: (a) Pressure cells measurements; (b) processed pressure cell data

5.5.5 Strains Developed in Geogrids

For each geogrid, a total of eight strain gages were installed at four geogrid ribs on both lower and upper surface of each rib. For each rib, the strains developed in the geogrid were the average of measurements from the pair of gages attached on both faces to minimize the bending effects on strain gages due to the out- of- plane load. All the strain gage measurements were corrected by scale factors to account for the local stiffening effects due to the adhesive and coating.

Figure 31 shows a snapshot of typical responses of strain gages to dynamic MMLS3 wheel load over the time period of two seconds at the MMLS3 axle number of 50,000. The two pairs of strain gages shown in Figure 31 were installed on two geogrid ribs of Grid C adjacent to each other in machine direction (MD) and cross-machine direction (TD). According to the way the geogrid was laid out in the pavement, the machine direction (MD) is parallel to the MMLS3 wheel path while the cross-machine direction is perpendicular to the wheel path. The vertical wheel load applied on the geogrid plane bent the geogrid ribs to some degree. As expected, the strain gages installed on top surfaces of the ribs were in compression (negative values) while the gages on bottom surfaces were in tension (positive values) as Figure 31 shows. It is therefore necessary to average the measurements of the pair of strain gages on each rib to minimize the effects due to bending and to extract the tensile strains developed in the ribs that are associated with the geogrid reinforcing effectiveness.

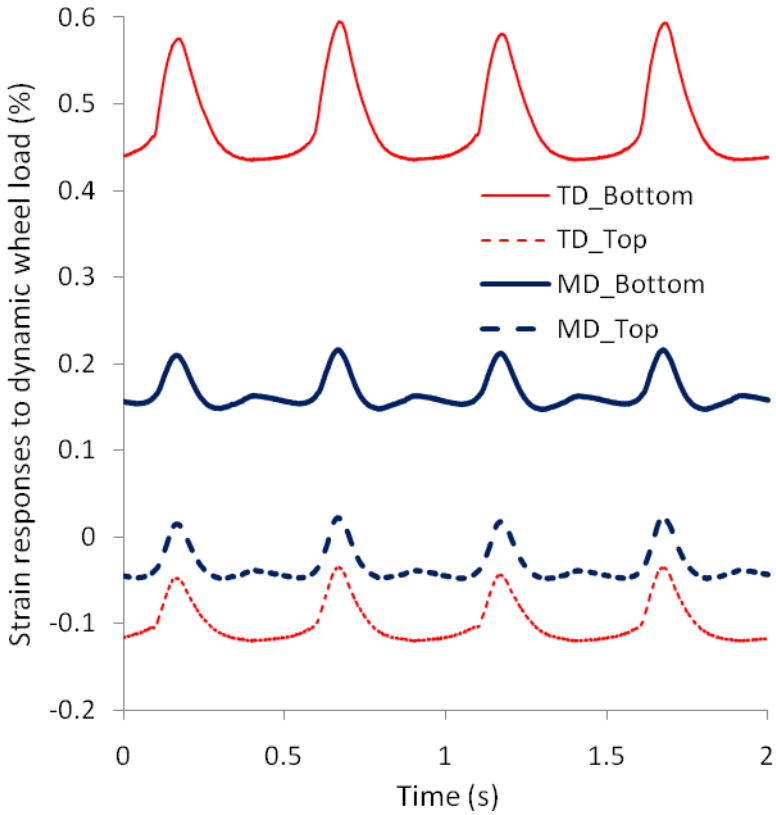

Figure 31. A snapshot of typical responses of strain gages on Grid C to dynamic wheel load at the axle number of 50,000 during Instrumented APT I

Figure 32 is presented to show the permanent strains developed in geogrid rib of Grid C. The opposite signs of measurements from the strain gage on bottom and top surfaces furthermore indicate the stress state of the geogrid rib in the pavement system under the vertical wheel load.

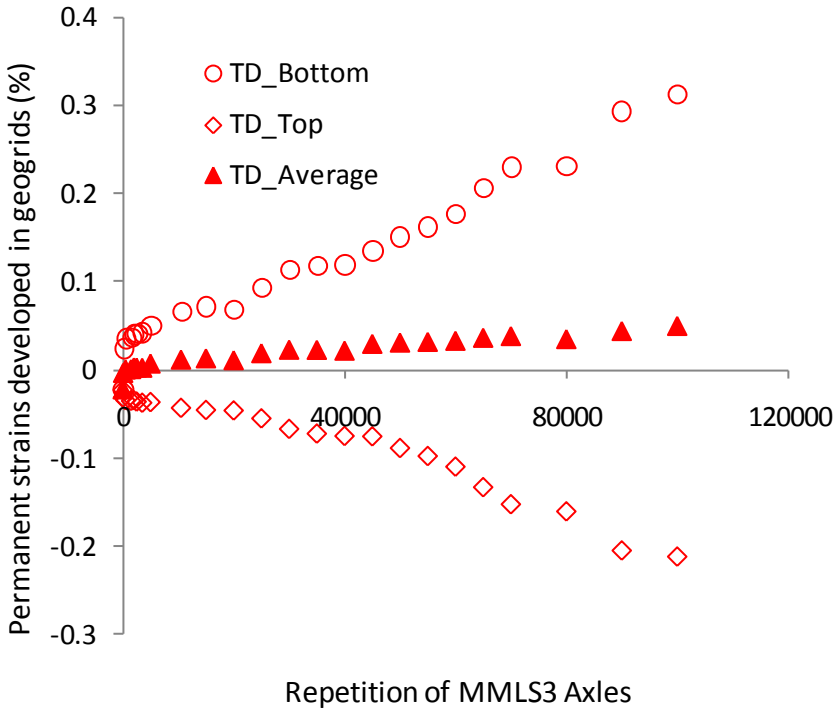

Figure 32. Permanent strains developed in a geogrid rib of Grid C in the cross-machine direction during Instrumented APT I

Figure 33 and Figure 34 displays the permanent geogrid strains measured in longitudinal direction at two different locations. The measurements of strains developed in geogrids can be an indicator on how much the geogrids were mobilized and engaged with the pavement system in resisting the axle load. It appears Grid B and Grid C developed more strains throught the testing.

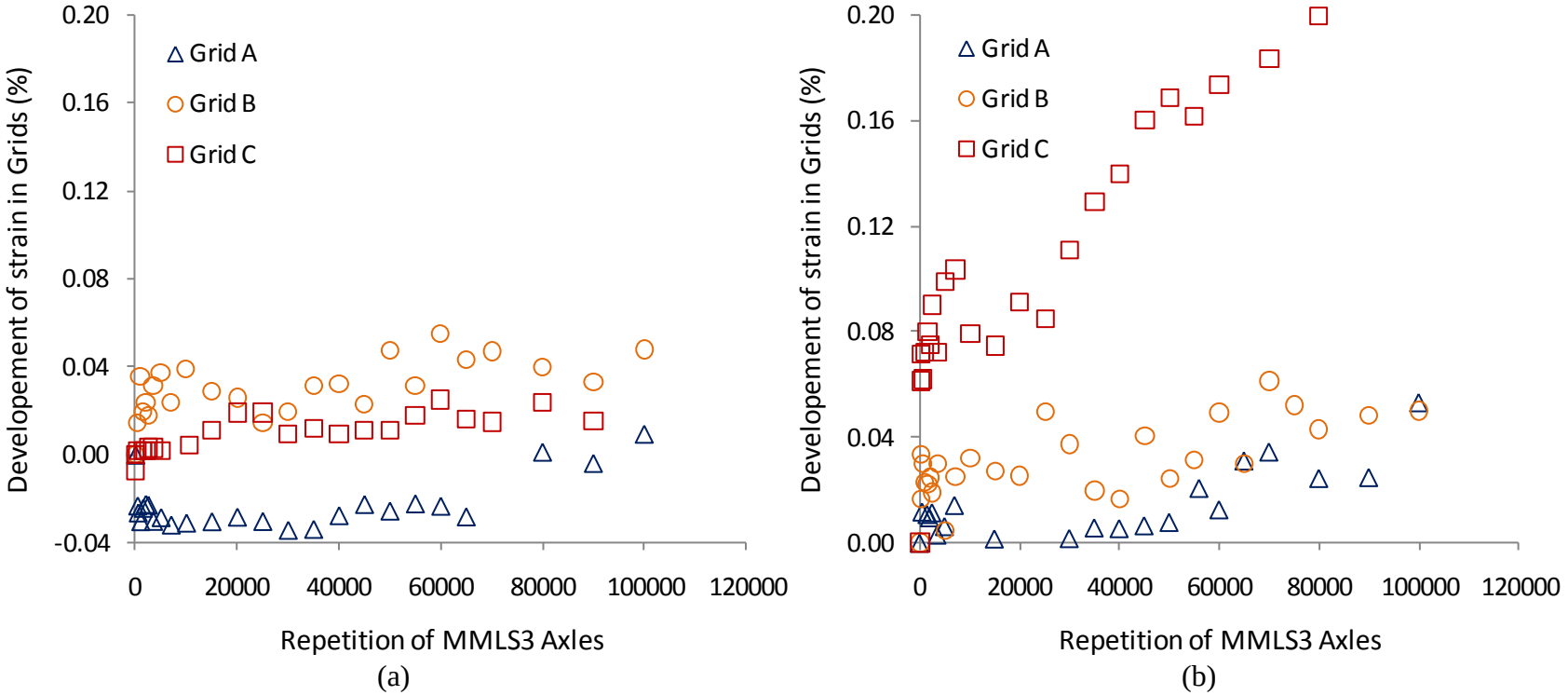

Figure 33. Strains developed in geogrids at location of NC in longitudinal direction: (a) Instrumented APT I; (b) Instrumented APT II

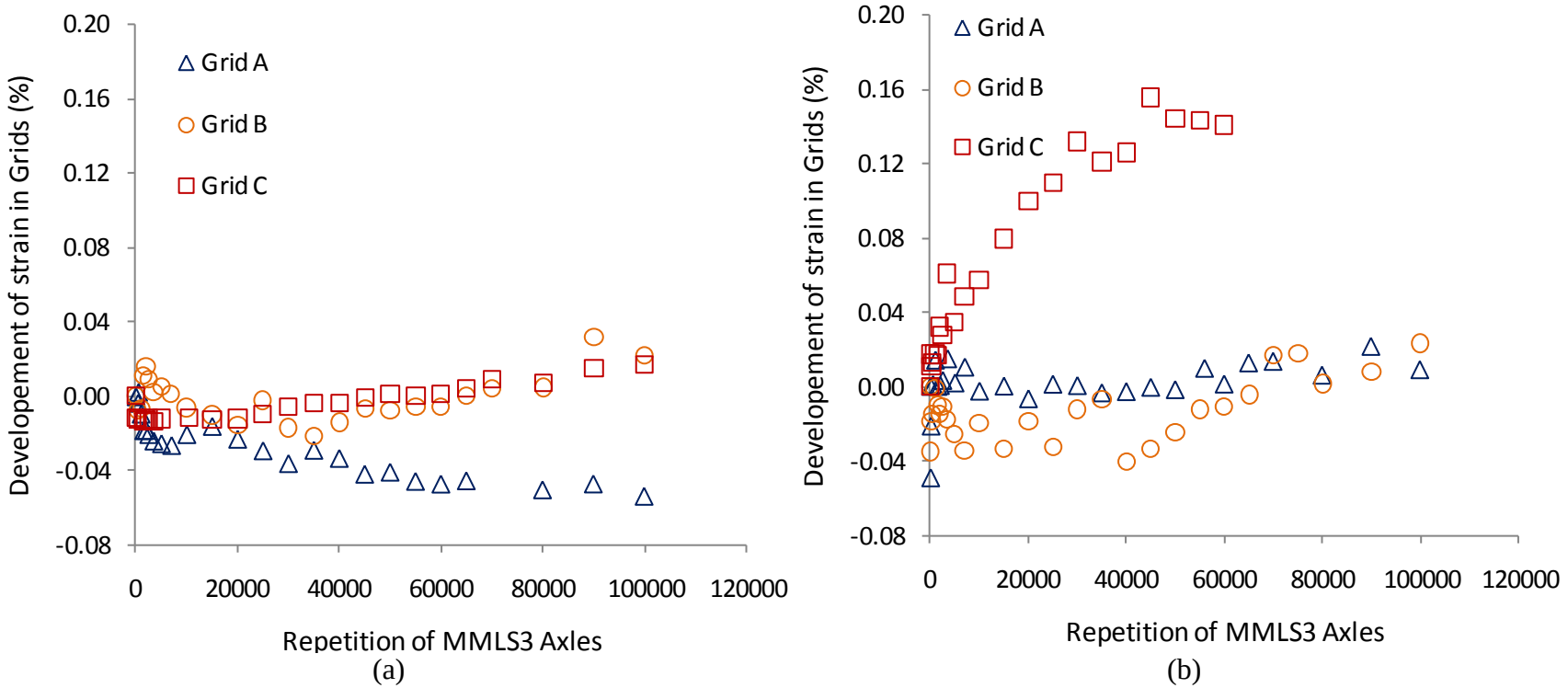

Figure 34. Strains developed in geogrids at location of FC in longitudinal direction: (a) Instrumented APT I; (b) Instrumented APT II

5.6 Summary and Conclusions

Two sets of accelerated testing designated as Instrumented APT I and Instrumented APT II were carried out to investigate the effectiveness of three different geogrids (Grid A, Grid B, and Grid C) in stabilizing weak subgrade and resisting permanent deformation. During each APT testing, four pavement sections were constructed, among which one was a control and the others were reinforced with different geogrids. Two different types of soil were investigated through the two accelerated tests.

Various instruments were installed in the pavement system to measure both static and dynamic response of the pavements. Deformation at the top of the subgrade was measured using LVDT in each section while the vertical stress at the top of the subgrade was monitored through earth pressure cells. Surface rutting was measured using a profilometer at intervals of the MMLS3 axle repetitions. Strains in the geogrids were measured using foil strain gages attached on the ribs. LWD tests were conducted on the pavement sections to backcalculate the pavement layer properties before the accelerated testing.

Central deflections of the LWD were used to compare the structural capacities among the sections. Reinforced sections in Instrumented APT I showed a slight decrease in the central deflection compared to the control section. However, no consistent evidence was found in sections of Instrumented APT II showing the reduction of surface deflection due to the geogrids.

Sections reinforced with Grid B and Grid C showed considerable reduction in surface rutting through the two rounds of accelerated testing after accounting for the effects of air void on asphalt concrete densification, while Grid A did not show consistent improvements in rutting resistance. Furthermore, the subgrade permanent deformation measurements demonstrated the effectiveness of Grid B and Grid C in reducing subgrade rutting. A discrepancy in Grid A's performance was also found in subgrade permanent deformation measurements in the two sets of accelerated testing. While it is not conclusive whether Grid A can improve the pavement performance, caution should be exercised when using Grid A for the similar conditions in this study.

6 DEVELOPMENT OF A RESPONSE MODEL FOR GEOGRID-REINFORCED FLEXIBLE PAVEMENTS

Pavement response models served two purposes in this study: (1) to provide a forward model for the inverse analysis procedure based on LWD tests; and (2) to predict pavement critical responses that were needed as the inputs in the mechanistic-empirical permanent deformation models based on MMLS3 tests. Although analytical solutions exist for a multi-layered pavement system, in this study, the Finite Element Method (FEM) was adopted to create response models for the pavement system because of its capability to consider inclusions of geogrids and site-specific boundaries. The general-purpose FE program ABAQUS was used to create the pavement response models. Assumptions of the geometries, boundary conditions, and material behaviors were made and discussed.

6.1 Model Geometry

It is ideal to use a three-dimensional FE model to simulate the actual geometries of the pavement testing sections. However, a 3-D model usually demands much more computational resources due to its larger amount of elements. Knowing that the FE model is called repeatedly during the inverse analysis, the cost of computational time and resources should be considered when creating the FE models.

The approximation of the LWD load and MMLS3 load as uniformly distributed circular loads led to axially symmetric loading conditions, which made it possible to employ the simplified axisymmetric models for the geometric model of the test section. The axisymmetric models were expected to be more computational resources-saving than 3-D models.

6.1.1 Axisymmetric Model

Figure 35-a shows the plan view of one test section. Up to the nearest boundary with a radial distance of 46 cm, the problem is symmetric with respect to the axis passing through the center of the loaded area. Through the axisymmetric model, the rectangular block is now reduced to a cylinder - the circle in Figure 35-a continues into the plane of the page to the depth of the pavement.

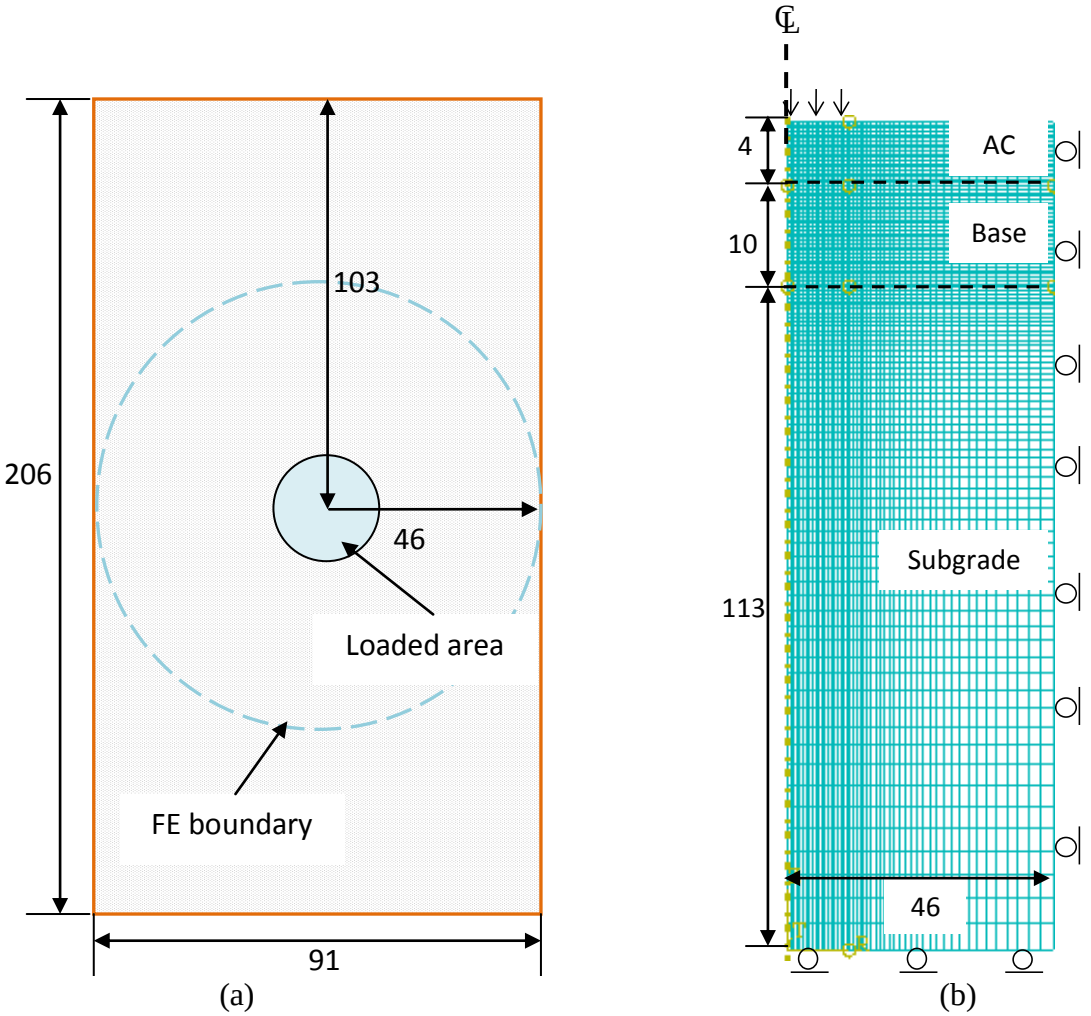

Figure 35. Geometries of the axisymmetric finite element model for the test section: (a) plan view of one test section with the circular area representing the FE geometric model; (b) cross-section view of the FE model (units in cm)

The body of the simplied cylinder can be generated by revolving a plane cross-section about the symmetry axis as Figure 35-b shows. An element of the cylinder can be described in cylindrical coordinates *r*, *z*, and θ (Figure 36). Knowing that the load distribution is independent of θ, with *r*, *z*, and θ being the three principal directions, there are three normal stresses, σ_{rr}, σ_{zz}, and $\sigma_{\theta\theta}$, and one shear stress, τ_{rz} which is equal to τ_{zr}. The deformation of any *r*-*z* plane represents the state of the strain and stress in the cylindrical body. Therefore, the problem can be reduced into a two-dimensional plane problem as shown in Figure 35-b.

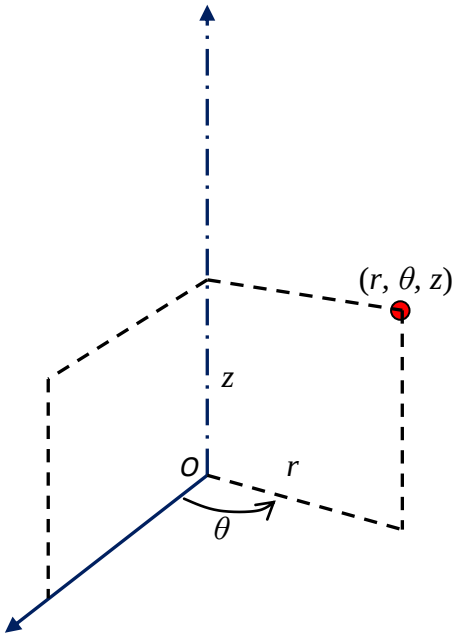

Figure 36. An element expressed in cylindrical coordinates

6. 1.2 Boundary Conditions

As discussed above, the test section virtually of a rectangular block was simplified into a cylinder with the radius of distance from the load center to the nearest boundary. In finite element, this simplified cylindrical problem was solved by two-dimensional axisymmetric model. For the two-dimensional axisymmetric model in ABAQUS, boundaries were assigned onto both the outer perimeter and the rotation axis, and the bottom of the model. It should be pointed out that boundaries were added to the symmetry axis in ABAQUS, although the axis physically is the central line of the cylinder and does not have boundaries.

The nodes on the rotation axis and outer perimeter were restrained in the radial direction but allowed to move in the vertical direction. The nodes on the bottom of the model were restrained in the vertical direction.

6.2 Modeling Techniques

ABAQUS provides various first and second-order isoparametric solid elements. For an axisymmetric model, there are first-order 4-node quadrilateral elements and second-order 8-node quadrilateral elements available. Although second-order elements

provide higher accuracy than the first-order elements, they tend to show difficulties in solving problems with contact conditions and impact involved (SIMULIA, 2009).

The first-order 4-node quadrilateral elements (CAX4R) were chosen for simulating the pavement models. The 4-node bilinear element has four nodes and a total of eight degrees of freedom with each node having two degrees of freedom in the directions of *r* and *z* (Figure 37).

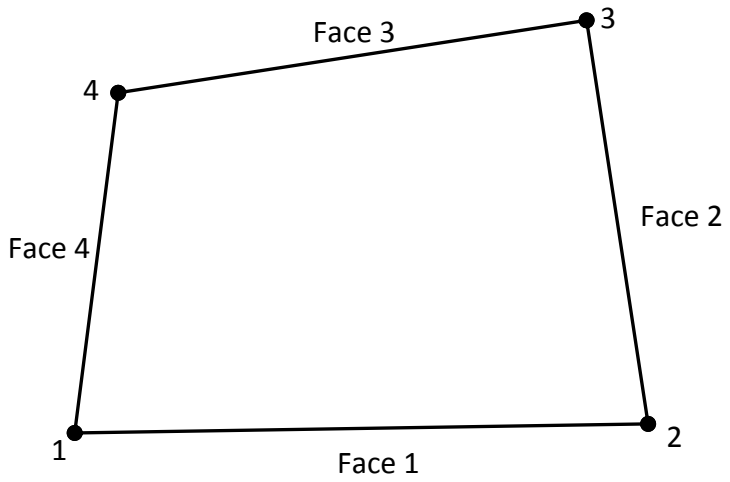

Figure 37. First order 4-node bilinear solid element for pavements

Geogrids in the pavement system were simulated as membranes. Linear 2-node membrane element (MAX1) was chosen as the element for membranes in an axisymmetric model. This type of element can take only in-plane tensile stresses but not normal stresses. A finite thickness of 1 mm was specified for the membranes.

Non-uniform meshes were used to discretize the model. Finer meshes were assigned at the regions closer to the load and of greater interests (Figure 35-b).

6.3 Material Properties and Interface Models

Pavement materials in the FE models were assumed to be linear elastic although they may exhibit nonlinear behaviors, for instance the aggregate base typically shows stress-dependence and the asphalt concrete posses time-dependency. The value of the elastic moduli for each pavement layer was obtained through an inverse analysis procedure which will be detailed in the subsequent chapter. Poisson's ratio for the asphalt

concrete, aggregate base, and soil subgrade were assumed to be: 0.30, 0.35, and 0.45, respectively.

The geogrids were simplified as continuous membranes embedded between the base course and subgrade. The direction-dependent character of the geogrid was not considered. The elastic moduli for the three different geogrids were based on the tensile modulus tested using wide-width tensile tests as listed in Table 7. The tensile modulus was converted into elastic modulus by dividing the thickness of the membrane (1 mm). The average value of the modulus in machine direction (MD) and cross machine direction (TD) was assumed to be the in-plane elastic modulus of the geogrids. Poisson's ratio of 0.45 was assigned to all the three geogrids. Table 23 presents the material properties that were used in the FE models.

Table 23. Material properties in the FE models

Material	**Modulus (MPa)**	**Poisson's Ratio**
Asphalt Concrete	1684.0	0.30
Aggregate Base	43.5	0.35
Soil Subgrade	12.2	0.45
Grid A	4.1	0.45
Grid B	6.1	0.45
Grid C	4.0	0.45

For a reinforced pavement section, there are a total of three interfaces: asphalt-base, base-geogrid, and geogrid-subgrade. The asphalt-base interface was assumed to be fully bonded while the base-geogrid-subgrade interface was an important character of the FE model to simulate the reinforcing effects of geogrids. The geogrid is generally considered to be able to improve the shear resistance when it is embedded in the pavement and well interlocked with pavement materials. The shear resistance behavior of the geogrid-pavement materials interface can be characterized through a shear stiffness or modulus defined as below (Perkins et al. 2004):

$$G_I = \frac{\tau_I}{\delta_I} \tag{21}$$

where G_I is the resilient interface shear modulus, N/m^3 (note the unit)

τ_I is the shear stress applied to the interface, N/m^2

δ_I is the relative displacement between the geogrids and pavement layers, m

In the FE models, the Coulomb friction model that has been used by previous researchers was adopted to address the shear resistance interaction between the geogrid and pavement materials (Perkins 2001; Leng 2002). Figure 38 illustrates the concepts of the Coulomb model. Both shear forces and normal forces are transmitted across the interface when two frictional surfaces are in contact. The relationship between the shear stress, τ and normal stress, σ determines the coefficient of friction, μ as Figure 38-a shows. Before the interface yields, the relative displacement between the two surfaces is considered elastic and controlled by the shear stress and the shear modulus (Figure 38-b).

Based on the discussion above, the shear modulus can be expressed as follows:

$$G_I = \frac{\tau_{\max}}{E_{slip}} = \frac{\mu\sigma}{E_{slip}} \tag{22}$$

For the FE models the elastic slip E_{slip} and the coefficient of friction, μ are the two input values. The coefficients of friction of the interfaces were determined from the direct shear tests as listed in Table 8. Additionally, in order to solve for the value of E_{slip} in Equation 23, it needs to know the normal stress at the interface. The interface stress state was estimated from the FE model for a control section under the MMLS3 load. The value of normal stress at the interface is about 14.2 kPa (2.1 psi) under the MMLS3 load.

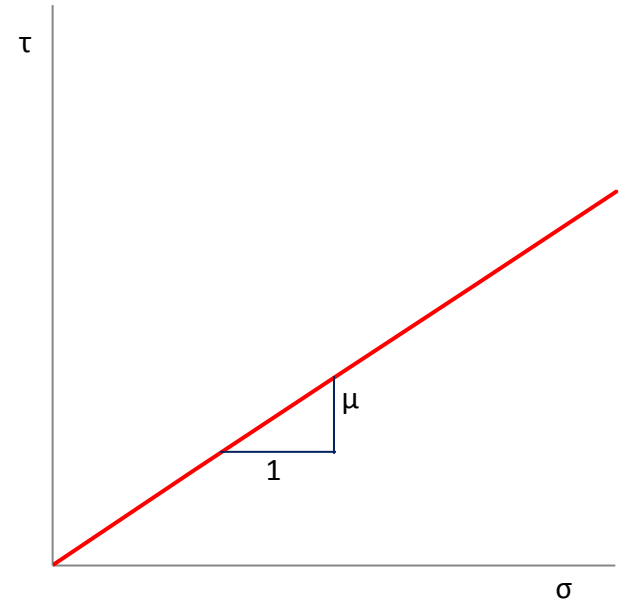

(a)

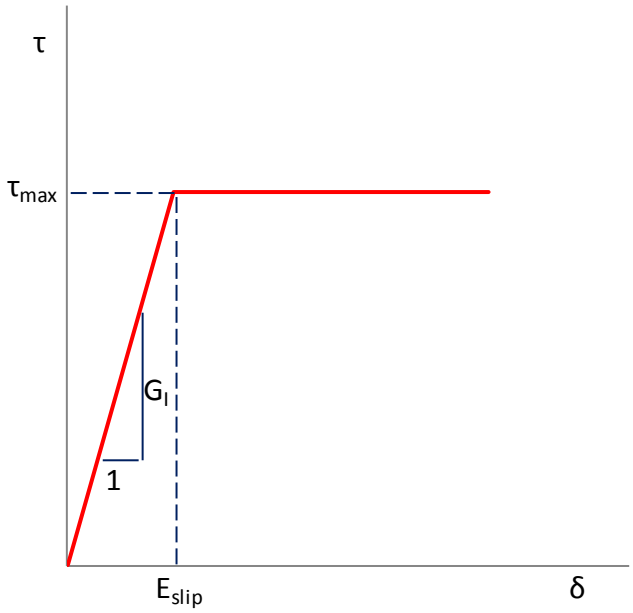

(b)

Figure 38. Coulomb friction model for the geogrid-pavement interface: (a) relationship between the shear stress and normal stress; (b) relationship between the shear stress and relative displacement

While it is ideal to test the shear modulus values through pullout tests under similar conditions in the pavement, only static pullout tests for geogrids embedded in the aggregates used in the accelerated testing were performed in this study. The pullout tests

results at small displacement (see Figure 14) were used to calculate the shear modulus (G_I) based on Equation 22. The shear stress was calculated as the pulling force divided by the area of the geogrid sample. It is noted that the normal stress applied during the pullout tests was 6.9 kPa (1.0 psi) which is only half of the vertical stress at the interface (14.2 kPa / 2.1 psi) calculated from the FE model of a control section. Greater shear modulus is expected when higher normal stress is applied upon the interface. The shear modulus for all the interfaces calculated based on the pullout results were multiplied by ten in order to account for the higher normal stress at the interfaces and to achieve reasonable values of elastic slip (E_{slip}).

Table 24 provides a summary of the interface properties that are included in the FE models. It is noted that same properties were applied to the upper and lower contact surface of geogrids for each set of interface. In fact, more interaction between aggregates and geogrids is expected compared to the geogrid-subgrade interface. However, separate experimental investigations for the aggregate-geogrid and subgrade-geogrid interfaces are needed to distinguish the different behaviors. The upper and lower interfaces of the geogrid are assumed to be the same in this study.

Table 24. Interface parameters for the FE models

Interfaces	**Measured G_I (MPa/m)**	**Corrected G_I (MPa/m)**	**Normal Stress (MPa)**	**Coefficient of Friction**	**Elastic Slip (mm)**
Base-Grid A-Soil CL	0.15	1.5	0.0142	0.47	4.4
Base-Grid B-Soil CL	0.45	4.5	0.0142	0.47	1.5
Base-Grid C-Soil CL	0.28	2.8	0.0142	0.47	2.4
Base-Grid A-Soil ML	0.15	1.5	0.0142	0.47	4.4
Base-Grid B-Soil ML	0.45	4.5	0.0142	0.47	1.5
Base-Grid C-Soil ML	0.28	2.8	0.0142	0.49	2.4

6.4 Modeling the Effects of Geogrid Reinforcements

With the assumption of continuity for geogrids in the FE model, it is not possible to directly simulate the interlocking between the geogrid and surrounding pavement materials. In order to simulate the lateral constraints provided by the geogrids to the adjacent pavement layers, a thermal shrinkage was applied to the geogrids to mimic the shear resistance at the interface (Perkins et al, 2004). An unrealistic thermal coefficient of expansion, α equal to 1.0 $(°C)^{-1}$ was assigned to the membrane in the FE models. The initial temperature of the geogrids was set to be 0°C. A decrease in the temperature generates shrinking strains in the membrane based on the following:

$$\varepsilon = \alpha T \qquad (23)$$

The geogrid tends to shrink due to the reduction in temperature while the contacts defined by the Coulomb model between the geogrids and pavement base and subgrade constrain the geogrid to do so. Tensile stresses are therefore developed in the geogrid because of the constraints from the adjacent layers. Figure 39 shows the stresses in horizontal direction in the geogrids. As can be seen in Figure 39-a, the tensile stress (positive sign in the FE model) in the geogrids dominates within certain area and diminish beyond that zone. Figure 39-b displays the horizontal stresses in the geogrid from the central line to the outer boundary. Under the MMLS3 load, it appears that the geogrid was mobilized mainly up to the radial distance of 200 mm from the central line.

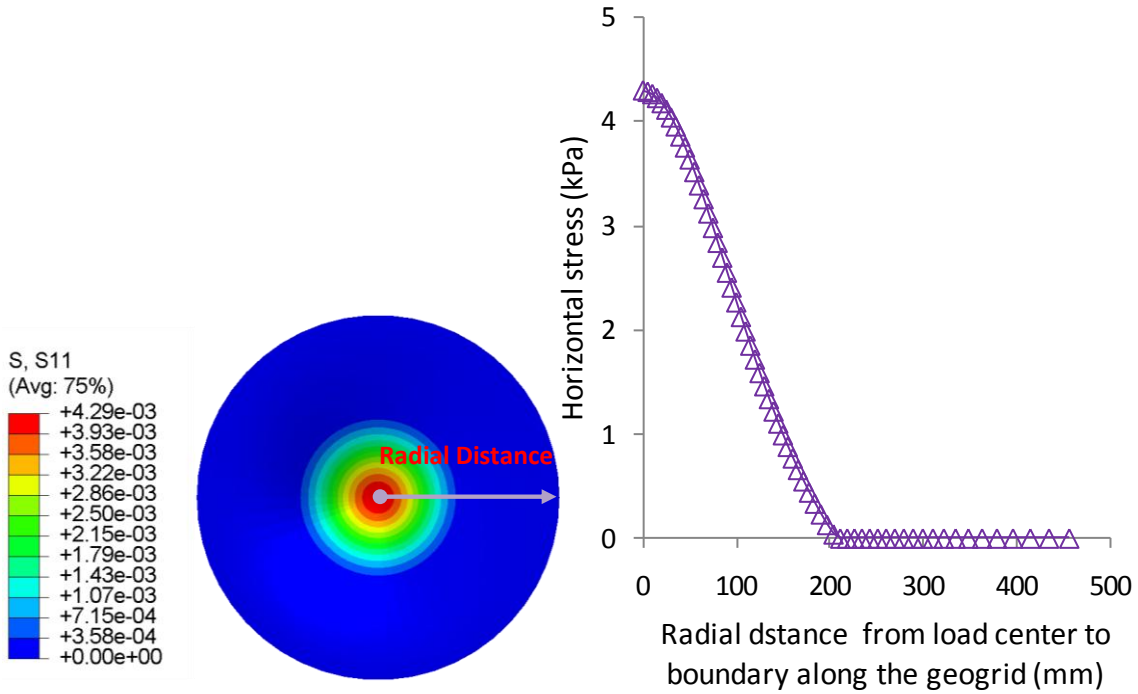

(a) (b)

Figure 39. Horizontal stresses developed in geogrid Grid B: (a) plan view of the geogrid in FE model with contour of the horizontal stress (units in MPa, positive signs represent tension in the FE models); (b) horizontal stress developed in the geogrid

The inclusion of geogrids is expected to improve the vertical stress distribution at the top of the subgrade such that the subgrade would experience less deformation. Figure 40 shows the vertical compressive stress in the reinforced and unreinforced pavement sections. With the same loading condition and pavement layer properties, it shows that the addition of geogrid reinforcement between the base and subgrade can reduce the vertical stress in the subgrade as illustrated in Figure 40.

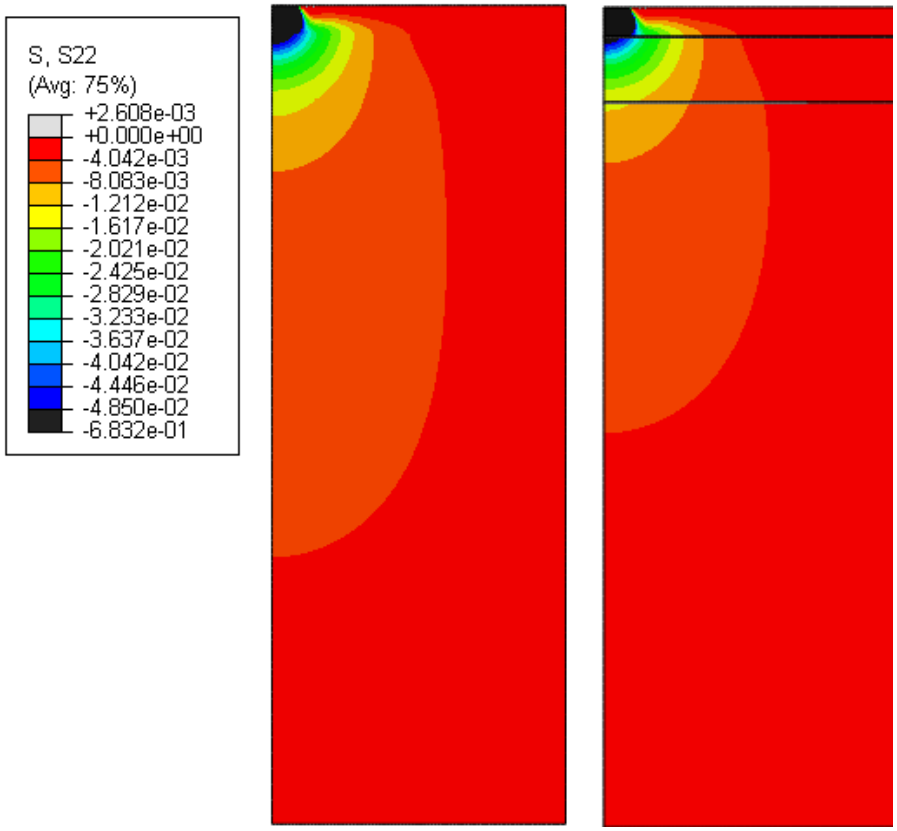

(a) (b)

Figure 40. Contour of the vertical stress in the FE model for pavement sections: (a) unreinforced section; (b) section reinforced with Grid B (units in MPa, negative signs represent compression in the FE models)

Figure 41 presents the vertical stress distribution from the load center to the outer boundary at the top of subgrade for the control section and a reinforced section. The most reduction of vertical stress at the top of subgrade occurred at the central axis due to the inclusion of geogrid reinforcement.

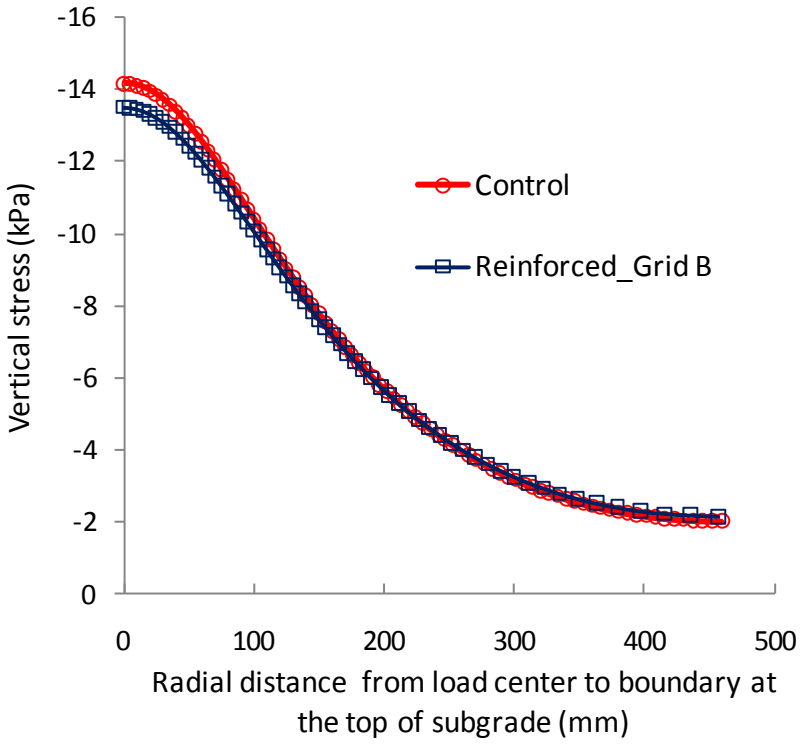

Figure 41. Vertical stress distribution at the top of subgrade calculated from FE models

7 CALIBRATION OF FE MODELS USING INVERSE ANALYSIS PROCEDURES

Calibration of the FE pavement responses models is a process of tuning the FE models such that the predicted pavement responses from the models match the measured pavement responses of the test section. In this study, pavement material property inputs were the variables that needed to be calibrated, while the pavement dimensions such as the layer thicknesses were known or the horizontal dimensions were assumed. The calibration was carried out based on the measurements of applied load and corresponding pavement responses from the LWD tests.

The calibration of pavement layer properties in the FE models is an inverse problem with known input signals into a system and known output signals based on which unknown system parameters are identified. In this study, the lightweight deflectometer was used to test the moduli of an instrumented three-layer pavement model. The recorded LWD peak load was used as the known inputs into the pavement system while the measured surface deflections and instrumentation measurements were considered as the outputs. While instrumentation measurements of pavement responses are typically used to verify backcalculated pavement layers moduli, they were used in the inverse analysis procedure for backcalculating the pavement layer properties in this study. Through the general inverse analysis procedure, consistent pavement layer properties were obtained based on the LWD deflection data and/or instrumentation measurements.

7.1 Inverse Analysis of Pavement Layer Parameters

Backcalculation of pavement layer properties based on the falling weight deflectometer (FWD) testing has been widely used as a tool for evaluating the structural capacity of pavements. The FWD back-calculation of pavement layer properties essentially is an inverse problem with known input signals into a system and known output signals based on which unknown system parameters are identified. It is, therefore, possible to backcalculate a pavement layers' properties from a known load applied to the pavement and properly measured pavement responses. In this case, the pavement

responses can be surface deflection or measurements of instruments installed in the pavement system.

Traditional backcalculation of pavement layer moduli involves using the measured deflection basin data, i.e. peak pavement surface deflections measured at the location underneath the impact load of FWD and locations with certain offsets from the load. Theoretical deflection basin under the applied load is first computed using a set of assumed pavement moduli (initial guess). The calculated theoretical deflection basin is then compared to the measured deflections. The assumed pavement moduli are iteratively adjusted until the difference between the theoretical and measured deflections reaches an acceptable match. Numerous computer programs were developed to automatically backcalculate pavement layer moduli based on FWD testing, just to name a few, MODCOMP, MODULUS, WESDEF, ELMOD, and EVERCALC etc. Most of these programs assume a uniformly distributed FWD load and rely on linear elastic theory to solve for the layer moduli.

The following aspects have been identified as critical issues in backcalculating pavement layer properties (Lytton 1989; SHRP 1991; Ullidtz and Coetzee 1995; Irwin 2002):

- Incorporation of material models to deal with stress-dependent nature of unbound pavement layers
- Consideration of interfaces or contact issues between pavement layers to deal with the estimation of overlay
- Dynamic analysis of FWD impact load
- Assessment of sensitivity of deflections to layer moduli and identify a relatively thin layer modulus

It is also recognized that the most reliable method to verify the backcalculated pavement layer moduli is to compare the predicted stresses and strains based on the backcalculated moduli to the measured values of stresses and strains in actual pavements. In fact, instrumentation appears to be the only way to verify the backcalculatecd layer moduli considering the fact that there are no viable and widely-recognized tools for testing in-situ moduli of pavement layers. Attempts were made to evaluate the laboratory and

backcalculated resilient moduli and showed significant discrepancies between resilient moduli determined from backcalculation and those determined through laboratory testing (Mikhail et al 1999).

In this study, a lightweight deflectometer (LWD) was used to test the moduli of the instrumented three-layer pavement model. The LWD tests were carried out on the base course layer and asphalt concrete layer along with the progress of the pavement construction. Based on the information of the recorded LWD data and instrumentation measurements, inverse analysis were conducted to backcalculate the pavement layer properties as listed in Table 25.

Table 25. Matrix of inverse analysis runs

Forward Analysis	Input Information	Output Information
Two-layer Linear Static	LWD Peak Load	Surface Deflection Subgrade Deflection
Three-Layer Linear Static	LWD Peak Load	Surface Deflection Subgrade Deflection Subgrade Vertical Stress

7.2 Inverse Analysis Procedures

A procedure of the inverse analysis coupling the forward modeling and the optimization process was adopted in this study to backcalculate pavement layer properties (see Figure 42). Reasonable initial assumptions of material properties were made before starting the inverse analysis. The least square error between measured and FE predicted pavement responses was the objective function. The process of minimizing the objective function was based on a so-called CMA-ES (Covariance Matrix Adaptation Evolution Strategy) optimization methodology developed by Hansen (2006). The optimization algorithm written in Python (Hansen, 2010) was able to communicate with the FE models created by using the ABAQUS Python scripts. Due to the nature of the optimization method, care had to be exercised to ensure the convergence was global. This was accomplished by assigning initial assumptions in a wide range and checking if the backcalculated results were similar.

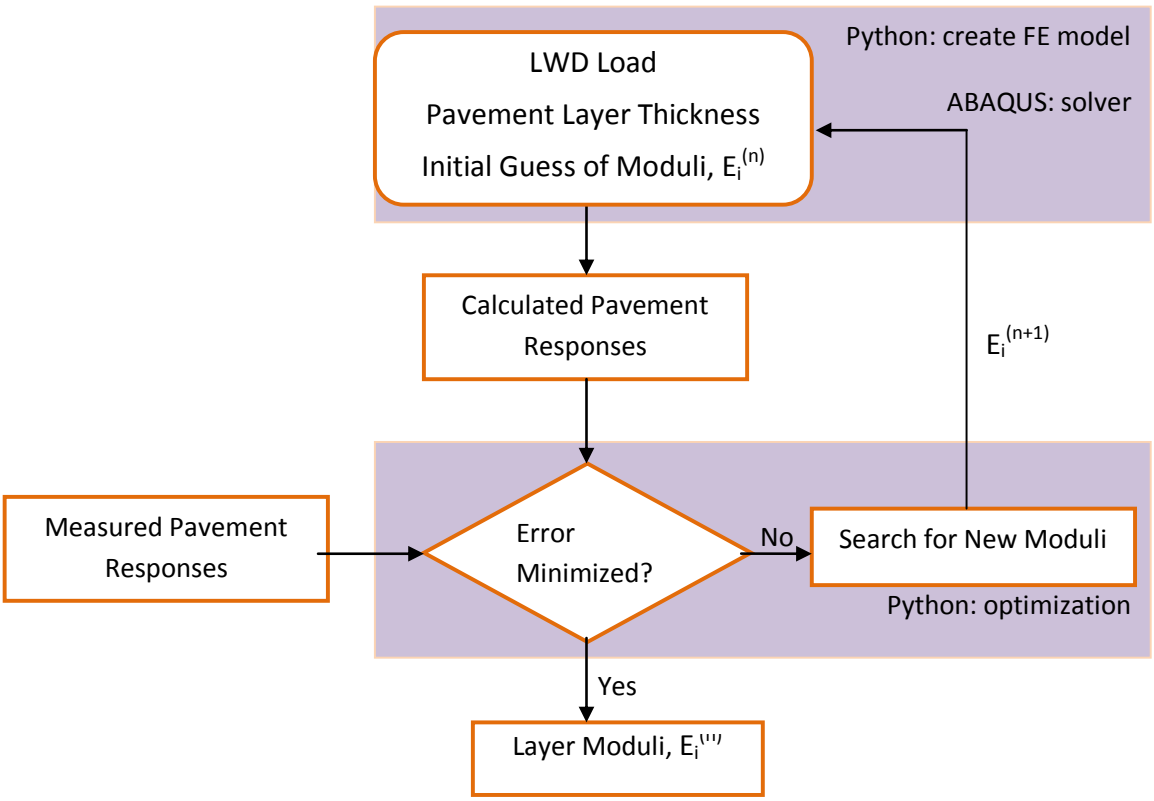

Figure 42. Inverse analysis procedure for identifying the pavement layer moduli

7.3 Optimization Method

Typically, an optimization problem includes the following three basic components:

- Optimization variables: these are usually the unknowns that need to be solved for, denoted as vector *x*.
- Constraints: the variables can be subjected to certain constraints in accordance with the physical meaning of the variables, denoted as $g(x) \leq 0$ and / or $h(x) = 0$.
- Objective function: it is also called cost function, denoted as $f(x)$.

To define an optimization problem, a feasible set S is defined as a collection of all the points that satisfy the constraints $g(x) = 0$ and / or $h(x) \leq 0$. Then the procedure of optimization is essentially to find a vector $x^* \in S$ such that $f(x^*) \leq f(x)$ for all $x \in S$. x^* is a local minimum if $f(x^*) \leq f(x)$ holds for all feasible x only in a small feasible neighborhood

of x^* while x^* is a global minimum when $f(x^*) \leq f(x)$ holds for all $x \in S$ as Figure 43 depicts.

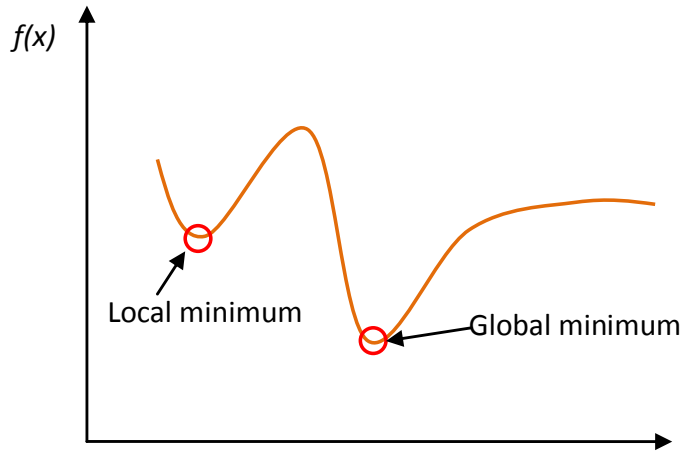

Figure 43. Local and global minimums of an objective function

7.3.1 Problem Formulation

In this study, the optimization variables / unknowns that need to be found through the inverse analysis procedure are the pavement layer elastic moduli. The Poisson's ratio were assumed and not considered optimization variables because they are not influential on the pavement response.

The general procedure of optimizing pavement layer moduli can be mathematically expressed as follows:

Minimize:

$$f(x),\ x \in S \subseteq \mathbb{R}^n$$

$$x = \{E_{asphalt}, E_{base}, E_{subgrade}\}$$

Subject to:

- Boundary constraints:

  $L_i \leq xi \leq U_i$

- Inequality constraints:

  $g_j(x) \leq 0$

f(x) is the objective function that need to be minimized. The objective function is the root mean squared error (RMSE) between the measured pavement responses from the LWD load and the calculated pavement responses from the FE model. Two measurements, base and subgrade deflections at the center of LWD load were used for the inverse analysis of the base-subgrade system to solve for two unknowns: E_{base} and $E_{subgrade}$. Three measurements (asphalt layer and subgrade deflections and vertical stress at the top of the subgrade) were used in the inverse analysis of the asphalt-base-subgrade system to solve for three unknowns: $E_{asphalt}$, E_{base} and $E_{subgrade}$. The objective function is defined as below:

$$f(x) = \sqrt{\frac{\sum_{i=1}^{n} (\delta_{mi} - \delta_{ci})^2}{(n-1)}} \qquad (24)$$

where δ_{mi} is measured values of pavement response such as surface and subgrade deflections.

δ_{ci} is calculated values of pavement response from the FE model.

x is a vector containing the variables that need to be optimized. In this study, the pavement layer moduli values are the optimization variables. The optimization variables fall into the search space *S* defined by the constraints. Broad yet reasonable bounds of the individual variable were specified as Table 26 presents.

Table 26. Bounds of the pavement layer moduli

Pavement Layers	**Elastic Modulus Ranges (MPa)**
Asphalt Concrete	1000 - 3000
Base Course	50 – 200
Subgrade	1 - 100

The constraints among the variables were also applied to the optimization procedure: $E_{subgrade} \leq E_{base} \leq E_{asphalt}$. It was expected to narrow the optimization search space by defining the bounds and constraints.

7.3.2 Optimization Method

It is recognized that the objective function in the problem formulation of this study is discontinuous and non-differentiable. Therefore, the traditional gradient-based optimization method such as steepest descent is not applicable to this category of problem because it requires the information about the gradient of the objective function. Other optimization methods such as direct search and evolutionary algorithms (EA) were reviewed and investigated. It was decided to use the Covariance Matrix Adaptation Evolutionary Strategy (CMAES) optimization algorithm considering its well recognized performance in solving difficult optimization problems (Hansen, 2006) and its successful application in backcalculating pavement layer properties (Gopalakrishnan and Manik, 2010).

CMAES is a population based algorithm. Unlike most direct search methods, the CMAES algorithm starts with a population of search points instead of a single point. An important and innovative feature of the CMAES algorithm is the definition of new search points. A new population is generated from a normal distribution expressed as below (Hansen, 2006):

$$x_k^{(g+1)} \sim N\left(m^{(g)}, (\sigma^{(g)})^2\, C^{(g)}\right) \qquad (25)$$

where $k = 1, 2, \ldots. \lambda$ and λ is the size of population.

$x_k^{(g+1)}$ is the k^{th} offspring / search points for generation g+1.

$N\left(m^{(g)}, (\sigma^{(g)})^2\, C^{(g)}\right)$ represents a multivariate normal distribution in generation g.

$m^{(g)}$ is the mean value of the search distribution at generation g.

$\sigma^{(g)}$ is the overall standard deviation, step size at generation g.

$C^{(g)}$ is the covariance matrix at generation g.

Each iteration or search step is accomplished by calculating values of $m^{(g)}$, $\sigma^{(g)}$,and $C^{(g)}$ for the next generation g+1. The following four parameters are the key operators in CMAES:

- Population size, adaptation, and change rates
- Population selection and recombination

- Step size control
- Covariance matrix adaptation

7.4 Verification of the Inverse Analysis Procedure using Synthetic Data

It is well-known that locating a global minimal is usually difficult not to mention verifying the global minimal. In order to ensure that the inverse procedure and the optimization algorithm work for the specific problem in this study, the procedure was subjected to an examination before it was applied to solve the problem. A set of synthetic pavement response data were generated from the FE model with assumed pavement layer moduli and the synthetic data were substituted for the measured values into the inverse procedure (Figure 42). The inverse procedure was then carried out to find the "known" assumed pavement layer moduli.

The examination was conducted for both the two-layer system and three-layer system as listed in Table 27. The difference between the backcalculated moduli values and the predefined layer moduli is negligible for both the two-layer and three-layer system, which indicates the inverse analysis procedures and the optimization algorithm are capable of finding the global or best minimum and accurately predict the pavement layer moduli.

Table 27. Results of inverse analysis using synthetic measurements

Runs	**FE Models**	**Synthetic Measurements**	**Assumed Layer Moduli (MPa)**	**Backcalculated Moduli (MPa)**
1	Two layer linear static	base deflection subgrade deflection	Base: 20.0 Subgrade: 10.0	Base: 20.0 Subgrade: 10.0
2	Three layer linear static	asphalt layer deflection subgrade deflection subgrade vertical stress	AC: 2000.0 Base: 20.0 Subgrade: 10.0	AC: 2007.0 Base: 19.9 Subgrade: 10.0

Figure 44 displays the change of root mean squared error values along with the optimization iteration steps. As can be seen, it took much more iterations for the inverse analysis on three-layer system to reach a satisfactory objective function value than that for the two-layer system.

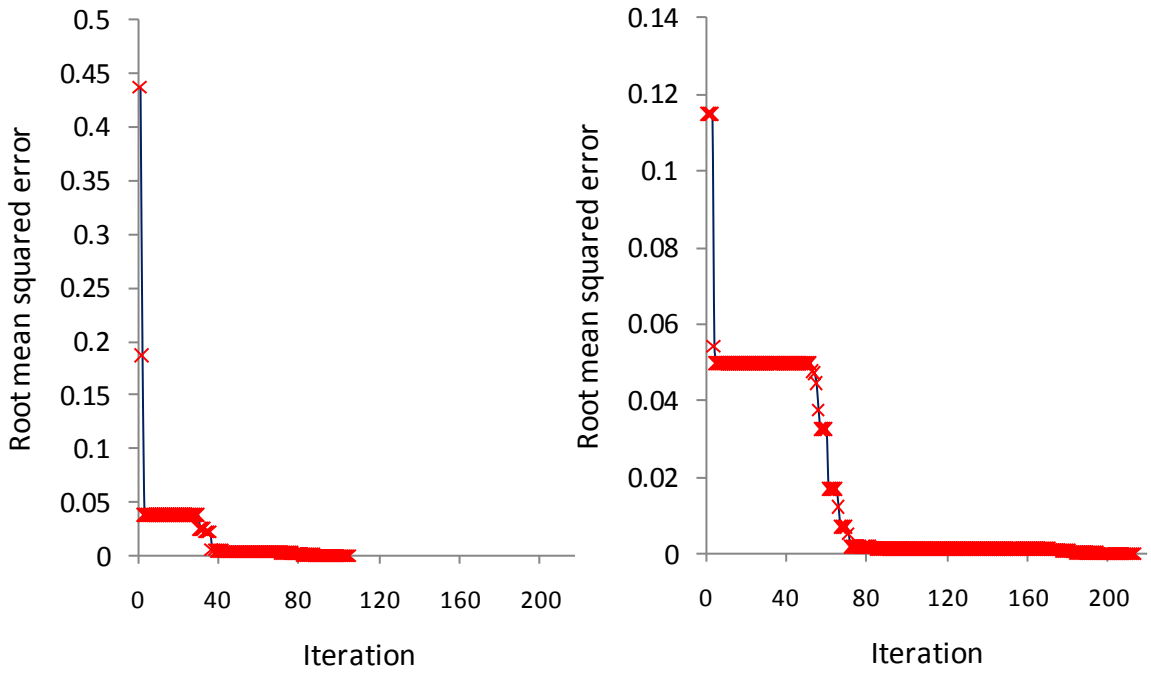

Figure 44. Root mean squared error along with the iteration: (a) two-layer system; (b) three-layer system

The verification tests on the inverse analysis procedure showed the procedure is a promising process to find the pavement layer moduli. However, it should be pointed out that the verification does not necessary guarantee that the inverse procedure adopted in this study will be able to find the "true" pavement layer moduli. There are two primary sources that affect the inverse procedure on finding the true pavement layer module:

- The simplifications of the FE models on pavement sections: the 2-D axisymmetric assumptions on the pavement geometry, the assumptions of linear elastic material behavior, and the static loading condition assumption do not fully simulate the actual pavement sections and their behaviors.
- The instrumentation measurements used in the inverse procedure: instrumentation measurements on local spots do not necessary accurately represent the pavement responses due to the measurements errors caused by electrical noise, installation etc.

7.5 Results and Discussion

LWD tests were carried out on the pavement sections with the progress of the pavement construction stages. LWD tests were conducted on the base course upon the completion of the base layer. The LWD tests were also conducted on the asphalt surface. The measurements during the two sets of LWD tests on base layer and asphalt concrete layer were used to backcalculate the pavement layer properties separately through the inverse analysis procedure.

Listed in Table 28 are the results from the inverse analysis on pavement layer properties. It is noticed that the elastic moduli values for base layer and subgrade are different between the two sets' analyses. The base layer and subgrade exhibited higher stiffness resulted from the inverse analysis based on the LWD tests on the asphalt layer. This indicates that the addition of the asphalt layer may have changed the confining conditions of the unbound layers and consequently increased the moduli of the unbound base and subgrade layer. Nevertheless, in looking at the results of the three-layer system, the backcalculated layer moduli values appear to be reasonable.

Table 28. Results of inverse analysis using instrumentation measurements

Runs	**FE Models**	**Measured Pavement Response**	**Backcalculated Pavement Layer Moduli (MPa)**
3	unreinforced two- layer section in ***Instrumented APT I***; LWD peak stress: 64.6 kPa	base deflection: 1.98 mm subgrade deflection: 1.66 mm	Base: 14.3 Subgrade: 4.8
4	unreinforced three-layer section in ***Instrumented APT I***; LWD peak stress: 129.6 kPa	asphalt deflection: 0.82 mm subgrade deflection: 0.59 mm subgrade vertical stress: 12.6 kPa	AC: 1684.0 Base: 43.5 Subgrade:12.2
5	unreinforced three-layer section in ***Instrumented APT II***; LWD peak stress: 130.0 kPa	asphalt deflection: 1.04 mm subgrade deflection: 0.80 mm subgrade vertical stress: 11.2 kPa	AC: 1705.1 Base: 27.8 Subgrade: 9.0

Using the measurements from pavement instruments and LWD sensors during the LWD tests, an inverse procedure was adopted to backcalculate the pavement layer properties. A well-recognized optimization algorithm, CMAES, was incorporated into the inverse procedure to search for the pavement layer moduli values that can generate the pavement responses most similar to the measured corresponding responses. The inverse procedure and the optimization algorithm showed good accuracy in finding the pavement layer moduli through the examination tests using synthetic data. Reasonable results were obtained for the pavement layer moduli from the inverse procedure.

8 SUBGRADE PERMANENT DEFORMATION MODELS FOR GEOGRID-REINFORCED FLEXIBLE PAVEMENTS

Pavement sections in both of the two sets of accelerated testing were built on subgrade soil with moisture content beyond the optimal values to mimic a weak subgrade. The inclusion of the geogrid reinforcements at the base-subgrade interface was primarily aimed at stabilizing weak subgrade in this study. The subgrade permanent deformation was expected to be reduced due to the geogrid reinforcement. This chapter presents the procedures of modifying and calibrating the subgrade permanent deformation model adopted in MEPDG. Measurements from the Instrumented APT I were used for the calibration while the calibrated models were verified by measurements from the second set of tests, Instrumented APT II.

The total permanent deformation in a pavement structure is the summation of permanent deformation in each individual layer. Therefore, the total rutting equals the rutting in asphalt concrete layer, base course layer, and subgrade:

$$\Delta_{total} = \delta_{AC} + \delta_{base} + \delta_{subgrade} \quad (26)$$

In this study, the total rutting (Δ_{total}) and subgrade permanent deformation ($\delta_{subgrade}$) were measured at intervals of axle load applications. No measurements were taken for deformation in asphalt layer and base layer (δ_{AC}, δ_{base}). Therefore, permanent deformation models for base course layer and asphalt concrete layer were not considered in this study due to the lack of measurements, although the inclusion of geogrids could be influential to the permanent deformation characters of the layers lying above, particularly the base course layer. Furthermore, the calibration of subgrade permanent deformation models was limited by the number of tests, subgrade conditions, geogrid types, pavement materials and structural thickness.

8.1 Modifications of Subgrade Permanent Deformation Models in MEPDG

The *Mechanistic-Empirical Pavement Design Guide* uses one permanent deformation model with different sets of calibration factors for pavement unbound layers, including aggregate base, subbase, and soil subgrade (NCHRP, 2002). For an unbound pavement layer or sublayer, the permanent deformation of the layer or sublayer can be calculated by the following model:

$$\delta_p = \beta_{cal} \left(\frac{\varepsilon_0}{\varepsilon_r} \right) e^{-\left(\frac{\rho}{N}\right)^{\beta}} \varepsilon_v h \qquad (27)$$

where: δ_p = permanent deformation

ε_r = resilient strain imposed in laboratory test, typically triaxial tests

ε_v = average vertical resilient strain in the layer

ε_0, β, ρ = material parameters

N = number of load applications

h = layer thickness

Knowing that the resilient strain (ε_r) imposed in triaxial tests is not available in this study, this parameter can be combined with the other two parameters (β_{cal} and ε_r) into one calibration factor, β_{cal}. Therefore, the equation for calculating the plastic strains in an unbound layer or sublayer can be rewritten as follows:

$$\delta_p = \beta_{cal} e^{-\left(\frac{\rho}{N}\right)^{\beta}} \varepsilon_v h \qquad (28)$$

β_{cal} is merely a calibration factor and may not represent any physical meaning. One of the parameters, β is a function of water content:

$$\log \beta = -0.61119 - 0.017638\, W_c \qquad (29)$$

where W_c is the water content in the layer (%)

The other parameter (ρ) is a function of the resilient modulus and water content of the unbound layer or sublayer:

$$\rho = 10^9 \left[\frac{C_0}{\left(-(10^9)^{\beta}\right)} \right]^{\frac{1}{\beta}} \tag{30}$$

in which C_0 is expressed as follows:

$$C_0 = \ln\left[\frac{\left(a_1 E_r^{b_1}\right)}{\left(a_9 E_r^{b_9}\right)} \right] \tag{31}$$

The constants a_1, b_1, a_9, b_9 are given as 0.15, 0.0, 20.0, and 0.0 in the MEPDG, which leads to the independency of parameter (ρ) on the resilient modulus because of the zero values for b_1 and b_9. In order to account for the effects of stiffness of the unbound layer, besides the vertical resilient strains, the two constants (b_1 and b_9) were recalibrated in this study.

In summary, in order to estimate the subgrade permanent deformation using Equation 28, one would need the following inputs and calibration factors:

- Material properties: water content (W_c), elastic modulus E_r
- Thickness of the layer or sublayer: h
- Outputs from the response model: vertical elastic strain (ε_r) at the mid-depth of the layer or sublayer
- Parameters associated with the layer stiffness: b_1 and b_9
- Calibration factors: β_{cal}

Instead of estimating the subgrade permanent deformation by dividing the usually deep subgrade into large amount of sublayers, an empirical model was adopted to reduce the calculation efforts (NCHRP, 2002). The model correlate the plastic strain at any depth of the subgrade with the plastic strain at the top of the subgrade:

$$\varepsilon_p(z) = (\varepsilon_{p,\,z=0})\, e^{-kz} \tag{32}$$

in which: $\varepsilon_p(z)$ is the plastic vertical strain at depth of z measured from the top of the subgrade.

$\varepsilon_{p,\,z=0}$ is the plastic vertical strain at the top of the subgrade

z is the depth measured from the top of the subgrade

k is a constant

The total permanent deformation of subgrade would be the integration of the plastic vertical strain, $\varepsilon_p(z)$ with the thickness of the subgrade of the depth from the top of subgrade to bedrock, $h_{bedrock}$. In order to solve for the constant k, plastic strains at two different depths (z=0 and z = 152.4 mm / 6 inches) of the subgrade are first estimated using following:

$$\varepsilon_p = \beta_{\text{cal}}\, e^{-(\frac{\rho}{N})^{\beta}}\, \varepsilon_v \tag{33}$$

The values of plastic strains at the two different depths are then substituted into Equitation (31) to solve for the constant k:

$$k = \frac{1}{152.4}\left(\frac{\varepsilon_{p,z=0}}{\varepsilon_{p,z=152.4}}\right) \tag{34}$$

Knowing that the plastic deformation in the subgrade is:

$$d\delta = \varepsilon_p(z)\, dz \tag{35}$$

The total permanent deformation in the subgrade is expressed as below:

$$\delta = \int_0^{h_{bedrock}} \varepsilon_p(z)dz = (\varepsilon_{p,\,z=0}) \int_0^{h_{bedrock}} e^{-kz}\, dz = (\frac{1-e^{-kh_{bedrock}}}{k})\varepsilon_{p,z=0} \tag{36}$$

8.2 Calibration of the Subgrade Permanent Deformation Model

Following the procedures discussed above, the vertical strains at the top of subgrade and at the depth of 152.4 mm (6 in) of subgrade was extracted from the FE model calibrated based on the LWD measurements. The calculated total permanent deformation along with the number of traffic load was compared against the measured permanent deformation using LVDT. The root mean squared error (RMSE) was set as the objective function to be minimized:

$$\Phi = \sqrt{\frac{\sum_{i=1}^{N}(\Delta_{mi} - \Delta_{ci})^2}{(N-1)}} \tag{37}$$

where N is the number of measurements

Δ_{mi} is the i^{th} measured total subgrade deformation

Δ_{mi} is the i^{th} calculated total subgrade deformation

The water content in percentage was expected to be a known material property input into the permanent deformation model for the unbound pavement layers. However, in this study, the water content was not continuously monitored through the accelerated testing. Only the initial water content and the water content at the end of the tests were tested. Therefore, the water content was set as an unknown and subjected to constraints of a certain range for each section. Furthermore, according to the testing time period listed in Table 19, the water content in section with Grid A is expected to be the highest during the accelerated testing, followed by sections in the order of control section, Grid B, and Grid C. This relationship of water content among the four sections was incorporated as a constraint into the optimization procedure to solve for the water content.

Both the water content and calibration factors for each section were solved through an optimization procedure. The same optimization algorithm described in Section 7.3.2 was used. Through the optimization procedure in conjunction with the constraints discussed above, the water content for the four sections, Grid A, Grid B, Grid C and control were determined as: 24.2%, 23.0%, 22.5%, and 23.6%.

Instead of using one set of calibration factors for all the reinforced sections, the sections reinforced with various geogrids were calibrated separately to closely reflect their different permanent deformation characters. Table 29 provides a summary of the calibration factors for the reinforced and unreinforced sections in the Instrumented APT I.

Table 29. Calibrated factors in subgrade permanent deformation model for sections in Instrumented APT I

Calibration Factors	Grid A	Grid B	Grid C	Control
β_{cal}	507.25	153.63	275.60	298.97
b1	0.48	0.77	0.40	1.98
b9	0.53	0.61	0.50	1.87

Figure 45-a presents the measured and modeled subgrade permanent deformation evolution with the number of axle load applications. The modeled subgrade permanent deformation indicates that the geogrids reduced the subgrade deformation to different degrees in the order of: Grid C, Grid B, and Grid A. As can be seen in Figure 45-a, in terms of decreasing subgrade permanent deformation, only marginal improvement was observed for the section reinforced by Grid A while Grid B and Grid C exhibited considerable improvements in reducing subgrade permanent deformation.

8.3 Verification of Permanent Deformation Models

As mentioned earlier, the subgrade permanent deformation models modified from the model in MEPDG are subjected to limitations such as the small number of testing samples, special loading conditions using MMLS3, and limited types of soil. Nevertheless, the subgrade permanent deformation model calibrated using measurements from the Instrumented APT I were verified by measurements from the Instrumented APT II.

Following the same procedures described in section 8.1, the calibration factors listed in Table 29 were used to calculate the permanent deformation of subgrade for pavement sections in the Instrumented APT II. Figure 45-b presents the measured and predicted subgrade permanent deformation along with the axle load repetitions.

Overall, the model underestimated the subgrade permanent deformation, although the model can distinguish the difference in performance among the sections (i.e., the predicted rank of the performance was consistent with the measurements). It should be noted that the effects of geogrids were incorporated into the model by means of vertical resilient strains, which were extracted from the finite element response model. In addition, the calibration factors, even without physical meaning, may also account for the geogrid reinforcement effects when they were calibrated to measurements.

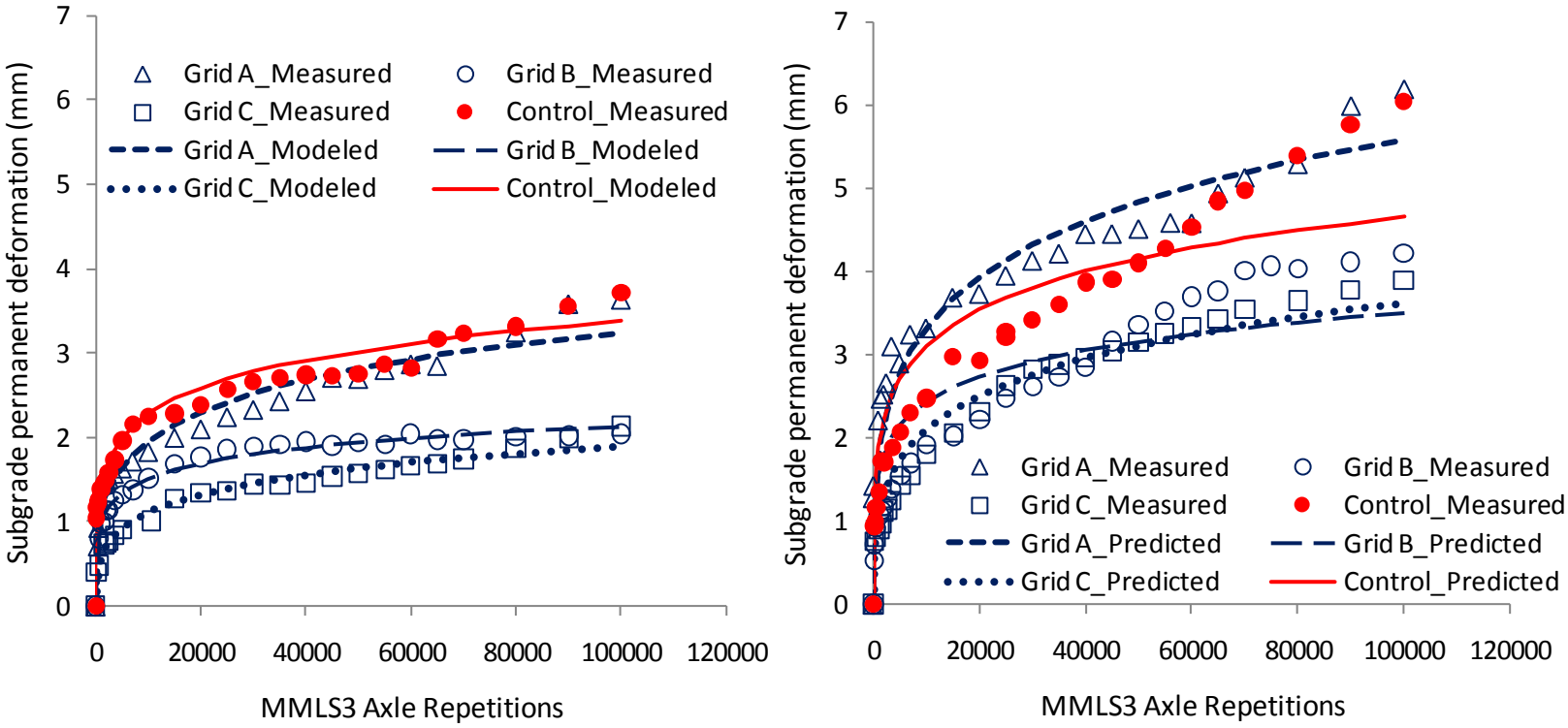

Figure 45. Subgrade permanent deformation: (a) Measured and modeled for sections in Instrumented APT I; (b) Measured and predicted for sections in Instrumented APT II

9 CONCLUSIONS AND RECOMMENDATIONS

This chapter provides a summary of the research project, whose aim was to investigate the structural benefits of using geogrids in reinforcing flexible pavements built on weak subgrade. Major findings through the study are presented in this chapter. Recommendations based on the outcome of the study were made for the practices of using geogrids in pavements.

9.1 Summary and Conclusions

Three PennDOT-approved geogrid products (Grid A, Grid B, and Grid C) were subjected to an in-depth investigation through multi-scale tests: in-air index testing, bench-scale testing, and pit-scale accelerated pavement testing. Geogrids' basic geometric characters and mechanical properties, particularly tensile behaviors at small displacements, were tested in air, followed by bench-scale testing, namely pullout and direct shear tests with geogrids embedded in pavement materials to characterize the geogrid-pavement interfaces.

The three geogrids were further tested within scaled pavement sections constructed in a pit with reinforced concrete walls. Two types of loads were applied to the scaled pavement sections: non-destructive LWD load and the MMLS3 trafficking load. Various instruments were installed in the scaled pavement to monitor pavement responses to the LWD and MMLS3 axle loads. Both elastic and permanent deformations at the top of the subgrade were measured under the LWD load and at intervals of the MMLS3 load repetitions. Vertical stress on top of the subgrade was also monitored. A contact-type profilometer was used to measure the surface rutting / total permanent deformation of the pavement sections at different stages of MMLS3 load applications. In addition to the measurements of the pavement responses, the geogrids were instrumented with foil strain gages to measure strains developed in the geogrids during the accelerated testing.

The in-air tensile tests yielded the tensile modulus at small-displacements which was expected to be the magnitude of stretch experienced by geogrids in the accelerated testing. Grid B showed higher tensile modulus than Grid A and Grid C under the small-

displacement testing conditions. Similarly, the interface properties were also estimated at conditions of small displacement, whereas Grid B had the highest interface shear modulus followed by Grid A and Grid C.

Two sets of accelerated testing (Instrumented APT I and Instrumented APT II) were carried out on pavement sections built on two different types of soil. Measurements of the total rutting on pavement surface at intervals of MMLS3 axle repetitions showed that the control section did not necessarily have the greatest rutting. While there were many factors such as change in water content in the subgrade, change in temperature in the asphalt concrete, and inconsistency in construction that affected the test results, the variation in asphalt concrete air voids could be the most influential and was therefore investigated. The surface total rutting was then normalized to a value of percent air void reduction to mitigate the effects of variation in air void. It was not conclusive whether Grid A is effective in reinforcing weak pavement subgrade based on only two replicates of testing. Caution should be taken when using Grid A in pavements under similar conditions to those in this study.

Through the two sets of accelerated testing, Grid B and Grid C consistently showed improvements in the pavement performance in resisting permanent deformation. Both the normalized surface total rutting and measured subgrade permanent deformation demonstrated the effectiveness of including Grid B and Grid C in reinforcing weak pavement subgrade and the consequent reduction in deformation. However, Grid A exhibited controversial permanent deformation behaviors between the two sets of the accelerated testing. In Instrumented APT I, Grid A showed slightly less total rutting and subgrade permanent deformation, while the control section outperformed the section with Grid A in Instrumented APT II.

Finite element (FE) response models were created for the reinforced and unreinforced pavement sections. Linear static analysis was conducted. The base-geogrid-subgrade interface was simulated in the FE model with the incorporation of results from the bench-scale testing. The FE models were calibrated through an inverse analysis procedure based on the measurement of LWD tests. Elastic compressive strains were extracted from the FE models that are needed in the subsequent development of subgrade permanent deformation models.

In light of the mechanistic-empirical pavement design, attempts were made to develop prediction models for the subgrade permanent deformation. The model adopted in MEPDG for unbound pavement layers' permanent deformation was modified to accommodate the testing conditions in this study. Measurement of subgrade permanent deformation in Instrumented APT I was used to calibrate the model. The model was then verified using the measurements from Instrumented APT II. It was found that the model underestimated the subgrade permanent deformation to various degrees, although the model was able to predict the rank of the performance among the sections. Knowing that a variety of factors such as the stress state of the subgrade, subgrade soil characters (soil type, density, fines content, etc.), and moisture content affect the permanent deformation behaviors, it is recognized that the model was limited by the number of testing samples to account for those factors.

9.2 Recommendations

The following recommendations were made for the practice of using geogrids to reinforce weak pavement subgrade or testing geogrids in laboratories for pavement applications:

1) Geogrids included in pavements typically experience small displacements that are much less than the elongation at failure. Therefore, tensile properties should be tested at small displacements or under expected loading magnitude for geogrids that will be used for pavement applications.
2) Information at the spectrum of small displacements from interface characterization tests should be investigated, although interface tests such as pullout and direct shear usually provide results from tests at failure.
3) Grid A or geogrid with similar properties to Grid A should be used with caution for reinforcing weak subgrade, although it was not confirmed whether Grid A is effective in reinforcing weak subgrade based on the results of this study.

REFERENCES

AASHTO. (1993). *Guide for Design of Pavement Structures*, American Association of State Highway and Transportation Officials (AASHTO).

Abd El Halim, A.O. (1983). *Geogrid Reinforcement of Asphalt Pavements*, Ph.D. Dissertation, University of Waterloo, Ontario, Canada.

Ahlvin, R.G., and Ulery, H.H. (1962). "Tabulated values for determining the complete pattern of stresses, strains and deflections beneath a uniform circular load on a homogeneous half space," *Bulletin 342*, *Highway Research Board*:1-13.

Al-Qadi, I.L, Brandon, T.L., Valentine, R.J., Lacina, B.A., and Smith, T.E. (1994). "Laboratory evaluation of geosynthetic-reinforced pavement sections." *Transportation Research Record 1439*, Transportation Research Board, National Research Council, Washington D.C.: 25-31.

Al-Qadi, Dessouky, S.H., Kwon, J., and Tutumluer, E. (2008). "Geogrid in flexible pavements: validated mechanis," *Transportation Research Record 2045*, Transportation Research Board, National Research Council, Washington D.C.: 102-109.

Aran, S., (2006). "Base reinforcement with biaxial geogrid-long term performance," *Transportation Research Record 1975*, Transportation Research Board, National Research Council, Washington D.C.:115-123.

Asphalt Institute (AI), (1991). Computer Program DAMA (CP-1/1991 Revision) - Pavement Structural Analysis using Multi-Layered Elastic Theory, Lexington, KY.

Austin and Coleman (1993). "A Field Evaluation of Geosynthetic-reinforced Haul Roads over Soft Foundation Soils," *Proceedings of the Conference Geosynthetic*, Vancouver, BC, Vol. 1: 65-80.

Baker, H. B., Buth, M. R., and Van Deusen, D. A. (1994). "Minnesota Road Research Project load response instrumentation installation and testing procedures." Report No. MN/PR-94/01, Minnesota Department of Transportation, 395 John Ireland Boulevard, St. Paul, MN 55155

Bakis, C. E. (2009). Personal Communication.

Barksdale, R.D. (1972). "Laboratory evaluation of rutting in base course materials," Proceedings of 3rd International Conference on Structure Design of Asphalt Pavements: 161-174.

Barksdale, R.D., Brown, S.F., and Chan, F. (1989). "Potential Benefits of Geosynthetics

in Flexible Pavement Systems." *National Cooperative Highway Research Program (NCHRP) Report No.315*, Transportation Research Board, National Research Council, Washington D.C.

Bergado, D.T. and Jin-Chun Chai. (1994). "Pullout force/displacement relationship of extensible grid reinforcements," *Geotextile and Geomembrane*. Vol.13: 295-316.

Berg, R. R., Christopher, B. R., and Perkins, S. (2000). "Geosynthetic Reinforcement of the Aggregate Base/Subbase Courses of Pavement Structures," *Geosynthetic Materials Association White Paper II,* Geosynthetic Materials Association, Roseville, Minnesota.

Brandon, T.L., Al-Qadi, I.L., Lacina, B.A., and Bhutta, S.A. (1996). "Construction and instrumentation of geosynthetically stabilized secondary road test sections." *Transportation Research Record 1534*, Transportation Research Board, Washington D.C.: 50-57.

Brown, S.F., Brodrick, B.V., and Hughes, D.A.B. (1984). "*Tensar reinforcement of asphalt:laboratory studies*." Proceedings of the Conference on Polymer Grid Reinforcement in Civil Engineering, Thomas Telford Publishing, London:158-165.

Brown, S.F., and Pappin, J.W. (1981). "Analysis of pavements with granular bases," *Transportation Research Record 810*, Transportation Research Board, Washington D.C.: 17-23.

Burmister, D.M. (1943). "The theory of stresses and displacements in layered systems and applications to the design of airport runways." *Proceedings of Highway Research Board*, Vol.23: 126-144.

Burmister, D.M. (1945). "The general theory of stresses and displacements in layered soil systems," *Journal of Applied Physics*, Vol.16: 84-94, 126-127, 296-302.

Carroll, R.G., Jr., Walls, J.G., and Haas, R., (1987). "Granular base reinforcement of flexible pavements using geogrids," *Proceedings of Geosynthetics*, St. Paul, MN: IFAI: 46-57.

Chehab, G.R., Palomino, A.M., and Tang, X. (2007). Laboratory evaluation and specification development for geogrids for highway engineering applications, *Report No. FHWA-PA-2007-009-050110*, Pennsylvania Department of Transportation, Harrisburg, PA, USA.

Chen, D.H., and Hugo, F. (1998). "Full-scale accelerated pavement testing of Texas Mobile Load Simulator." Journal of Transportation Engineering, Vol.124 (5): 479-490.

Cuelho, E.V., S.W. Perkins, and S.K. Ganeshan. (2005). "Determining geosynthetic

material properties pertinent to reinforced pavement design," *Advances in Pavement Engineering (GSP-130) – Proceedings of the Sessions of the Geo-Frontiers 2005 Congress*, January 24-26, Austin, Texas, USA.

Cox, B.R., McCartney, J.S., Wood, C.M., Curry, B. (2010). "Performance evaluation of full-scale geosynthetic-reinforced flexible pavements using field cyclic plate load tests," TRB 2010 Annual Meeting CD-ROM, Transportation Research Board, Washington, D.C.

De Jong, D. L., Peatz, M. G. F. and Korswagen, A. R. (1972). Computer program BISAR: Layered systems under normal and tangential loads, Koninklijke Shell–Laboratorium, Amsterdam, External Report AMSR.0006.73.

Fleming, P.R., Frost, M.W., Lambert, J.P.(2007). "A review of the lightweight deflectometer (LWD) for routine insitu assessment of pavement material stiffness." *TRB 2007 Annual Meeting CD-ROM*, Transportation Research Board, Washington, D.C.

Foster, C.R., and Ahlvin, R.G. (1954). "Stresses and deflections induced by a uniform circular load," *Proceedings of Highway Research Board*, Vol.33: 467-470.

Hugo, F., Fults, K., Chen, D.H., and Smit, AdeF, (1999). "An overview of the TxMLS program and lessons learned." *1st International Conference on Accelerated Pavement Testing*. Reno, Nevada, USA, Oct. 18-20, 1999.

General Accounting Office (GAO). (1997). *Transportation Infrastructure: Highway Pavement Design Guide is Outdated*, Report GAO/RCED-98-9, U.S. General Accounting Office, November 1997.

Gilchrist, A.J.T., Austin, R.A., and Brodrick, B.V. (1996). "The development of a grid/geotextile composite for bituminous pavement reinforcement." *Proceedings of the Third International RILEM Conference on Reflective Cracking in Pavements, Design and Performance of Overlay Systems*, Maastricht, Netherlands: 288-297.

Gillespie, T.D., Karimihas, S.M., and Cebon, D. (1993). *NCHRP Preport 353: Effects of Heavy-Vehicle Characteristics on Pavement Response and Performance*, Transportation Research Board, Washington, D.C.

Gopalakrishnan, K., and Manik, A. (2010). "Co-variance matrix adaptation evolution strategy for pavement backcalculation." *Construction and Building Materials*, Vol. 24 (11): 2177-2187.

Haas, R. (1984). "Structural behaviour of Tensar reinforced pavements and some field applications." *Proceedings of the Conference on Polymer Grid Reinforcement in Civil Engineering*, Thomas Telford Publishing, London: 166-170.

Haas R., Wall, J., and Carroll, R.G.(1988). "Geogrid reinforcement of granular bases in flexible pavements." *Transportation Research Record 1188*, Transportation Research Board, National Research Council, Washington D.C.:19-27.

Halim, A.O.A., and Razaqpur, A.G. (1993). "Minimization of reflection cracking through the use of geogrid and better compaction." *Proceedings of the Second International RILEM Conference on Reflective Cracking in Pavements*, Liege, Belgium: 299-306.

Hansen, N. (2006). "The CMA Evolution Strategy: A Comparing Review." *Towards a New Evolutionary Computation. Advances in Estimation of Distribution Algorithms*, J.A. Lozano, P. Larrañga, I. Inza and E. Bengoetxea (eds.). pp. 75-102, Springer

Hansen, N. (2010). Personal Communication.

Harichandran, R.S., Yeh, M.S., and Baladi, G.Y. (1990). "MICH-PAVE: a nonlinear finite element program for analysis of pavements," *Transportation Research Record 1286*, Transportation Research Board, National Research Council, Washington D.C.:123-131.

Harvey, J.T., Roesler, J, Coetzee, N.F., and Monismith, C.L. (2000). "Caltrans accelerated pavement test (CAL/APT) program - summary report, six year period: 1994-2000." *Report No. FHWA/CA/RM-2000/15*, Pavement Research Center, Institute of Transportation Studies, University of California, Berkeley, CA

Henry, K., Clapp, J., Davids, W., Humphrey, D., and Barna, L. (2009). "Structural improvements of flexible pavements using geosynthetics for base course reinforcement," *Report No. ERDC/CRREL TR-09-11*, U.S. Army Corps of Engineers in conjunction with U.S. Department of Transportation, Pooled Fund Program, Federal Highway Administration, McLean, VA.

Hicks, R.G., and Monismith, C.L. (1971). "Factors influencing the resilient response of granular materials," *Highway Research Record 345*, Washington, D.C.: 15-31.

HRB. (1961). *The AASHO Road Test History and Description of Project*. Highway Research Board, Washington, DC.

Huang, Y.H. (2003). *Pavement Analysis and Design*, Pearson Prentice Hall, Upper Saddle River, NJ, USA.

Hugo, F., and Martin, A. E. (2004). "Significant findings from full-scale accelerated pavement testing." *NCHRP Synthesis of Highway Practice No. 325*, TRB, National Research Council, Washington D.C.

Jewell, R.A., Milligan, G.W.E., Sarsby, R.W., and Dubois, D. (1984). "Interaction between soil and geogrids." *Proceedings of the Conference on Polymer Grid Reinforcement in Civil Engineering*, Thomas Telford Publishing, London: 18-30.

Juran, I., Knochenmus, G., Acar, Y.B., and Arman, A. (1988). "Pull-out response of

geotextiles and geogrids (Synthesis of available Experimental Data)." *Proceedings of Symposium on Geotextiles for Soil Improvemen*t, ASCE, GSP No.18, ASCE, Reston, VA: 92-111.

Kim, S.M., Hugo, F., and Roesset, J.M. (1997). "Small-scale accelerated pavement testing." *Journal of Transportation Engineering*, Vol.124(2): 117-122.

Kim, M. (2007). *Three-Dimensional Finite Element Analysis of Flexible Pavements Considering Nonlinear Pavement Foundation Behavior*, Ph.D. Dissertation, University of Illinois at Urbana-Champaign, IL.

Kinney, T.C., Xiaolin, Y., (1995). "Geogrid aperture rigidity by in-plane rotation." *Proceedings of the Conference Geosynthetics 95*, Nashville, TN, USA, Vol.2: 525-538.

Kinney, T.C., Abbott, J, and Schuler, J. (1998). "Benefits of using geogrids for base reinforcement with regard to rutting." *Transportation Research Record 1611*, Transportation Research Board, National Research Council, Washington D.C.:86-96.

Koerner, R.M. (1998). *Designing with Geosynthetics*, 4th Edition, Prentice Hall, New Jersey.

Kooperman, S., Tiller, G., and Tseng, M. (1986). ELSYM5 "Interactive microcomputer version, user's manual," Report FHWA-TS-7-206, Federal Highway Administration, Washington D.C.

Kwon, J. (2007). *Development of a Mechanistic Model for Geogrid Reinforced Flexible Pavements*, Ph.D. Dissertation, University of Illinois at Urbana-Champaign, Urbana, IL.

Lazebnik, G.E. (1998). *Monitoring of Soil-Structure Interaction: Instruments for Measuring Soi Pressures*. Trans. Gregory P. Tsinker. Chapman and Hall, New York.

Lekarp,F., and Dawson, A. (1998). "Modeling permanent deformation behavior of unbound granular materials," *Construction and Building Materials*, Vol.12 (1):9-18.

Lekarp, F., Isacsson, U., and Dawson, A. (2000). "State of the art II: Permanent strain response of unbound aggregates," *Journal of Transportation Engineering*, Vol.126 (1): 76-83.

Leng, J., Ju, T.J., and Gabr, M.A., (2002). "Characteristics of geogrid-reinforced aggregate under cyclic load," *Transportation Research Record 1786*, Transportation Research Board, National Research Council, Washington D.C.:29-35.

Leng, J., and Gabr, M. (2005). "Numerical analysis of stress-deformation response in reinforced unpaved road sections." *Geosynthetics International*, Vol.12, 111-119.

Liao, Y. (2007). *Viscoelastic FE Modeling of Asphalt Pavements and its Application to U.S. 30 Perpetual Pavement*, Ph.D. Dissertation, Ohio University, Athens, OH.

Love, J.P. (1984). *Model Testing of Geogrids in Unpaved Roads*, Doctoral Dissertation, University of Oxford, Oxford, UK.

Lytton, R.L. (1989). "Backcalculation of pavement layer properties in nondestructive testing of pavements and backcalculation of moduli." *Nondestructive Testing of Pavements and Backcalculation of Moduli*, Vol.2, ASTM STP 1026: 7-38.

Martin, A.E., Walubita, L.F., Hugo, F., and Bangera, N.U. (2003). "Pavement response and rutting for full-scale and scaled APT." *Journal of Transportation Engineering*, Vlo.129 (4): 451-461.

Maxwell, S., Kim, W.H., Edil, T.B., and Benson, C.H. (2005). "Geosynthetics in stabilizing soft subgrade with breaker run." *Report No. 0092-45-15*, Wisconsin Department of Transportation, Madison, WI, USA.

McGown, A., Kupec, J., Heerten, G., and K. von Maubeuge. (2005). "Testing Biaxial Geogrids for Specification and Design Purposes," *Geosynthetics Research and Development in Progress (GRI-18) – Proceedings of the Sessions of the Geo-Frontiers 2005 Congress*, January 24-26, Austin, Texas, USA.

Metcalf, J.B. (1996). "Application of Full-scale Accelerated Pavement Testing." *NCHRP Synthesis of Highway Practice No. 235*, TRB, National Research Council, Washington D.C.

Mohiuddin, A. (2003). Analysis of Laboratory and Field Pull-out Tests of Geosynthetics in Clayer Soils, Thesis, Louisiana State University, Baton Rouge, Louisiana, USA.

Monismith, C.L., Harvey, J.T., Hoover, T.P. (2004). "Ten year perspective on accelerated testing: Caltrans partnered pavement research program." 2nd International Conference on Accelerated Pavement Testing, Minneapolis, MN, September 26-29, 2004.

Monismith, C.L., Ogawa, N., Freeme, C.R. (1975). "A permanent deformation characteristics of subgrade soils due to repeated loading," *Transportation Research Record 537*, Transportation Research Board, National Research Council, Washington D.C.:1-17.

Montanelli, F., Zhao, A., and Rimoldi, P. (1997). "Geosynthetic-reinforced

pavement system: testing and design." *Proceedings of Geosynthetics*, IFAI, Vol.2, Long Beach, California, USA March 1997:619-632.

Mun., S. (2003). *Nonlinear Finite Element Analysis of Pavements and its Application to Performance Evaluation*, Ph.D. Dissertation, North Carolina State University, Raleigh, NC.

Müller-Rochholz, J. and Recker, C. (2000). "Tensile Strength and Clamping of Geogrids," *Grips, Clamps, Clamping Techniques, and Strain Measurement for Testing of Geosynthetics, ASTM STP 1379*, American Society for Testing and Materials, West Conshohocken, PA.

NCHRP, (2002). *Simple Performance Test for Superpave Mix Design: Appendix A – Test Method for Dynamic Modulus of Asphalt Concrete Mixtures for Fatigue Cracking*, Transportation Research Board, National Research Council, Washington D.C.

NCHRP. (2004). Guide for Mechanistic-Empirical Design of New and Rehabilitated Pavement Structures, *Final Report, NCHRP Study 1-37A*, National Cooperative Highway Research Program (NCHRP), Washington D.C.

Newcomb, D. E., Johnson, D.M., Kaker, H.B., and Lund, S.M. (1990). "Minnesota Road Research Project: work plan for research objectives." Report MN-RC-2007-16, Minnesota Department of Transportation, 395 John Ireland Blvd., St.Paul, MN 55155

Pennsylvania Department of Transportation (PennDOT), (1995). *Pavement Policy Manual, Publication 242* , Commonwealth of Pennsylvania Department of Transportation, Harrisburg, PA

Penner, R., Haas, R., Walls, J. and Kennepohl, G. (1985). "Geogrid reinforcement of granular bases." Paper presented at the Roads and Transportation Association of Canada Annual Conference, Vancouver, British Columbia, Canada, September, 1985.

Perkins, S.S. (1999). "Geosynthetic Reinforcement of Flexible Pavements: Laboratory Based Pavement Test Sections." *Report No. FHWA/MT-99-001/8138*, U.S. Department of Transportation, Federal Highway Administration, Washington, D.C.

Perkins, S.S. (2002). "Evaluation of geosynthetic reinforced flexible pavement systems using two pavement test facilities," *Report No. FHWA/MT-02-008/20040*, U.S. Department of Transportation, Federal Highway Administration, Washington, D.C.

Perkins, S. W., Christopher, B.R., and Cuelho, E.L. (2004). *Development of Design Methods for Geosynthetic Reinforced Flexible Pavements*, Report No. DTFH61-01-X-00068, Federal Highway Administration, 400 Seventh Street, S.W. Room 4410, Washington D.C. 20590

Raad, L., and Figueroa, J.L. (1980). "Load response of transportation support systems," *Journal of Transportation Engineering*, Vol.16 (TE1): 111-128.

Saad, B., and Mitri, H., and Poorooshasb, H. (2006). "3D FE analysis of flexible pavement with geosynthetic reinforcement," *Journal of Transportation Engineering*, Vol.132 (5): 402-415.

Schapery, R. A., and Park, S. W. (1999). "Methods of Interconversion between Linear Viscoelastic Materials Functions. Part II – An Approximate Analytical Method," *International Journal of Solids and Structures*, Vol. 36(11):1677–1699.

Seed, H.B., Mitry, F.G., Monismith, C.L., and Chan, C.K. (1967). "Factors influencing the resilient deformation of untreated aggregate base in two layer pavements subjected to repeated loading," *Highway Research Record 190*, Washington, D.C.

Shukla, S.K. (2002). *Geosynthetics and their Applications*, Thomas Telford, London, UK.

Shukla, S.K., and Yin, J. (2006). *Fundamentals of Geosynthetic Engineering*, Taylor and Francis, London, UK.

SIMULIA.(2009). Abaqus Analysis User's Manual, Abaqus version 6.9, Providence, RI

Taciroglu, E. (1998). *Constitutive Modeling of the Resilient Response of Granular Solids*, Ph.D. Dissertation, University of Illinois at Urbana-Champaign, Urbana, IL.

Tang, X., Chehab, G.R., Palomino, A.M, Allen, S., and Sprague J. (2008a). "Effects of geogrids properties on subgrade stabilization of flexible pavements." *Proceedings of GeoCongress 2008: Geosustainability and Geohazard Mitigation*, ASCE, Geotechnical Special Publication 178:1089-1096.

Tang, X., Chehab, G.R., and Palomino, A.M (2008b). "Accelerated testing of geogrid-reinforced subgrade in flexible pavements." *Proceedings of GeoCongress 2008: Geosustainability and Geohazard Mitigation*, ASCE, Geotechnical Special Publication 178:1049-1056.

Tang, X., Palomino, A.M., and Chehab, G.R. (2008c). "Laboratory evaluation of geogrids for flexible pavement reinforcement." *The GeoAmericas 2008Conference Proceedings*, Cancun, Mexico, March 2-5, 2008: 973-982.

Tatlisoz, N., Edil, T.B., and Benson, C.H. (1998). "Interaction between Reinforcing Geosynthetics and Soil-tire Chip Mixtures," *Journal of Geotechnical and Geoenvironmental Engineering*, Vol. 124, No. 11, pp. 1109-1119.

Thornton, J.S., Allen, S.R., and Arnett, S.L. (2000). "Effect of Gripping Technique on Tensile, Tensile Creep and Tensile creep-rupture Results for a High Tenacity Polyester Yarn," *Grips, Clamps, Clamping Techniques, and Strain Measurement*

for Testing of Geosynthetics, ASTM STP 1379, American Society for Testing and Materials, West Conshohocken, PA.

Theyse, H.L. (1997). "Mechanistic empirical modeling of the permanent deformation of unbound pavement layers," *Proceedings of the 8th International Conference on Asphalt Pavements*, Seattle, WA, Agu.10-14.

Timm, D., West, R., and Priest, A. (2006). "Phase II NCAT test track results." NCAT Report 06-05, 277 Technology Parkway, Auburn, AL 36830

Tompkins, D.M., Khazanovich, L., and Johnson, D.M. (2008). "Benefits of the Minnesota Road Research Project." *Transportation Research Record 2087*, Transportation Research Board, National Research Council, Washington D.C.:12-19.

Tseng, K., and Lytton, R. (1989). "Prediction of permanent deformation in flexible pavement materials." *Implication of Aggregates in the Design, Construction, and Performance of Flexible Pavements*, ASTM STP 1016, ASTM: 154-172.

Tutumluer, E. (1995). *Predicting Behavior of Flexible Pavements with Granular Bases*, Ph.D. Dissertation, Georgia Institute of Technology, GA.

Uddin, W. (2003). "Effects of FWD load-time history on dynamic response analysis of \ asphalt pavement," Presented at Pavement Performance Data Analysis Forum in Conjunction with MAIREPAV03, Guimaraes, Portugal.

Uddin, W., and Garza, S. (2002). "In situ material characterization of pavement-subgrade systems using FWD data and validation by 3D-FE simulations," *CD Proceedings, 2002 Airport Technology Conference*, Federal Aviation Administration , Atlantic City, NJ, May 5-8, 2002.

Uddin, W. and Ricalde, L. (2000). "Nonlinear material modeling and dynamic finite element simulation of asphalt pavement," *Fourteenth Engineering Mechanics Conference*, ASCE, Austin, TX.

Uzan, J. (1985). "Characterization of granular material," *Transportation Research Record 1022*, Transportation Research Board, National Research Council, Washington D.C.:52-59.

Uzan, J. (1976). "The influence of the interface condition on the stress distribution in a layered system," *Transportation Research Record 616*, Transportation Research Board, National Research Council, Washington D.C.:71-73.

Vishay, (2005-a). Surface preparation for strain gage bonding, *Application Note B-129-8*, Vishay, Precision Group, Raleigh, NC

Vishay, (2005-b). Strain gage applications with M-Bond AE-10, AE-15 and GA-2 adhesive systems, Precision Group, Raleigh, NC

Vishay, (2007). Strain gage selection: criteria, procedures, recommendations. *Tech Note TN-505-4*, Vishay, Precision Group, Raleigh, NC

Yoder, E.J., and Witczak, M.W. (1975). *Principles of Pavement Design, 2nd Ed.*, John Wiley & Sons, Inc., New York, NY.

Yoo, P., and Al-Qadi, I. (2007). "Effect of transient dynamic loading on flexible pavements," *Transportation Research Record 1990*, Transportation Research Board, National Research Council, Washington D.C.: 129-140

Wartman, J., D. Harmanos, and P. Ibanez. (2005). "Development of a Versatile Device for Measuring the Tensile Properties of Geosynthetics," *Geosynthetics Research and Development in Progress (GRI-18) – Proceedings of the Sessions of the Geo-Frontiers 2005 Congress*, January 24-26, Austin, Texas, USA.

Warren, K., Brooks, J., and Howard, I. (2005). "Survivability of foil strain gages mounted on geosynthetics under full-scale construction loads." *ASCE, Geotechnical Special Publication No.130-142*: 4085-4090.

Warren, H. and Dieckman, W. L. (1963). Numerical computation of stresses and strains in a multiple - layer asphalt pavement system. International Report, Chevron Research Corporation, Richmond, CA.

Wathugala, G. W., and Desai, C. S. (1993) "Constitutive model for cyclic behavior of clays. I: Theory." *Journal of Geotechnical Engineering*, Vol.119 (4): 714–729.

Wathugala, G. W., Huang, B., and Pal, S. (1996). "Numerical simulation of geogrid reinforced flexible pavements." *Transportation Research Record 1534*, Transportation Research Board, National Research Council, Washington, D.C.: 58–65.

Webster, S.L. (1993). Geogrid reinforced base course for flexible pavements for light aircraft, test section construction, behavior under traffic, laboratory tests, and design criteria, *Technique Report GL-93-6*, USAE Waterways Experiment Station, Vicksburg, MS.

Willis, R., Timm, D., West, R. (2009). "Phase III NCAT Test Track Findings." *NCAT Report 09-08*, 277 Technology Parkway, Auburn, AL 36830

Witczak, M.W., and Uzan, J. (1988). *The Universal Airport Pavement Design System: Granular Material Characterization*, University of Maryland, Department of Civil Engineering, MD.

Witczak,M. (2005).http://knowledge.fhwa.dot.gov/cops/hcx.nsf/discussionDisplay?Open&id=74439AE04DC7FD0B85256FEB003E6A1F&Group=NCHRP%201-

37A%20(MechanisticEmpirical)%20Pavement%20Design%20Guide&tab=DISCUSSION#74439AE04DC7FD0B85256FEB003E6A1F (accessed on Jun. 18, 2010).

Zaghloul, S.M., and White, T.D. (1993). "Use of a three-dimensional, dynamic Finite Element program for analysis of flexible pavement," *Transportation Research Record 1388*, TRB, Transportation Research Board, National Research Council, Washington, D., C.: 60-69.

APPENDIX A: INSTRUMENTATION SELECTION AND INSTALLATION

A.1 Instrumentation Selection and Calibration

The understanding of responses of the layered pavement systems to traffic loading helps determine the instrument types needed for the pavement. Vertical stress on the top of the subgrade is an important factor in pavement design, since the function of a pavement is to reduce the vertical stress on the subgrade such that detrimental pavement deformations will not occur. The vertical interface deflection is often considered an indicator of the vertical stress and layer strength in pavement design. Therefore, earth pressure cells were placed at the surface of the subgrade to quantify the vertical stresses. Linear variable differential transformers were used to measure the deflection of subgrade surface, while a contact-type profilometer can be used to measure the pavement surface deformation. Furthermore, electrical resistance strain gages are used to measure developed strains in the geogrids during the trafficking.

A.1.1 Subgrade Deformation Measurements

Table A.1 lists the previous techniques that have been used for measuring pavement layer deformation. It is noted that LVDTs were selected in most of the past studies. In order to minimize the risk of losing meaningful measurements, an in-depth search for reliable instruments was carried out and many relevant manufacturers or technical support sources were consulted.

Table A.2 presents the potential options for measuring pavement layer deformation. After reviewing the past research and exhausting possible options for measuring pavement layer deformation, it was decided that LVDTs would be used to measure the subgrade deformation and potentiometers were used as a backup measurement.

Table A.1. Techniques used for measuring pavement layer displacement from the past research

Sensor	**Manufacturer and Model**	**Specifications**	**Application**	**Reference**
Multi-Depth Deflectometer (MDD)	N/A	N/A	***TxMLS*** Deflections at various depths	(Chen and Hugo, 1998)
LVDT	Schaevitz GPD 121-500	Range: ±0.5 in Harsh industrial environments; submersible	***Ohio SHRP Test Pavement*** Vertical deflection in subgrade and base	(Sargand and Hazen, 1999)
LVDT	Schaevitz HCD-500 DT	Range: ±0.5 in Harsh industrial environments; submersible	***MnRoad*** Surface layer displacement	MnDOT
MDD	N/A	N/A	***HVS at UC Berkeley*** Deflections at various depths	(Harvey et al., 2000)
μ soil strain system	CRREL	N/A	***HVS at USACE CRREL*** Triaxial dynamic and permanent deformation in the base and subgrade	(Janoo et al., 2003)
Compression Gage (Extensometer)	CTL Group	Range: 1 in Gage length: 6 in	***NCAT*** Vertical deformation in base layer	(Timm et al., 2004)
Vibrating Wire Strain Gage	Geokon Model VCE-4200	Range: 3000 με Gage length: 6 in	***Virginia Smart Road*** Strains in subgrade and cement-stabilized base layer	(Al-Qadi et al., 2004)
LVDT	Macro Sensors, GHSER 750-1000, GHSE 750-1000	Range: 1 in	***ATREL at UIUC*** Vertical deflection in subgrade; vertical and horizontal deflection in base	(Al-Qadi et al., 2006)
LVDT	Macro Sensors, GHSER 750-1000-006, GHSE 750-1000-006	Range: 25.4 mm	***Airport of Cagliari-Elmas in Italy*** Vertical deflection in subgrade; vertical, transverse and longitudinal deflections in base layer	(Al-Qadi et al., 2010)

Table A.2. Potential instruments for measuring subgrade deformation

Sensor	Manufacturer	Model	Limitations
LVDT	Macro Sensors	GHSE-750-1000	• Not enough resistance to harsh environment • Need to be modified for the application
Displacement Transducer	Geokon	Model 4450	• Vibrating wire type transducer with frequency as the output signal • Typically used for long-term static displacement measurement
Compression Gage	CTL Group	N/A	• Measures the average strain within the gage length
Multi-Depth Deflectometer (MDD)	Dynatest, CTL Group	N/A	• Too much disturbance for the application due to the size of MDD
Vibrating Wire Strain Gage	Geokon	Model 3900	• Typically used for concrete structures and earth fills • The range (5,000 με with 203-mm gage length) is not enough for the subgrade deformation • Frequency as the output signal
	Soil Instruments Ltd	ST4-1	• Typically used in concrete elements • The range (3,000 micro strain with 150-mm gage length) is not enough
Vibrating Wire Settlement Cell	Soil Instruments Ltd	S8-1.11T	• Typical applications include the measurement of settlement in embankments, earth and rockfill dams • Too much disturbance due to the size (4.5 in × 15 in)
Vibrating Wire Soil Extensometer	Soil Instruments Ltd	E7-1.10	• Measures strains and settlements of embankments and dams, foundation movements and subsidence • Length 1,000 mm, body diameter 50 mm, flange diameter 150 mm
Single Point Mechanical Rod Extensometers	Geokon	Model A-1	• Used for boreholes • The size (up to 10 m long) is too big for this application

A DC LVDT (Macro Sensors GHSE-750-1000) was selected for measuring the deflection at subgrade surface. It requires a 15-V DC power supply. The maximum travel distance of the push rod is 25.4 mm (1 in). The overall length of the LVDT is 29 cm (11.4 in). The linearity error of the LVDT is less than 0.06% and the repeatability error is less than 0.6 μm.

Depending on the quality of the LVDT and the signal conditioner, the calibration equations for an LVDT can range from highly linear to nonlinear. An LVDT usually exhibits non-linear behavior when the core is displaced near the ends of the LVDT due to the nature of the magnetic field. A customized setup including a micrometer (Figure A.1-a) was used to calibrate the LVDT. The LVDT was calibrated by relating its output voltages to known input displacements with the micrometer. A calibration equation was then obtained and entered into the data acquisition program. Figure A.1-b shows the calibration setup and results.

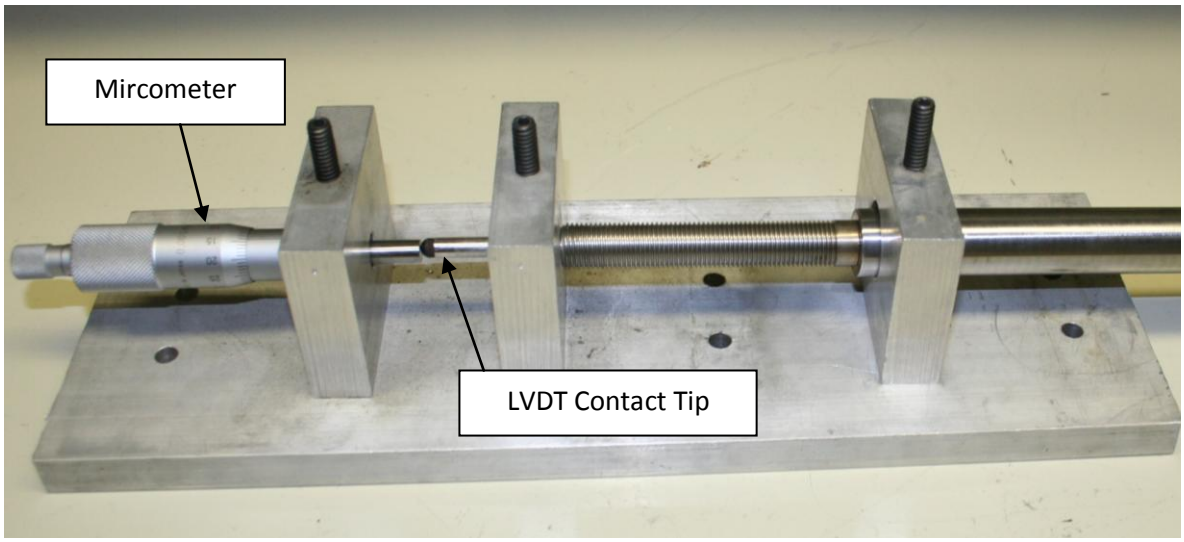

(a)

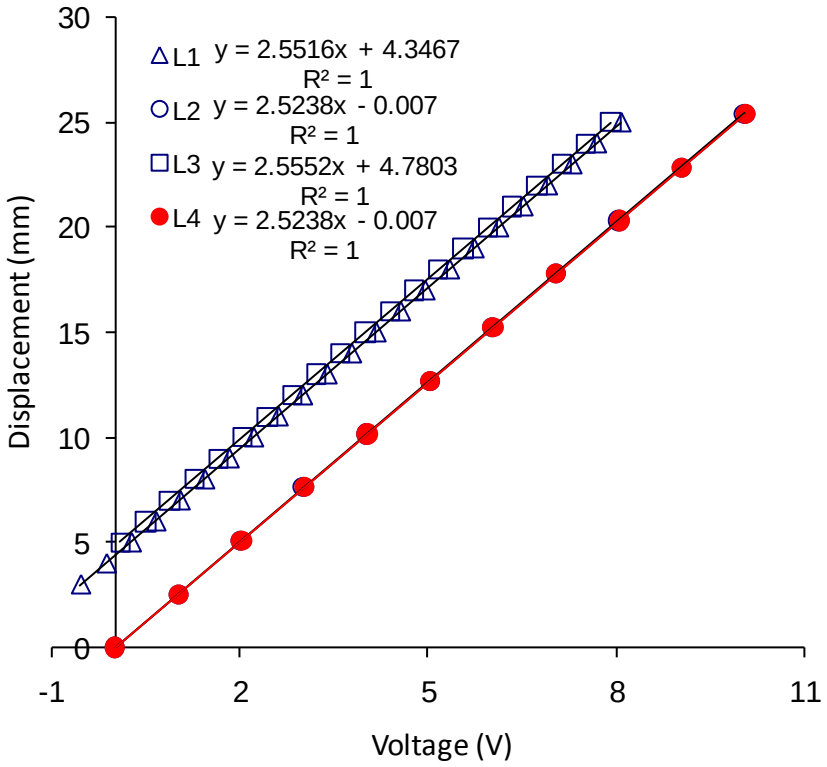

(b)

Figure A.1. Calibration of the LVDT: (a) calibration setup; (b) calibration curve

The relatively less expensive potentiometers were used as backup to the LVDTs for subgrade deformation measurement. The potentiometers (Honeywell MLT-38000201) were customized to measure the strain at the top of the subgrade of each section. The potentiometer has a small diameter of 0.95 cm (3/8 in) and maximum travel distance of 25.4 mm (1 in). Two end plates with diameters of 5 cm were attached onto the potentiometer (Figure A.2). The customized potentiometers were installed and floated at the top of the subgrade without fixing one end of the potentiometer. The potentiometer measures relative distance between the two circular plates.

(a) (b)

Figure A.2. Modification to the potentiometer: (a) original potentiometer; (b) modified potentiometer

Using the same calibration setup as for LVDTs, the potentiometers were calibrated before they were modified. Figure A.3 shows the results of potentiometer calibration.

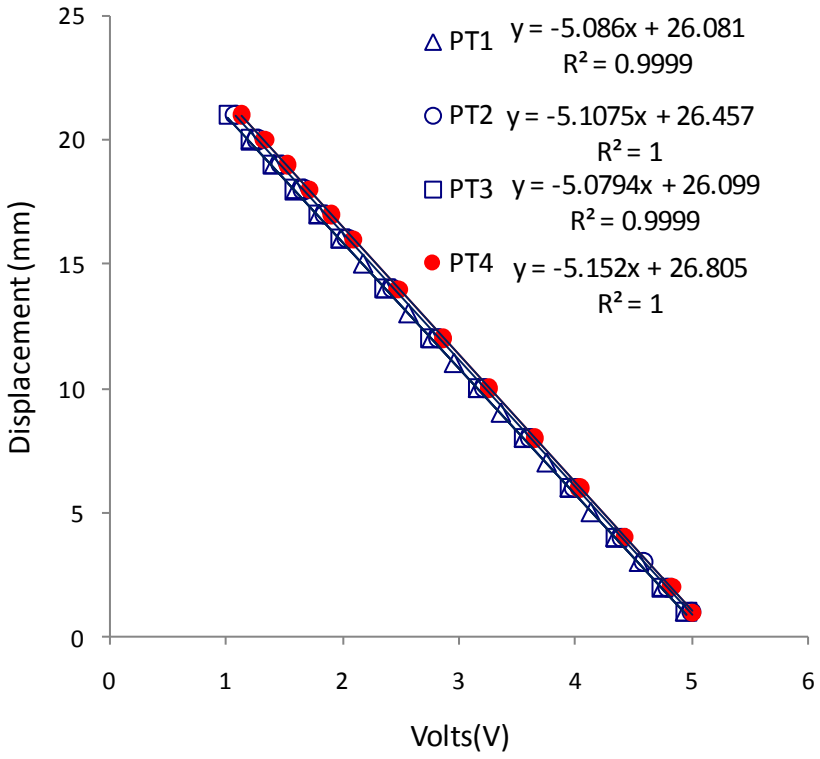

Figure A.3. Results of potentiometer calibration

A.1.2 Subgrade Vertical Stress Measurements

A hydraulic-type pressure cell (Geokon 3500) was selected since it has been successfully used in other pavement experiments. The pressure cell was customized to 10-cm (4-in) diameter by the manufacturer in order to fit the 80-mm (3-in) wide wheel path. The pressure cell has a full-scale range of 250 kPa (36.3 psi), which can provide satisfying resolution and range since the pressure was expected to be about 20 kPa (3 psi) in this application. The scale factor of the pressure cell is 50 kPa/V (7.252 psi/V) according to the specifications provided by the manufacturer. The pressure cell has the following specifications: ± 0.5% calibrated accuracy, < 0.05% thermal effect on zero, < 0.5% linearity, and -20 °C to + 80 °C operating temperature range.

Ideally, soil pressure cells are calibrated in the following sequence (Lazebnik, 1998):

1) A pressure cell is first calibrated in the calibration chamber using hydrostatic or air pressure. This is typically done by the manufacturer to examine the character of response to the applied pressure, sensitivity, etc. Users of pressure cells sometimes also conduct this type of calibration to verify the manufacturer's calibration.
2) The pressure cell is then loaded through a layer of field soil underlying a fluid or air pressure separated by membrane (to obtain a uniform stress distribution on soil). This is to account for the effects of pressure cell stiffness and dimensions on stress measurements.

In this study, however, the linearity of the pressure cell responses to known dead weights was investigated to ensure that the pressure cell was reading properly with the existing data acquisition hardware and software. Figure A.4 shows the calibration results of the four pressure cells. It should be noted that there was some discrepancy between the calibration using dead weights and the calibration provided by the manufacturer. The calibration factors are listed as: 7.252 psi/v (manufacturer), 5.629 psi/v (P1), 6.738 psi/v (P2), 7.228 psi/v (P3), and 6.984 psi/v (P4).

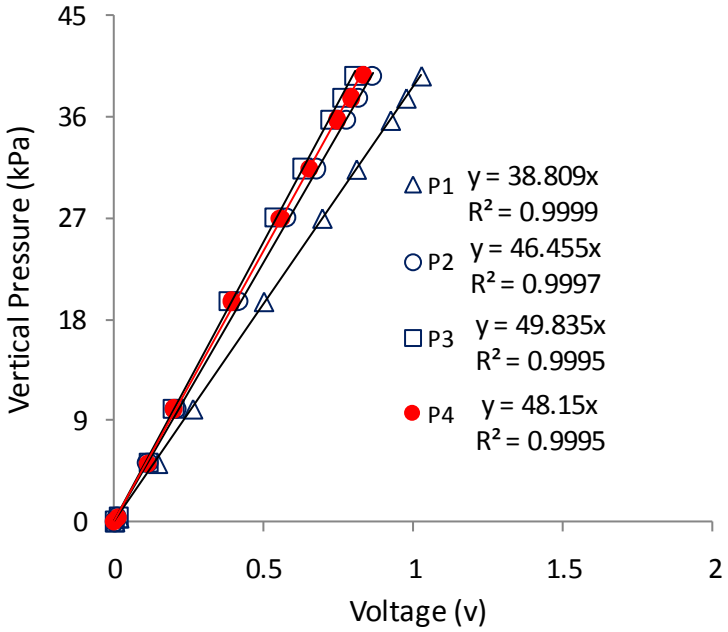

Figure A.4. Calibration of pressure cells

A.1.3 Geogrid Strain Gages

Due to the relatively lower modulus of geogrids, the external gage-adhesive-coat system could add reinforcements to the geogrid ribs on which the strain gages were attached. Using the in-air calibration of the local strain measurements from strain gages to the global measurements of strains in geogrids, it is possible to correlate the geogrid strain gage measurements to the strains developed in the geogrids when geogrids are placed in the pavement and subjected to the accelerated testing.

As Figure A.5 shows, a 20-cm × 30-cm geogrid specimen was tested on an Instron machine under static tensile loading. Two strain gages were installed onto the two opposite faces of a geogrid rib by following the same procedures that were adopted to attach the strain gages onto geogrids in the pavement. In addition to the strain measurements from the two strain gages, geogrid strains were measured in the geogrid ribs parallel with and next to the instrumented geogrid rib. For each of the three geogrids, the calibration was carried out for grid ribs in both machine-direction and cross-machine direction.

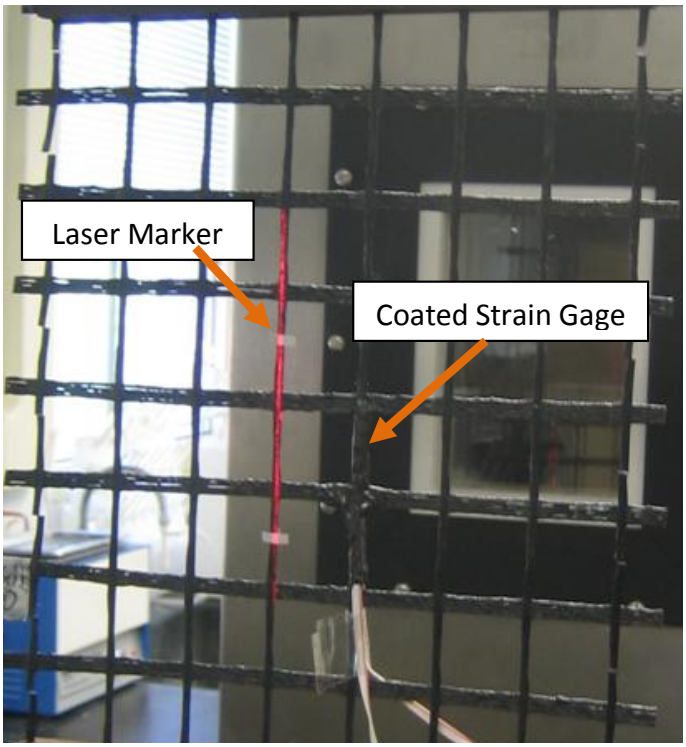

Figure A.5. Calibration of geogrid strain gages

The results of strain gages calibration for the three geogrids are presented in Figure A.6 through Figure A.8. The relationships between the strain gage measurements and global strain measurements were used to calibrate the strain gage measurements of geogrids in the accelerated testing.

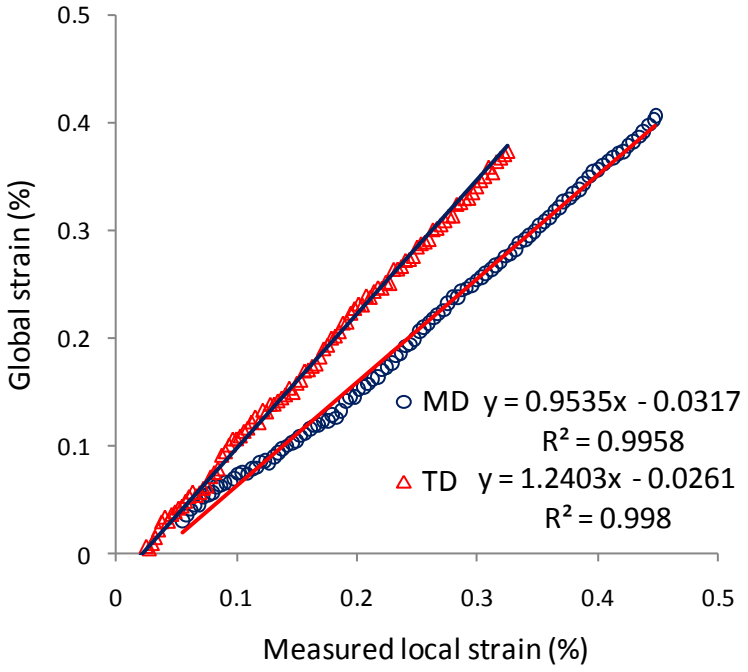

Figure A.6. Calibration results for Grid A in both machine-direction (MD) and cross machine direction (TD)

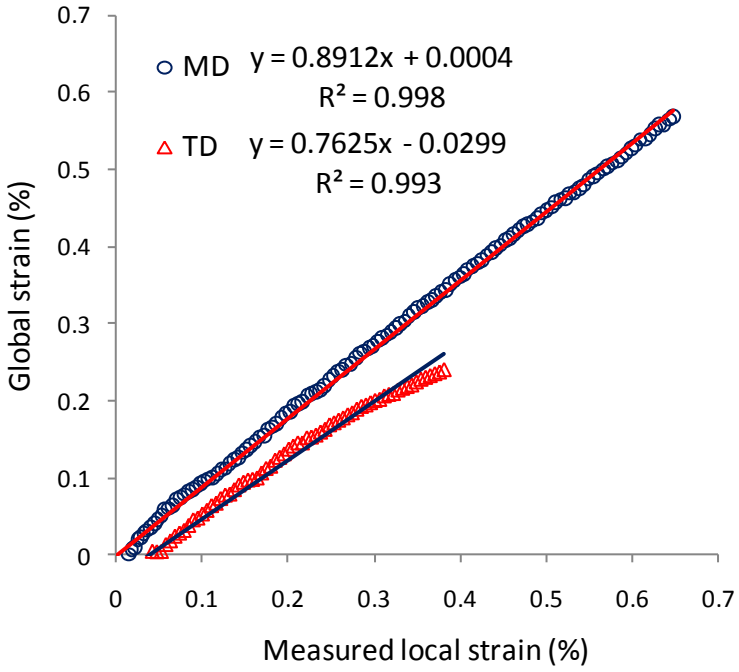

Figure A.7. Calibration results for Grid B in both machine-direction (MD) and cross machine direction (TD)

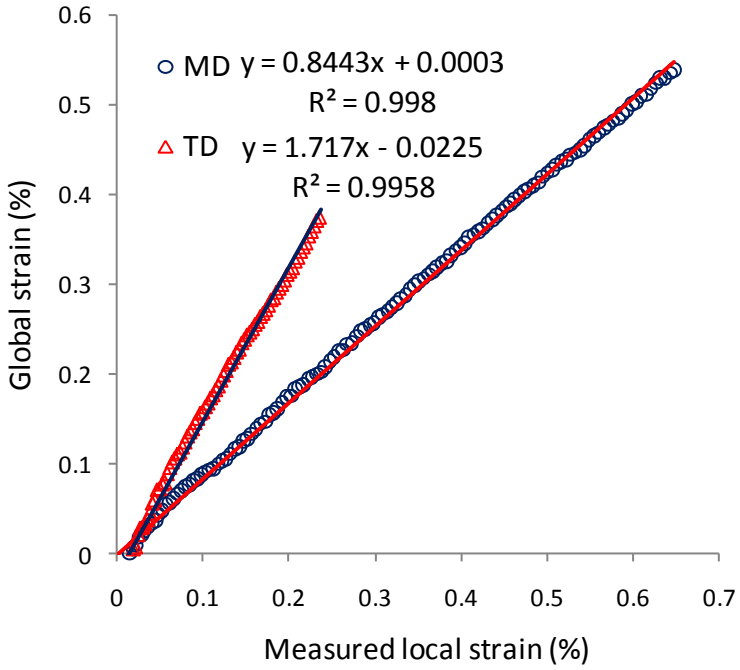

Figure A.8. Calibration results for Grid C in both machine-direction (MD) and cross machine direction (TD)

A.1.4 Data Acquisition

The data acquisition (DAQ) hardware was evaluated according to the cost, product quality, processing speed, and its variability in terms of a relatively wide range of input modules and sensors. A National Instruments® data acquisition hardware was selected, including a USB compacted chassis (NI cDAQ-9172) housing six different modules for analog and digital inputs. The system ensured enough channels corresponding to the specified sensors and strain gages. This pilot study involved using only two types of modules: NI 9237 and NI 9205 analog input module. The NI 9237 module for strain gages consists of four channels, and each channel has an independent 24-bit analog-digital converter (ADC) and input amplifier. The module has programmable excitation ranging from 2.5 V to 10 V, with the limitation of 150-mW excitation power. The NI 9205 module for the LVDT and pressure cell provides connections for the 32 single-ended or 16 differential analog input channels depending on the measurement configuration. In this study, a differential configuration was adopted to attain more accurate measurements and less noise.

A.2 Instrumentation Installation

Following the selection of appropriate instruments for measuring pavement responses, it is vital to properly install the instruments in the pavement system to obtain reliable and meaningful measurements. The following general rules were followed during the installation of instruments:

- Minimal disturbance to the pavement system
- Adequate protection of the instruments from mechanical damage and moisture damage

A.2.1 Installation of LVDTs and Potentiometers

The installation of LVDTs was accomplished in two steps. Prior to the construction of subgrade, a steel tube for housing the LVDT later on was mounted on a concrete slab and placed in the desirable position as Figure A.9-a displays. The concrete slab was leveled as much as possible to ensure the horizontal level of the subsequent LVDT installation. The cable for the LVDT was also protected from angular aggregates by using a PVC pipe. After the construction of the subgrade, the LVDT was connected to the cable and inserted into the steel tube by excavating the built subgrade to avoid possible damage to the LVDT during the subgrade construction. A thin yet rigid disk with diameter of 5 cm (2 in) was attached onto the contact tip of the spring-loaded LVDT to provide sufficient contact area with the soil-geogrid interface, as illustrated in Figure A.9-b. The contact tip was wrapped with thin and flexible membrane to avoid the intrusion of soil particles into the LVDT. The LVDT was totally immersed in the soil with its contact disk flush with the soil surface but underneath the geogrid.

(a)

(b)

Figure A.9. Installation of LVDT: (a) a housing steel tube was mounted on a concrete slab; (b) a circular plate was attached to the LVDT contact tip

A.2.2 Installation of Potentiometers

Potentiometers were first customized by attaching two circular disks onto both ends (Figure A.2). The potentiometer was sealed using thin membranes to prevent intrusion of soil particles and moisture (Figure A.10-a). The circular disk on the potentiometer contact tip first was not attached onto the potentiometer in order to accommodate the installation. A pattern of the potentiometer in the soil was prepared according to the diameter and length of the customized potentiometer as Figure A.10-a shows. The customized potentiometer was placed in the excavated pattern and kept as vertical as possible (Figure A.10-b). Soil was backfilled and compacted manually using small tools, as Figure A.10-c illustrates. The circular disk was attached back onto the potentiometer when the excavated pattern was filled by soil (Figure A.10-d).

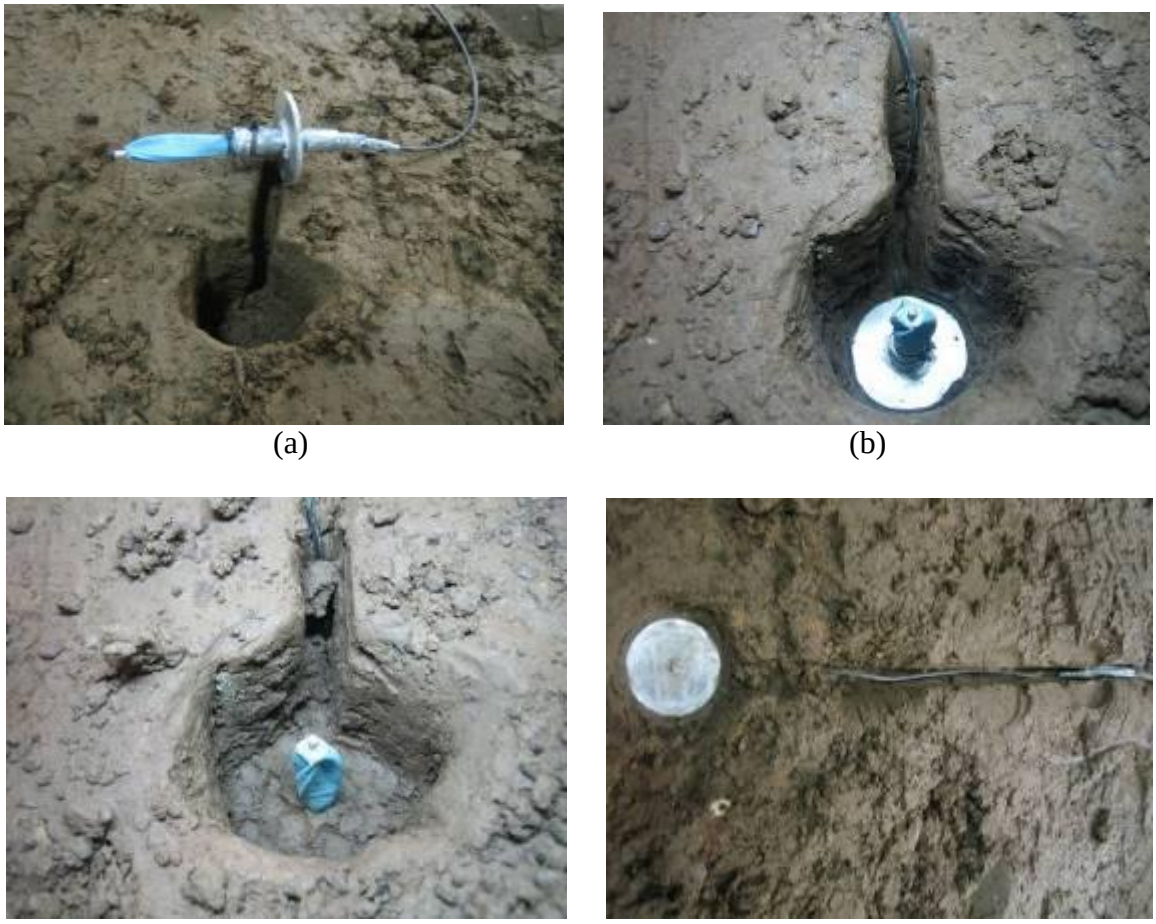

(a) (b)

(c) (d)

Figure A.10. Installation of a customized potentiometer in the subgrade soil: (a) a potentiometer pattern in the soil was excavated; (b) the customized potentiometer was placed in the pattern; (c) soil was filled and compacted in the pattern; (d) the circular disk was attached back

A.2.3 Installation of Earth Pressure Cells

The pressure cell was installed in place upon completion of the subgrade layer construction. The subgrade was excavated using small hand tools for placement of the pressure cell. The pressure cell was installed about 1.3 cm (0.5 in) below the subgrade surface. A small trench was excavated to accommodate the wire from the pressure cell to a PVC pipe. It is important to fully compact and level the base of the excavation before the placement of the pressure cell. The excavation was then backfilled with compacted stone-free soils. The pressure cell was positioned and leveled again before being covered by fine soils, as shown in Figure A.11-a. Figure A.11-b shows that the pressure cell was

surrounded by fine soil particles to avoid stress concentration caused by individual-aggregate contact, and the wires were housed in PVC pipes.

(a) (b)

Figure A.11. Installation of the pressure cell: (a) the pressure cell was leveled before being covered by soil; (b) excavation was backfilled by fine soils and wires from the pressure cell were housed in PVC pipes.

A.2.4 Installation of Strain Gages on Geogrids

The installation of strain gages onto geogrid ribs was challenging and cumbersome. One should be aware of the following factors contributing to the difficulties of strain gage installation on geogrids:

- The working space is narrow and constrained due to the small areas of grid ribs.
- The surface of the grid ribs is uneven and irregular, and needs careful preparation.
- The net-like geogrid does not provide a stable structure for attaching strain gages. Care needs to be exercised to keep the geogrids in position during the installation.
- The delicate gages need to be protected from mechanical and moisture damage.

Knowing the difficulties of installing strain gages onto geogrids as discussed above, a procedure was developed after an in-depth literature review and personal communication with experts. Three primary steps were involved in installing a strain gage onto geogrid:

surface preparation, gage attachment, and protective coating. Listed below are the materials and accessories that were used during the installation:

- Surface preparation: CMS-2 degreaser, MCA-2M-Prep conditioner A, MN5A-2M-Prep neutralizer, sandpaper, GSP-1 Gauze sponges, Q-tips
- Gage attachment: M-Bond AE-10 adhesive, PCT-2M tape
- Protective coating: M-Coat J-3, TFE-2 Teflon tape

The installation process needed to consider that strain gages were attached on both lower and upper faces of a singe rib. Furthermore, the working life of each unit of adhesive and coating materials was limited once the unit was opened. The following general steps were followed to optimize and accommodate the installation:

1) Clean and prepare all the working surfaces for the three geogrids on both sides. Keep the geogrids in a clean environment and away from dust.
2) Attach strain gages on one side of the geogrid ribs; wait for 24 hours for the adhesive to cure and attach strain gages onto the other side of the geogrid ribs.
3) Apply coating materials onto both sides of the geogrid ribs.

Following the procedures and operations in this specific study, it was found that one unit of the adhesive typically was able to serve 4 strain gages, and one unit of coating material served 12 strain gages during the time period from the opening of the unit to its cure. Details of the three steps are presented as follows.

Surface Preparation

The purpose of surface preparation was to provide a bondable base for the strain gage to be attached onto. The quality of bond relies on the surface cleanness and evenness. A good reference for preparing working surfaces in general for strain gages is the tech note from Vishay (2005-a).

The nature and textures of surfaces for the stiff geogrid (Grid B) and flexible geogrids (Grid A and Grid C) were quite different. The surface of the stiff geogrid was relatively smoother and suitable for bonding, while the surfaces of the flexible geogrids were irregular and porous. General surface preparation procedures were followed for treating the stiff geogrid surface, as described below:

- Stabilizing: steel rods were temporarily tied onto the geogrid ribs adjacent to the working surfaces to provide a stable structure and to avoid any bending.
- Degreasing: CMS-2 degreaser was applied to the target ribs and adjacent areas to remove any greases, contaminants, chemical residuals, etc.
- Abrading: the target surfaces were abraded using sandpaper to remove any loosely bonded adherents and create a rough surface texture for bonding.
- Positioning: central lines in the longitudinal and transverse directions were marked on the test surfaces.
- Conditioning and neutralizing: M-Prep conditioner A was applied to the abraded surfaces to clean any residuals followed by the application of MN5A-2M-Prep neutralizer to create an optimum alkalinity suitable for the adhesive.

The stiff geogrid surfaces were ready for strain gage attachment after following the steps listed above, while a workable surface for the flexible geogrids needed further steps to develop a bondable working area for strain gages. Figure A.12-a shows a flexible geogrid after the removal of the bituminous coat and cleaning of the ribs.

It was noticed that the surface was still not suitable for attaching strain gages because the multifilament yarns were exposed from the removal of the coat. It was decided to use the adhesive materials to create a base for the strain gage attachment after personal consulting (Bakis, 2009) and careful literature review. A generous amount of adhesive (M-Bond AE-10) was applied onto the geogrid ribs (Figure A.12-b). A grinder was used to carefully shape and polish the surfaces after the adhesive cured, as Figure A.12-c shows. The surfaces were then cleaned, conditioned, and neutralized following the procedures previously described. Figure A.12-d presents a close view of the prepared surfaces for flexible geogrids.

(a)

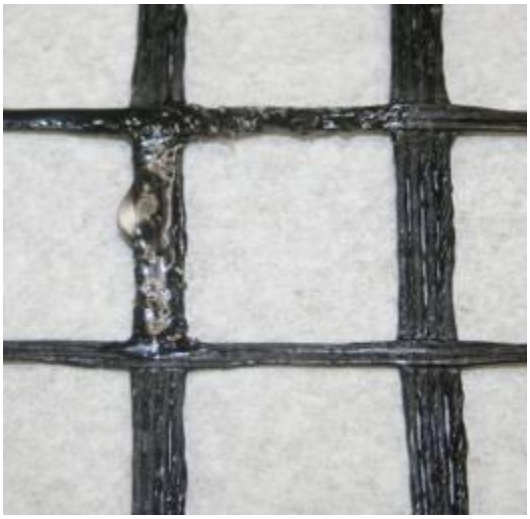

(b)

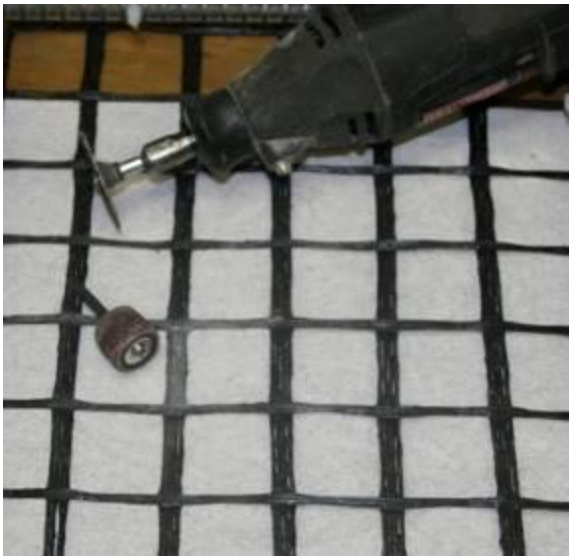

(c)

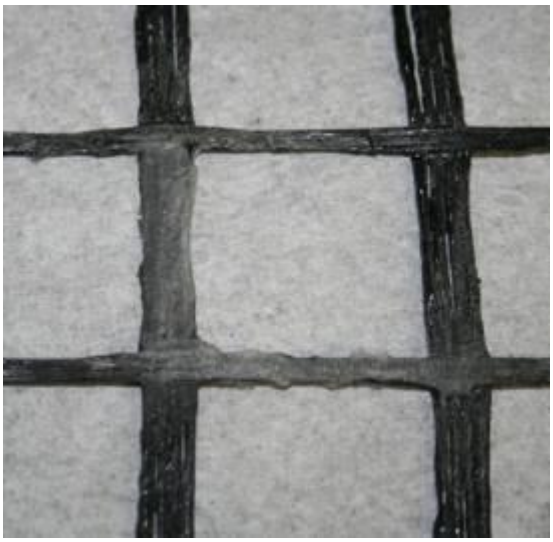

(d)

Figure A.12. Surface preparation for the strain gages installation onto a flexible geogrid: (a) initial cleaning and removal of coating; (b) application of adhesive onto the target geogrid ribs; (c) shaping and polishing the cured adhesive; (d) a close view of the prepared surfaces

Gage Attachment

The strain gage was positioned on the rib according to the previously marked central lines, by using PCT-2M gage installation tape as a carrier (Figure A.13-a). M-Bond AE-10 was used for gage adhesive. It has the characteristics of high elongation, high viscosity, and ability to fill irregular surfaces. It cures in 40 hours after application at room temperature (75 °F).

Dead weights were applied to the gages during the time period of curing. Silicone gum pads were used to help evenly distribute the applied force (Figure A.13-b). Detailed information on attaching strain gages onto a test specimen can be found from a technique note (Vishay, 2005-b).

Protective Coating

A two-component material (M-Coat J-3) was used as the protective coating in this study (Figure A.13-d). The coating became tough yet flexible after it cured. The exposed strain gage grids and wire leads were wrapped using TFE-2 Teflon tape before applying the protective coat (Figure A.13-c).

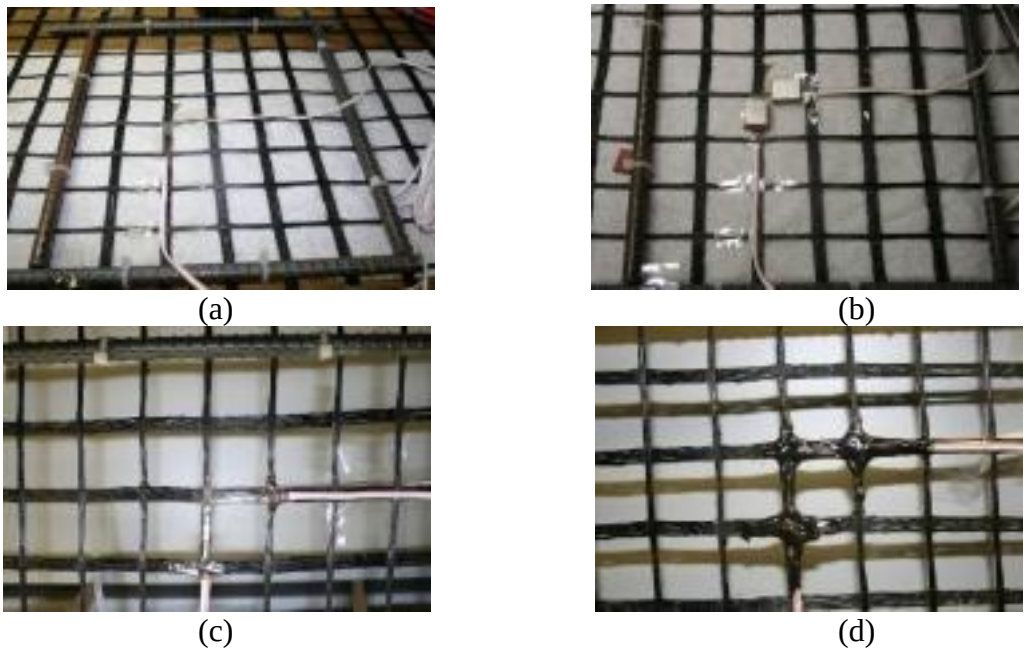

(a) (b) (c) (d)

Figure A.13. Installation of strain gages onto geogrid ribs: (a) strain gage attachment; (b) gage pressure application; (c) isolation tape; (d) protective coating

APPENDIX B: PORTABLE LIGHTWEIGHT DEFLECTOMETER

A portable lightweight deflectometer (Carl Bro^{TM} PRIMA 100) was used for in-situ assessment of pavement layer modulus. The LWD applies an impulse load to the pavement surface and the deflections are measured at various distances from the load. The moduli of pavement layers are computed based on the measured deflection using a backcalculation program. The backcalculation is an "inverse" procedure of determining material properties of pavement layers from its response to surface load. It involves using iteration or optimization to calculate theoretical deflections by varying the material properties until the calculated deflections are close to the measured defections. This makes it possible to characterize quantitatively the reinforcement transition zone in the vicinity of geogrids by measuring the modulus layer by layer during the construction.

Figure B.1-a shows a portable lightweight deflectometer with one deflection sensor measuring the deflection at only one location (underneath the drop weight). By dropping the drop weight, the modulus is calculated by the software package based on the following equation (Fleming et al., 2007):

$$E = \frac{A \cdot P \cdot r(1-\nu^2)}{d} \tag{38}$$

where

E = modulus;

A = plate rigidity factor, default value is 2 for a flexible plate, $\pi/2$ for a rigid plate;

P = maximum contact pressure;

r = plate radius;

v = Poisson's ratio (typically ranging from 0.3 to 0.45 depending on test materials);

d = peak deflection.

Figure B.1-b displays an example output from a laboratory test on aggregate layer surface. It is noted that the peak deflection did not occur at the same instant as the peak force, which is typical (Fleming et al., 2007).

With additional deflection sensors, multilayer moduli can be computed based on the deflections measured at a certain distance using a backcalculation technique. Backcalculation seeks to match the measured surface deflection with a calculated deflection based on assumed layer moduli. The assumed layer moduli in the computation model are adjusted until the calculated deflection is close to the measured one. The combination of the assumed layer moduli is then considered to be near the in-situ moduli of the pavement layers (Lytton, 1989).

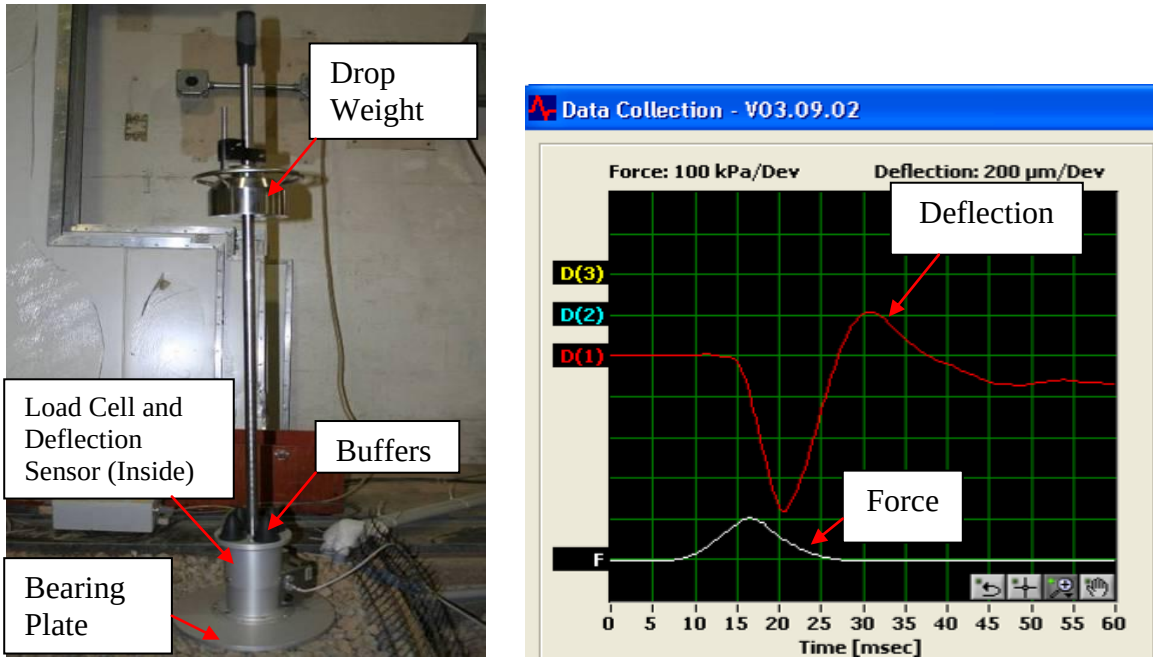

Figure B.1. Portable lightweight deflectometer: (a) Major components of LWD; (b) example output from a laboratory test